



universität  
wien

# DIPLOMARBEIT

Titel der Diplomarbeit

**First-principles study of the Fe-rich  
 $\text{Fe}_x\text{Ni}_y\text{Al}_{1-x-y}$  alloy system**

Verfasser

Georg Kastlunger

angestrebter akademischer Grad

Magister der Naturwissenschaften (Mag. rer. nat.)

Wien, Juli 2011

Studienkennzahl lt. Studienblatt: A419

Studienrichtung lt. Studienblatt: Chemie

Betreuer: Ao. Univ.-Prof. Dr. Raimund Podlucky



# Abstract

The present diploma thesis deals with the identification and description of stable ordered phases in the ternary iron-nickel-aluminium system (Fe-Ni-Al) based on a first principle concept. The aim of the work was to perform a concentration dependant search for ground state phases of a ternary system with the precision of density functional theory calculations. For this the Cluster expansion in combination with Monte Carlo simulations was applied.

As a basic quantity the enthalpy of formation was calculated, which is the responsible for the formation of stable phases in an alloy system. By including the enthalpies of formation of the calculated structures in a ground state diagram the stable phases could be identified.

The body centered cubic (bcc) parent lattice was chosen, since we were interested in the Fe-rich  $\text{Fe}_x\text{Ni}_y\text{Al}_{1-x-y}$  alloy system as an example for the application of a Cluster Expansion on a multicomponent system. The Fe-Ni-Al system is of high scientific and technological interest since the binary subsystems (Ni-Fe, Al-Fe, Ni-Al) are of different characteristics (i.e. lattice types, phase stability) while the ternary phase diagram shows a stable B2-phase regime in the pseudo binary  $\text{Fe}_x(\text{NiAl})_{1-x}$  part. On the basis of *ab initio* results for various configurations from DFT, calculated with the *Vienna Ab initio Simulation Package* (VASP) effective cluster interaction energies were calculated employing the *UNiversal CLuster Expansion* (UNCLE) code. After an extensive ground state search the stable phases in the bcc lattice were identified. By combining the results of the binary and ternary ground state searches to construct phase diagrams at finite temperatures the converged ECIs were used in both, canonical and grand-canonical Monte-Carlo simulations. The formation of ordered phases was simulated by starting from completely unordered systems –which represents an infinite high temperature– and cooling down to 100 Kelvin. By slowly heating up again the effect of the configurational entropy was studied.

The identification of the formed phases in the simulation boxes was done by a self elaborated method analyzing short range ordering with an extension of 3x3x3 atoms for binary and ternary phases and 10 atoms for elemental precipitations.

As expected the investigations done on the binary systems lead to somehow different results. The binary Ni-Al system has shown to form the most stable phases in the ternary system, with B2-NiAl showing the lowest enthalpy of formation. Other two stable ground states have been identified. In contrast to Ni-Al the Ni-Fe system did not tend to form ordered structures in the bcc lattice. The ground states of the Al-Fe system turned out to be less stable than in the Ni-Al system, but the ordering is still energetically favourable. From the found phases at T=0K three have shown to be stable also at finite temperatures.

B2-NiAl has shown to form deep into the ternary region, while Fe forms elemental precipitations. The ratio between nickel and aluminium concentration has a great influence in the extension of the B2 region. On the Al rich side of the investigated concentration range B2-NiAl is formed up to 80 % iron, while on the Ni-rich side the phase is destabilized already at 60 % Fe. As the reason for this behaviour a stabilization of the excessive aluminium in the iron matrix by  $\text{Fe}_3\text{Al}$  like ordering has been identified. Since nickel did not tend to form ordered structures with iron in a bcc lattice the excess of Ni destabilizes the B2-NiAl ordering by replacing Al in the B2 crystal.

In the region of nearly pure iron nickel and aluminium still have shown to cluster in a B2-like way.

# Zusammenfassung

Die eingereichte Diplomarbeit befasst sich mit der Identifikation und Beschreibung stabiler geordneter Phasen im ternären Eisen-Nickel-Aluminium System (Fe-Ni-Al). Die grundlegende Zielsetzung bestand darin eine konzentrationsabhängige Suche nach den Grundzustandsphasen eines ternären Systems mit der Präzision der Dichtefunktionaltheorie durchzuführen. Um dies zu erreichen wurde ein Cluster Expansion Ansatz in Kombination mit Monte Carlo Simulationen gewählt.

Als grundlegende Größe in der CE wird die Formationsenthalpie verwendet, welche Aussage über die Stabilität einer gebildeten Phase gibt. Durch Herausfiltern der Strukturen, welche die größte Formationenthalpie besitzen können durch ein Grundzustandsdiagramm die stabilen Phasen einer mehrkomponentigen Legierung identifiziert werden.

In der vorliegenden Arbeit wurde das kubisch innenzentrierte Gitter (bcc) basierend auf der Fe-reichen Seite des ternären Systems  $\text{Fe}_x\text{Ni}_y\text{Al}_{1-x-y}$  als Beispiel verwendet um die Anwendung der CE auf Systeme mit mehr Komponenten zu zeigen. Dieses Legierungssystem ist in wissenschaftlicher und technologischer Sicht wertvoll, da die binären Subsysteme (Ni-Al, Fe-Al, Fe-Ni) verschiedene Eigenschaften aufweisen, während das ternäre System eine stabile B2 Phase über einen grossen Bereich im pseudo-binären  $\text{Fe}_x(\text{NiAl})_{1-x}$  Bereich zeigt.

Auf der Basis von *ab initio* Ergebnissen, welche mittels des *Vienna Ab initio simulation packages* VASP für einige ausgewählte Strukturen berechnet wurden, wurden durch die Anwendung des *UNiversal CLuster Expansion* UNCLE codes effektive Cluster Wechselwirkungen bestimmt. Nach einer ausgiebigen Grundzustandssuche konnten die stabilen Phasen im System identifiziert werden. Durch Kombination der Ergebnisse, die von den binären und ternären CE erhalten wurden, wurden mittels Monte Carlo Simulationen in kanonischen und grosskanonischen Ensembles die Phasendiagramme bei ausgewählten Temperaturen gezeichnet.

Als Start fuer die Beschreibung der Formation von stabilen Phasen bei finiten Temperaturen wurde eine komplett ungeordnete Monte Carlo Box –entspricht unendlich hoher Temperatur– verwendet und im Laufe der Simulation auf 100 Kelvin abgekühlt. Durch langsames Aufheizen wurde der Effekt der Konfigurationsentropie studiert.

Zur Identifikation der gebildeten Phasen wurde eine selbstentwickelte Methode verwendet, welche die Analyse der kurzreichweitigen Ordnung in einer Ausdehnung von  $3 \times 3 \times 3$  Atomen für binäre und ternäre Phasen beinhaltet. Elementare Ausscheidungen wurden ab einer Clustergröße von 10 Atomen als solche gekennzeichnet.

Die Untersuchungen an den binären Systeme führten wie erwartet zu verschiedenen Ergebnissen. Die binären Phasen des Ni-Al Systems besitzen die höchste Stabilität im untersuchten ternären System. Als stabilste Struktur wurde B2-NiAl identifiziert. Zwei

weitere Phasen wurden gefunden. Im Gegensatz zu Ni-Al zeigt das Ni-Fe System keine Tendenz zur Bildung geordneter Strukturen im kubisch innenzentrierten Gitter. Die Phasenbildung im Al-Fe System ist energetisch sehr begünstigt. Drei Grundzustände wurden gefunden, welche auch bei höheren Temperaturen stabil sind.

Als stabilste Struktur im System bildet sich B2-NiAl weit in das ternäre System hinein, wobei Eisen in diesem Fall als elementare Ausscheidungen formt. Diese Ausdehnung wird stark durch das Verhältnis der Konzentration von Nickel und Aluminium beeinflusst. Während auf der aluminiumreichen Seite des untersuchten Konzentrationsbereichs B2-NiAl bis zu einer Konzentration von 80 % Eisen gebildet wurde, wird die binäre Phase auf der nickelreichen Seite bereits bei 60 % Eisen destabilisiert. Als Grund für dieses Verhalten wurde eine Stabilisierung des überschüssigen Aluminiums in der Eisenmatrix durch die Bildung von  $\text{Fe}_3\text{Al}$  gefunden. Da Nickel und Eisen keine geordneten Phasen im bcc Gitter bilden, wird die B2-Phase auf der nickelreichen Seite durch die Bildung von Ni-Antisites auf den Aluminiumplätzen des Kristalls destabilisiert.

Im Bereich des ternären Systems, welcher aus nahezu reinem Eisen besteht wurde bereits ein Clustern von Nickel und Aluminium in einer B2-artigen Struktur identifiziert.

# Contents

<b>1</b>	<b>Introduction</b>	<b>1</b>
<b>2</b>	<b>Theoretical background</b>	<b>3</b>
2.1	Density Functional Theory . . . . .	3
2.1.1	History . . . . .	3
2.1.2	Schrödinger's equation . . . . .	4
2.1.3	Hohenberg-Kohn theorems . . . . .	5
2.2	Kohn-Sham equations . . . . .	6
2.3	Calculating the exchange-correlation energy . . . . .	7
2.3.1	Exchange and correlation functionals . . . . .	8
2.3.2	Local spin density approximation . . . . .	8
2.3.3	Generalized gradient approximation . . . . .	9
2.4	Computational implementation of DFT . . . . .	10
2.5	Determination of ground state properties . . . . .	10
2.5.1	Ground state phase diagrams . . . . .	11
2.6	The Cluster Expansion . . . . .	12
2.6.1	Basic principles of the Cluster Expansion . . . . .	13
2.7	The UNCLE-code . . . . .	16
2.7.1	Selecting the input structures . . . . .	17
2.7.2	Determination of the ECIs . . . . .	17
2.7.3	The genetic algorithm . . . . .	18
2.7.4	Running the Cluster Expansion . . . . .	20
2.8	Monte Carlo simulations . . . . .	21
2.8.1	Random walks and Markov-chains . . . . .	22
2.8.2	The Metropolis Rosenbluth algorithm . . . . .	23
2.8.3	Implementation of the MC simulation in the UNCLE code . . . . .	24
<b>3</b>	<b>Elemental metals</b>	<b>27</b>
3.1	Nickel (Ni) . . . . .	27
3.1.1	DFT results . . . . .	27

3.2	Aluminium (Al) . . . . .	29
3.2.1	DFT results . . . . .	29
3.3	Iron (Fe) . . . . .	31
3.3.1	DFT results . . . . .	31
<b>4</b>	<b>Binary alloys and compounds</b>	<b>35</b>
4.1	Nickel-Aluminum . . . . .	38
4.1.1	Experimental findings . . . . .	38
4.1.2	Search for the ground states . . . . .	40
4.1.3	Monte Carlo simulations . . . . .	44
4.1.4	Summary . . . . .	47
4.2	Iron-Aluminum . . . . .	48
4.2.1	Experimental findings . . . . .	48
4.2.2	Search for the ground states . . . . .	49
4.2.3	Monte Carlo simulations . . . . .	50
4.2.4	Summary . . . . .	54
4.3	Nickel-Iron . . . . .	56
4.3.1	Experimental findings . . . . .	56
4.3.2	Search for the ground states . . . . .	57
4.3.3	Monte Carlo simulation . . . . .	58
4.3.4	Summary . . . . .	61
<b>5</b>	<b>The ternary system (Fe-Ni-Al)</b>	<b>63</b>
5.1	Introduction . . . . .	63
5.2	Fe-Ni-Al phase diagram . . . . .	64
5.3	Ground state search . . . . .	68
5.3.1	Technical details . . . . .	68
5.3.2	CE calculations and results . . . . .	71
5.4	Monte Carlo simulations . . . . .	73
5.4.1	Technical details . . . . .	73
5.4.2	Results and Discussion . . . . .	77
5.4.3	Pseudo binary $\text{Fe}_x(\text{NiAl})_{1-x}$ system . . . . .	83
5.4.4	Fe-rich side of the phase diagram . . . . .	86
<b>6</b>	<b>Conclusion</b>	<b>91</b>
	<b>Bibliography</b>	<b>93</b>
	<b>Danksagung</b>	<b>98</b>



In the last decade, application of density functional theory (DFT) to materials properties became very successful and in quite a few cases it works on the same level of accuracy as experiments. Most of the standard DFT work consists in working with systems of rather small unit cells of a few hundreds of atoms at most describing ordered structures, even when alloy properties and configurational averages are described. If, however, one wants to go far beyond such a size limitation and wants to bridge the length scale one has to think about other extended concepts.

Another problem consists in finding the actual ground state, i.e. the equilibrium structure of a compound at low temperatures. Experimentally, this is also a problem because e.g. synthesizing an alloy by melting the constituent metals and measuring its properties at lower temperatures means to cool down; then atomic motion is frozen in and metastable states can survive for a considerable time. Finally reaching the thermodynamic ground states could mean that after some years cracks and materials failures form. This happened e.g. to air plane wings made of Al-rich Al-Li alloys. The theoretical way out is to make an extensive and exhaustive search for all possible structures, requiring the calculation of  $10^4$  to  $10^6$  different structures. Such a task is clearly impossible if its done brute force.

For both problems the method of choice is the Cluster Expansion (CE), which - if done properly- maintains DFT accuracy for systems with many atom types and for concentration dependent configurational averages.

One of the most basic problems in material sciences is the determination of phase stabilities of alloy systems with two or more atoms.

The determination of a phase diagram by theoretical calculations with useful accuracy needs basically two major requirements, namely many atomic configurations have to be searched through and temperature must be taken into account. Theoretically, on a DFT level this can be achieved by combining the CE with Monte Carlo simulations, which includes the configurational entropy. The temperature dependency can be taken even further and be made more realistic by including vibrational free energies, again derived from DFT calculations with their inherent accuracy. This is, however, a very demanding task but nevertheless it was done by D. Reith (also in the working group of R. Podlucky)

for Fe-Cu binary alloys.

The CE is a concept to model configuration dependent properties of a system by taking a set of DFT calculations and deriving the unknown effective cluster interactions (ECIs) from fitting the CE ansatz to the DFT input. If the system is friendly, by using a rather small number of DFT treated input structures properties like the free energy, the formation energy, volume and magnetic behaviour can be determined. The basic principle of the CE is that physical observables such as the enthalpy of formation, which is defined for periodically repeated structures, can be reformulated in terms of interacting building blocks (i.e. clusters). The building blocks are known because of the underlying crystal lattice. (At present, this is a basic requirement for CE, that one common lattice is used for all configurations). The unknown glue between the blocks is derived from fitting the CE derived enthalpies of formations of selected structures to the hard numbers of DFT calculations. By that no empirical values are needed and the configuration dependent properties at every composition can be determined truly from first principles. After a convergent CE is obtained, the many body cluster interactions can be used for Monte Carlo simulation in order to derive temperature dependent configurational averages.

In the present work the phase stabilities of the ternary Fe-Ni-Al alloy system is described using CE in combination with Monte Carlo simulations. Dealing with ternary systems using CE is a very demanding task, in particular concerning computer resources, accuracy of DFT calculations, the evaluation of a large set of data and the design of a suitable Monte Carlo strategy. Even though the Universal CLuster Expansion (UNCLE) code [1] could be used, quite some effort went into designing a proper expansion (apart from partially debugging and extending the code). Thanks to close collaboration with the group of G. Kresse, the VASP code was used, which is a very powerful working horse for DFT calculations. The focus was put on the Fe-rich part of the phase diagram in order to model NiAl precipitations in Fe. By that, the basic lattice for the CE is bcc, and the concentration range of Ni and Al can also be narrowed down. The three binary systems, Al-Fe, Ni-Al, and Fe-Ni, were however studied over the whole concentration range.

The thesis consists of two main parts. In the first part the theoretical backgrounds will be shown introducing the mathematical framework and algorithms used in the work. In the second part the work done on the Fe-Ni-Al system is presented. Starting with an analysis of the elements contained in the ternary alloys, the derived parameters like e.g. cutoff energies and  $k$ -point sets will be mentioned. In the next section the three binary systems populating the sides of the Gibbs triangle will be described through binary CE+MC approaches. As a result of these the ground state lines and derived binary phase diagrams will be shown. Finally the ground state structures gotten from the binary alloys will be used as a starting point for the description of the ternary Gibbs triangle by ternary CE+MC.

## 2.1 Density Functional Theory

### 2.1.1 History

The fundamental concepts of density functional theory (DFT) were proposed by Hohenberg and Kohn (HK) in their famous paper in the year 1964 [2]. The basic proposition of their work was, that all ground state properties of a quantum system - in particular the ground state total energy - are unique functionals of the ground state density. If this would work then all the ground state properties can be expressed by a function of 4 variables (space and spin), the density namely, rather than by the manybody wavefunction which is a function of  $4 \times N$  variables,  $N$  being the number of particles. This way of thinking in terms of the density rather than the wavefunction was not new: Thomas [3] and Fermi [4] (TF) published a somewhat similar -but much less rigorous- concept already in 1927, but in their work the crucial manybody electronic interactions were left out. The idea of TF was, that the kinetic energy can be described as a functional of the electron density of non-interacting electrons representing a homogeneous electron gas. The manybody exchange and correlation terms of the electrons were added by Dirac [5] in 1930, who formulated the local density approximation, which is still used today. It turned out, however, that the Thomas-Fermi-Dirac theory based on the homogeneous electron gas is not accurate enough for a predictive precision, in contrast to the modern applications of DFT.

A problem of the original HK theory is the uniqueness of the dependency of the energy functionals on the ground state density. It could be proven that this problem can be lifted for reasonable physical densities, but nevertheless the HK formulation is not useful for actual calculations of ground state properties with sufficient accuracy. A major progress was achieved one year after HK, when Kohn and Sham [6] presented a formulation by partially going back to a wavefunction description in terms of orbitals of independent quasi particles. The basic -and crucial- idea is that the manybody problem can be mapped onto a system of non-interacting quasiparticles. Since then up to now the Kohn-Sham equation (as derived later on) are used in practically all calculations based on DFT.

## 2.1.2 Schrödinger's equation

The basis of every *ab initio* approaches is the Schrödinger equation, which in its stationary (non-relativistic) form is an eigenvalue equation of the form

$$\hat{H}\Psi(\{\mathbf{r}_i\}, \{\mathbf{R}_\alpha\}) = E\Psi(\{\mathbf{r}_i\}, \{\mathbf{R}_\alpha\}) \quad (2.1)$$

with  $\Psi(\{\mathbf{r}_i\}, \{\mathbf{R}_\alpha\})$  as the wave function of the system, depending on the electron coordinates  $\mathbf{r}_i, i = 1, N$  (including the spin) and the coordinates of all nuclei in the system  $\mathbf{R}_\alpha, \alpha = 1, N_\alpha$ . Making use of the Born-Oppenheimer approximation and separating electronic and nuclear motion the electronic Schrödinger equation is then defined as

$$\hat{H}_{el}(\{\mathbf{r}_i\}, \{\mathbf{R}_\alpha\})\Psi_{el}(\{\mathbf{r}_i\}) = E_{el}\Psi_{el}(\{\mathbf{r}_i\}, \{\mathbf{R}_\alpha\}) \quad (2.2)$$

with the Hamilton operator,

$$\hat{H}_{el} = -\frac{\hbar}{2m_e} \sum_i \nabla_i^2 + \sum_i V_{ext}(\mathbf{r}) + \frac{1}{2} \sum_{i \neq j} \frac{e^2}{|r_i - r_j|} \quad (2.3)$$

which consists of the kinetic energy, the electron-nuclei Coulomb energy (the so-called external potential in the language of DFT),

$$V_{ext}(\mathbf{r}) = - \sum_\alpha \frac{Z_\alpha}{r_{i\alpha}} \quad (2.4)$$

and the electron-electron interaction. This definitions lead to an implicit dependency of  $E_{el}$  on the spatial distribution of the nuclei in the system. The ground state energy  $E_{el,0}$  is the lowest energy eigenvalue for a given distribution of nuclei. To calculate the total energy of the system the Coulomb energy between the nuclei has to be added,

$$E_0(\{\mathbf{R}_\alpha\}) = E_{el,0}(\{\mathbf{R}_\alpha\}) + \sum_{\alpha < \beta} \frac{Z_\alpha Z_\beta}{R_{\alpha\beta}} \quad (2.5)$$

which then results in a potential energy  $E_0(\{\mathbf{R}_\alpha\})$  in terms of the position of the nuclei.

The wave function in equation (2.2) depends on the electron positions and spins and has to be antisymmetric regarding the exchange of electrons.

### 2.1.3 Hohenberg-Kohn theorems

The HK approach consists in formulating an exact theory for manybody systems in terms of the electron density  $n(\mathbf{r})$ , which is defined as

$$n(\mathbf{r}) = \int \dots \int d^3r_2 \dots d^3r_N |\Psi_{el}(\mathbf{r}_1, \dots, \mathbf{r}_N)|^2 \quad (2.6)$$

and has to obey the relation

$$\int n(\mathbf{r}) d^3r = N_{el} \quad (2.7)$$

when  $N_{el}$  is the number of electrons in the system. This can be achieved by proper normalization of the manybody wavefunction.

There are two HK theorems:

- **Theorem I:** The external potential  $V_{ext}(\mathbf{r})$  of a system is determined uniquely - except for a constant- by the ground state density  $n_0(\mathbf{r})$ . As a consequence, the Hamiltonian is fully defined -except for a constant energy shift- and with the Hamiltonian also the wavefunction for the ground state is known.
- **Theorem II:** The ground state total energy  $E[n]$  of a system with a particular  $V_{ext}(\mathbf{r})$  is the global minimum of this functional when  $n = n_0$ .

Based on these two theorems the electronic energy-functional can be written as a sum of the kinetic energy operator, the external potential (equation (2.4)) and the so called exchange correlation functional  $E_{xc}$ . This leads to the form

$$\begin{aligned} E[n] &= T[n] + E_{xc} + \int d^3r n(\mathbf{r}) V_{ext}(\mathbf{r}) \\ &\equiv F_{HK}[n] + \int d^3r n(\mathbf{r}) V_{ext}(\mathbf{r}) \end{aligned} \quad (2.8)$$

with

$$F_{HK}[n] = T[n] + E_{xc} \quad (2.9)$$

The universal functional  $F_{HK}[n]$  includes the kinetic energy and the exchange-correlation potential (described in section 2.3) and is universal for the electronic system, because it only depends on the electronic density  $n$ . The minimization of the energy functional is now done requiring conservation of charge by integrating the density according to relation (2.7). Making use of the chemical potential  $\mu$  as a Lagrange parameter one derives

$$\mu = \frac{\delta E[n]}{\delta n(\mathbf{r})} = V_{ext}(\mathbf{r}) + \frac{\delta F_{HK}[n]}{\delta n(\mathbf{r})}. \quad (2.10)$$

This very elegant equation is, however, of no use in practical calculations. The crucial step towards practical applications of DFT is elaborated in the following section dealing with the Kohn-Sham equations.

## 2.2 Kohn-Sham equations

In the year 1965 Kohn and Sham (KS) reformulated DFT by introducing orbitals, i.e. mapping the fully interacting manybody system onto a fictitious independent-particle system with the requirement, that these KS orbitals build up the true ground state density. The derived KS equations are the ones which are solved when DFT is applied in all modern DFT calculations (as also used in the Vienna *Ab initio* Simulation Package, VASP). For deriving the KS equations it is required, that the ground state density is built up by the KS orbitals, i.e. the solutions of the KS equations:

$$\hat{H}_{KS}\phi_i = \varepsilon_i\phi_i \quad (2.11)$$

The Hamiltonian  $H_{KS}$  is built by the single particle kinetic energy term  $T_S$  and the effective potential  $V_{eff}(\mathbf{r})$  which are acting on one electron at the point  $\mathbf{r}$ .

$$\hat{H}_{KS} = -\frac{1}{2}\nabla_i^2 + V_{eff}(\mathbf{r}) \quad (2.12)$$

Since the Kohn Sham Hamiltonian is a functional of just one electron at the point  $\mathbf{r}$  the kinetic energy term and the classical Coulomb interaction energy of the electrons are defined analogous to the Hartree-Fock theory:

$$T_s = -\frac{1}{2}\sum_{i=1}^N \langle \phi_i | \nabla^2 | \phi_i \rangle = -\frac{1}{2}\sum_{i=1}^N \int d^3r |\nabla \phi_i(\mathbf{r})|^2 \quad (2.13)$$

$$E_{Hartree}[n] = \frac{1}{2}\int d^3r d^3r' \frac{n(\mathbf{r})n(\mathbf{r}')}{|\mathbf{r} - \mathbf{r}'|} \quad (2.14)$$

with the electron density defined according to the HK theories:

$$n(\mathbf{r}) = \sum_i |\phi_i(\mathbf{r}, \sigma)|^2 \quad (2.15)$$

The Hohenberg-Kohn ground state energy can now be rewritten according to the Kohn-Sham approach:

$$E_{KS} = \sum_i^N \varepsilon_i - E_{Hartree}[n] + E_{xc}[n] - \int \frac{\delta E_{xc}}{\delta n(\mathbf{r})} \quad (2.16)$$

The one electron energies  $\epsilon_i$  in equation (2.16) are results of the single particle Kohn Sham equations and generally have low physical meaning. By the addition of the many particle terms the ground state energy of the investigated system can be determined. The most sophisticated term in equation (2.16) is the exchange correlation energy, which contains all the many-body interactions of exchange and interaction of the electrons. It can be interpreted as the universal Hohenberg-Kohn functional -shown in equation (2.9)- with the one particle kinetic energy  $T_s[n]$  and the classical Coulomb term  $E_{Hartree}[n]$  taken out.

$$E_{xc}[n] = F_{HK}[n] - (T_s[n] + E_{Hartree}[n]) \quad (2.17)$$

or

$$E_{xc}[n] = \langle \widehat{T} \rangle - T_s[n] + \langle \widehat{V}_{ee} \rangle - E_{Hartree}[n] \quad (2.18)$$

Since  $E_{KS}$  contains only the electronic energy the total ground state energy of the system is calculated by adding the nuclei-nuclei repulsion term.

$$E_0 = E_{0,KS} + E_{NN} \quad (2.19)$$

The total energy is dependent of the ion positions  $\mathbf{R}_\alpha$  and -as a consequence- of the volume and the cell shape, so by minimizing the total energy term the ground state structure of the system can be computed.

The crucial point in the solvation of the single particle Kohn Sham equations is the approximation of the exchange correlation functional  $E_{xc}[n]$ . If it was known then the ground state energy of a many-body system could be computed by solving the independent Kohn-Sham equations and extend them with the  $E_{xc}[n]$  energy. That's why a few approximation techniques have been developed.

## 2.3 Calculating the exchange-correlation energy

By extracting the one particle kinetic energy and the long range Hartree energy from the exchange-correlation functional, the remaining term is now local. This means local or nearly local approximations can be used for the exchange and correlation energy calculation and the functional can be written as

$$E_{xc}[n] = \int d\mathbf{r} n(\mathbf{r}) \epsilon_{xc}([n], \mathbf{r}) \quad (2.20)$$

where  $\epsilon_{xc}([n], \mathbf{r})$  is a one electron energy term at the point  $\mathbf{r}$ , which is only dependent of the density  $n(\mathbf{r})$  in the neighborhood of the point  $\mathbf{r}$ . The spin densities are integrated in the  $\epsilon_{xc}([n], \mathbf{r})$ , that's why only the total densities appear in (2.20).

### 2.3.1 Exchange and correlation functionals

The derivation of the KS equations in section 2.2 is exact. As mentioned all complications of the electronic manybody problem, i.e. exchange and correlation, are packed into the energy functional  $E_{xc}[n^\uparrow, n^\downarrow]$  and its functional derivative  $V_{xc}[n^\uparrow, n^\downarrow]$ , using the spin-polarized notation. In general, these functionals are unknown for realistic systems and, therefore, approximations have to be made. The usefulness of an DFT application depends now on the quality of such approximations. As the success story of DFT proves such useful approximations could be made, and improving the quality of the approximation is one of the forefront field in modern DFT developments. Two of the most commonly used parametrizations of the exchange-correlation functionals are briefly introduced.

### 2.3.2 Local spin density approximation

In the local spin density approximation (LSDA) the exchange-correlation functionals of the general system are replaced by the corresponding expressions for a homogeneous electron gas. Locally, for each point in space and spin the value of the densities  $n, n^\uparrow, n^\downarrow$  are determined and for these values the corresponding results for the homogeneous electron gas are inserted according to,

$$E_{xc}^{LSDA}[n^\uparrow, n^\downarrow] = \int d^3r n(\mathbf{r}) \epsilon_{xc}^{hom}(n^\uparrow(\mathbf{r}), n^\downarrow(\mathbf{r})) \quad (2.21)$$

in which  $\epsilon_{xc}^{hom}$  is the exchange-correlation energy per electron of the homogeneous electron gas. Now,  $\epsilon_{xc}^{hom} = \epsilon_x^{hom} + \epsilon_c^{hom}$  and numerical parametrizations have to be made for the correlation functional  $\epsilon_c^{hom}$ , whereas  $\epsilon_x^{hom}$  is known for any value of the density. Including LSDA in any DFT computer code is easy and very fast. Although the approximation seems to be very crude it, nevertheless, works astonishingly well for many realistic systems. LSDA however gets inaccurate when the true density is strongly deviating from the constant density of an homogeneous electron gas, which occurs for localized states, such as e.g. 3d-states of transition metals or surface states. Then, LSDA leads to overbinding effects, i.e. bonding is too strong.

The spin can be taken into account either by the spin densities  $n^\uparrow(\mathbf{r})$  and  $n^\downarrow(\mathbf{r})$  or by a fractional spin polarization  $\zeta(\mathbf{r})$

$$\zeta(\mathbf{r}) = \frac{n^\uparrow(\mathbf{r}) - n^\downarrow(\mathbf{r})}{n(\mathbf{r})} \quad (2.22)$$



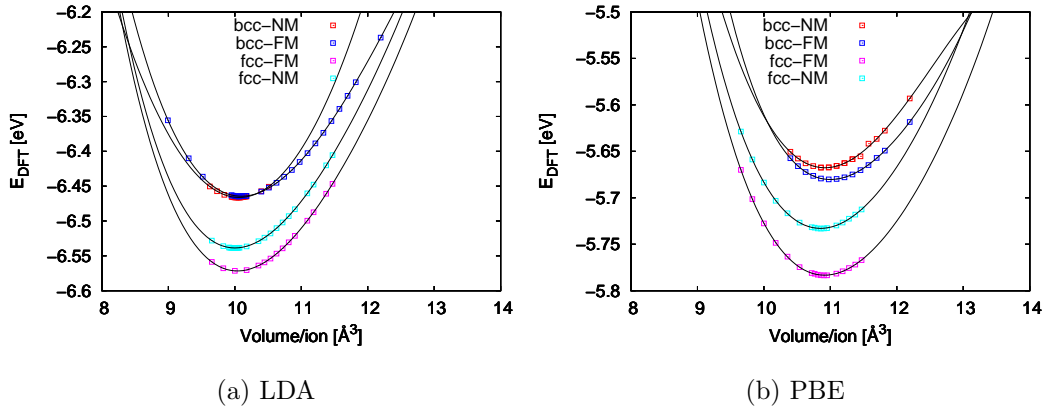


Figure 2.1: DFT total energy  $E(V)$  for Ni the fcc and bcc structure, both spin polarized (FM) and nonpolarized (NM) using the LSDA of Ceperley and Alder [8] and using the GGA of Perdew, Burke and Ernzerhof [9]. LSDA, overestimates the binding, because the equilibrium volume (i.e. energy minimum) is  $10.00 \text{ rÅ}^3$ . GGA yields a ground state minimum of  $10.90 \text{ rÅ}^3$ , which is very good when compared to the experimental value of  $10.94 \text{ rÅ}^3$  [10]

To improve the failure of LSDA it was suggested to include also the gradient of the density in the Taylor expansion of  $E_{xc}^{LSDA}[n^\uparrow, n^\downarrow]$ , as briefly discussed in the next section.

### 2.3.3 Generalized gradient approximation

The idea of the generalized gradient approximation (GGA) by taking into account also the gradient of the density was already proposed by Kohn and Sham in their original paper [6] and advanced by Herman et al [7]. Doing so the functional is now reformulated as

$$E_{xc}^{GGA}[n^\uparrow, n^\downarrow] = \int d^3r n(\mathbf{r}) \epsilon_{xc}(n^\uparrow, n^\downarrow, |\nabla n^\uparrow|, |\nabla n^\downarrow|) \quad (2.23)$$

Including the density gradient is by far not straightforward and therefore a variety of parametrizations exist. Throughout this work the functional of Perdew, Burke and Ernzerhof (PBE) was applied. Applying GGA cures most of the overbinding problems of LSDA. The most famous example is the ground state of Fe. LSDA predicts the ground state, namely the nonmagnetic fcc-structure. Making use of GGA correctly predicts the ferromagnetic ground state with bcc structure. On the other hand, for heavier atoms such as the 5d-transition metals, GGA leads to too large lattice spacings of about the same error which occurs for LSDA but in the other direction for too small volumes.

The accuracy of the two discussed (semi)local exchange correlation approximations is tested for Ni in figure 2.1, for which GGA is the better choice.

## 2.4 Computational implementation of DFT

All calculations of this diploma thesis are done by the Vienna ab Initio Simulation Package (VASP) from Kresse et al. [11, 12], which is a pseudopotential method. Pseudopotential approaches have big advantages concerning computational speed, because the KS basis functions are plane waves. Building the Hamiltonian matrix and solving the eigenvalue problem is very fast and the power of parallel architectures can be exploited in a powerful way. The disadvantage of a pseudopotential code is the need of pseudopotentials, i.e. of potentials which describe the Coulomb interaction of atomic nuclei screened by the innermost electronic states, which do not participate in the bonding. There is a very long history of pseudopotential construction and the most flexible and powerful is based on the projected augmented wave (PAW) construction of P. Blöchl [13]. The potentials have to be provided before any pseudopotential calculations start, i.e. they are input files. Often several choices of such pseudopotentials for the same atom are available, depending on the accuracy needed. Given all these ingredients total energies are derived. (Actually, due to the usage of pseudopotentials the so-called total energies are rather cohesive energies, because the references are atomic ions.) Finding (hopefully) the true ground state energy  $E_0$  as a function of lattice parameters, volume and atomic positions needs also forces, which can be derived within the Hellman-Feynman theorem. [14, 15] The minimization procedure is the following: for a given structure (lattice vectors and volume fixed) the forces acting on each atom are derived by the negative gradient of the DFT energy due to the atomic positions. The structure is relaxed until the forces are numerically zero. Then, volume and –if necessary– cell shape are changed and again the forces are relaxed until the minimum total energy  $E_0$  is reached. Thanks to the features of VASP, all these minimization steps can be done separately or in a combined way. The parameters needed for convergency in the present work are shown in chapter 3.

## 2.5 Determination of ground state properties

Before the theoretical and practical aspects of the Cluster Expansion (CE) will be elaborated the ground state properties of a system will be introduced and the definition of a ground state phase diagram will be explained. Results of DFT calculations provide a basis for the CE (see following section), but they are –strictly speaking– only valid at zero temperature. To overcome this limitation due to temperature Monte Carlo simulations based on the CE/DFT data are made which then deliver the ground state phase diagram

for a given temperature. The key quantity for the definition of the ground state is the enthalpy of formation as discussed in this section.

### 2.5.1 Ground state phase diagrams

A useful concept for describing a stable ground state of a thermodynamical system is the (internal) energy of formation  $\Delta U_f$  (constant volume) or the enthalpy of formation  $\Delta H_f$  (constant pressure). It is defined as the difference between the ground state energy  $E_0(\sigma)$  of the system with a given atomic configuration  $\sigma$  of atoms  $A, B, \dots$  and composition  $A_{x_A}B_{x_B}\dots$ , and the sum of reference energies of the pure elemental ground state energies  $E_{0,i}$  weighted by the mole fraction  $x_i$  of the components,

$$\Delta H_f = E_0(\sigma) - (x_A \cdot E_{0,A} + x_B \cdot E_{0,B} + \dots) \quad (2.24)$$

From the differences  $\Delta H_f$  or  $\Delta U_f$  the stability of investigated structures can be extracted. By combining the formation data in a so-called ground state diagram the compositions with highest stability (i.e. lowest formation energy or enthalpy) can be identified. Figure 2.2 shows an example of such a ground state diagram for the binary system  $A_{x_A}B_{x_B}$ . It is constructed by plotting the calculated formation enthalpy  $\Delta H_f$  of different phases (i.e. compounds) versus the mole fraction  $x$  of a chosen component, e.g. component A. The most stable phases form a convex hull which at  $T=0$  consists of lines connecting the lowest points. At higher temperatures this would be the convex enthalpies as function of  $x$  properly connected with common tangents, according to the construction of stable phases in physical chemistry. The structures, which span the convex hull dominate the phase behaviour of the system and form the ground state structures. For a mole fraction  $x_0$  between the fixed points the stable phase is a mixture of the phases left and right from  $x_0$  according to the thermodynamic lever rule. Also the stability relation between the different ground state structures can be extracted from the diagram. In the example shown figure 2.2 the structure at  $x_A=0.5$  shows higher stability than the one at  $x_A=0.75$ .

In the selfconsistent fitting procedure of the Cluster Expansion shown in section 2.7 the ground state diagram will be determined in every iteration. Its importance lies in finding new possible ground state structures which could be added to the DFT-derived input set. Such a new ground state structure is determined by calculating the enthalpy of formation with the fitted effective cluster interaction energies (see section 2.6.1) and inserting the thus estimated enthalpies into the ground state diagram as determined by the DFT input structures. If such a newly estimated formation enthalpy lies below the convex hull it is characterized as a new ground state structure. The Cluster Expansion is considered to be converged when the ground state line does not change anymore after the next iterations.

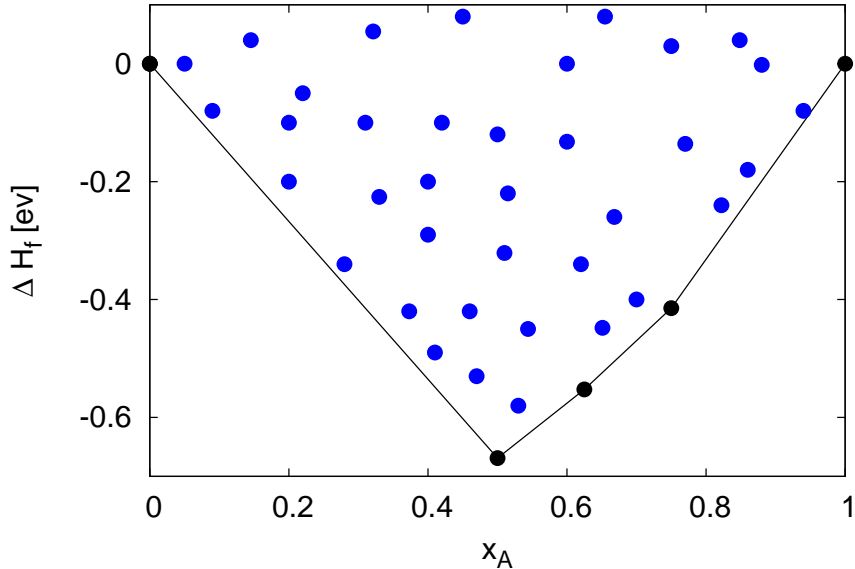


Figure 2.2: Sketch of a ground state diagram. The black circles represent the ground state structures. Connecting the ground state structures results in the ground state line or diagram. The blue dots are other phases, which are thermodynamically not stable.

## 2.6 The Cluster Expansion

Modern DFT methods are able to calculate material properties with reasonable to high precision (depending on the quality of the approximations to the exchange and correlation effects, see section 2.7). Standard DFT applications are, however, restricted to unit cells of a few hundreds of atoms. If one wants to model an alloy with varying atomic concentrations and crystal structures a huge number of very large supercells would be needed, if one tries to solve this problem in a brute force way. Such a procedure is, of course, not feasible. A successful strategy to overcome this limitation is offered by the cluster expansion (CE) [16] in particular when combined with Monte Carlo simulations. The concept of CE is to describe every configuration dependent property of a system by a linear combination of interacting building blocks or figures. By configuration one understands a distribution of atoms over a given lattice. Then the energy for a given configuration  $\sigma$  is written as a sum over pairs, triplets, quadruplets, and so on, the so-called *figures* or *clusters*. It was shown [16] that such an expansion exists if –mathematically– the expansion goes over all configurations (i.e. atomic distributions). For practical reasons the expansion has to be limited to reasonably small clusters, so that the expansion converges numerically. If the input of a convergent cluster expansion is provided by DFT calculations, then the accuracy of DFT calculations can be carried over to systems consisting of  $10^4 - 10^6$  atoms. Many studies were made for binary bulk systems (e.g. [17–20]).

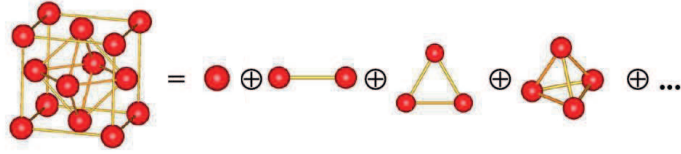
Ternary systems (or binary systems with vacancies) (e.g. Refs, [21] or [22]) are still rather scarce because of the effort they need. More detailed information about CE can be found e.g. in the PhD theses of Lechermann [23] and Wiekhorst [24] with application to bulk as well as surface systems.

### 2.6.1 Basic principles of the Cluster Expansion

The cluster expansion (CE) is based on an Ising Model [25] for modeling the Hamiltonian. A 'pseudo' spin  $S_i$  is defined which characterizes the atom type at each lattice site  $i$ . The spin variables are  $S_i=1,-1$  in a binary and  $S_i = -1, 0, 1$  in a ternary system (see figure 2.4). The distributions of spins over the lattice of a structure represents the configuration  $\sigma$ . In general, CE can be expanded up to any number of species. The configuration space grows, however, fast with the number of atomic species involved. because for a binary case with  $N$  lattice sites  $2^N$  configurations are possible which even grows up to  $3^N$  in a ternary system, and so on. Because of the need of a sufficient number of input structures the number of required DFT calculations grows roughly in the same way. The present work focuses on the modeling of three binary (NiAl,AlFe and NiFe) and a ternary system (FeNiAl) based on a bcc-lattice. Although elemental Al and Ni crystallize in a fcc lattice, fcc-structures and others were not considered for the CE because the main interest of this work is on Fe-rich alloys, for which the bcc structure dominates the phase diagram. In the binary case atom type A is characterized by the spin -1 and atom type B by +1. Any physical property of the system, which is dependent on the atomic configuration  $\sigma$  can now be described by a sum of spin products, as written in equation (2.25). An example for such a property is the energy or enthalpy of formation, but also other observable properties can be cluster expanded such as tensorial quantities [26], Curie temperature [27] and density of states [28]. For fitting and finding the optimum set of figures, the energy or enthalpy of formation is much better suited because they have to reach a minimum.

$$E(\sigma) = J_0 + \sum_i J_i S_i + \sum_{i<j} J_{ij} S_i S_j + \sum_{i<j<k} J_{ijk} S_i S_j S_k + \dots \quad (2.25)$$

The parameters  $J_i$  in equation (2.25) are the so-called *effective cluster interactions (ECI)*, which are of the same dimension as the expanded property.  $J_0$  stands for the empty figure, which serves as a constant value. The ECIs are independent of the configuration  $\sigma$  and contain the properties of the figures as determined by the spinproducts. The approach of calculating a configuration dependent property in this way is exact in principle. Of course, in practical applications it has to be truncated and its convergency has to be tested. The precision of the CE fit is then dependent of the number of terms used in the sum. Practical calculations show that in standard case the sum can be truncated at rather small cluster sizes maintaining the precision of the DFT input energies. Typical



$$E = \Pi_1 \cdot J_1(\bullet) + \Pi_2 \cdot J_2(\bullet\text{---}\bullet) + \Pi_3 \cdot J_3(\triangle) + \Pi_4 \cdot J_4(\text{tetrahedron}) + \dots$$

Figure 2.3: Sketch of the cluster expansion procedure and its mathematical formulation. The structure is decomposed into a set of clusters (or figures). The energy  $E$  of a configuration is a sum over interacting cluster, whereby their geometry is described by  $\Pi_i$  and their (effective) interaction energy by  $J_i$ . These energies are independent of the configuration, whereas the selection of figures (i.e. the summation) depends on it. If the summation runs over all possible clusters the cluster expansion yields the exact result. In practice, this sum is truncated to reasonably small clusters, which has reached numerical convergency.

values for the accuracy of the fit are a few meV per atom. As a short remark, the CE can also be extended for surface alloys. [29] Then, such an expansion has to be made for each layer of the material. Another and very important new development is to make the ECIs temperature dependent, which is the case when free energies of lattice vibrations are included. [30, 31]

### Expanding the basis for ternary systems

In a binary CE approach the desired property of the system can be determined by using the spinproduct as a basis (as shown in equation (2.25)). In a ternary CE the spinproduct is conveniently replaced by a orthogonal basis set which is constructed by Chebyshev polynomials  $\Theta_n$  of order  $n$ , for which their arguments are the spin variables [16],

$$\Theta_0 = 1, \quad \Theta_1(S_i) = \sqrt{3/2} * S_i \quad \Theta_2(S_i) = \sqrt{2} - 3/\sqrt{2} * S_i^2 \quad (2.26)$$

From now on, we will use the term "figure" instead of "cluster". The spinproduct of a figure  $f$  used in equation (2.25) for the binary case is now replaced by the product of polynomials on each lattice site which is occupied by spin  $S_i$ ,

$$\Pi_{f,s}(\sigma) = \Theta_{s_1}(S_1) \cdot \Theta_{s_2}(S_2) \cdot \dots \cdot \Theta_{s_n}(S_n). \quad (2.27)$$

The vector  $s$  has components  $s_j \in \{1; 2\}$ , which designate the order of the polynomial. The number of factors  $n$  is equal to the number of lattice sites (or so-called vertices)

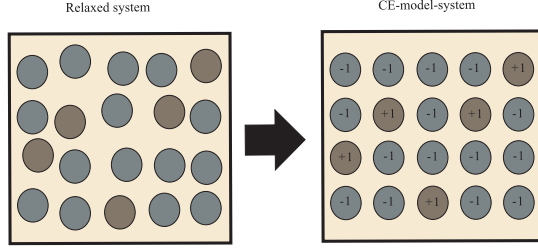


Figure 2.4: Schematic picture of mapping a physical configuration in terms of a relaxed structure (left panel) with a given atomic occupation (circles with different colours) onto the virtual lattice (right panel), which is then decomposed into the clusters or figures of the CE. The atom types in the CE fit are defined as the spin variable  $S_i = -1, +1$ . A basic lattice type (e.g. bcc) has to be chosen for both of the systems. Structural relaxations (see left panel) are allowed if they are not too large: the CE converges also for the given set of relaxed structures, see discussion in the text.

which belong to a figure  $f$ . By making use of  $\Theta_{s_j}$  each figure can now be described by a different basis. For example the correlation function of the figure with one vertex  $\Pi_{1,s}$  describes two different characteristics:

- $\Pi_{f,(1)}$  describes correlations only between atom types with spin -1 and 1, since the atoms with  $S_i=0$  do not contribute because the Chebyshev polynomial of first order is zero. If atoms are labelled by A,B,C and their occupation variables are -1,0,+1 in respective order, then only correlations between A and C atoms are described.
- $\Pi_{f,(2)}$  describes correlations between all three atoms, because the Chebyshev polynomial of second order is different from zero for  $S_i=0$  and  $|S_i|=1$

In a ternary system, the maximum number of figures with  $k$  vertices or lattice sites is  $3^k$  possibilities. This can be reduced if clusters are equivalent because of symmetry. Summing over all figures  $f$ , the Hamiltonian has now the form

$$E(\sigma) = J_0 + \sum_f J_f \cdot \Pi_{f,s}(\sigma) \quad (2.28)$$

with the configuration dependent spin products  $\Pi$  and the configuration *independent* effective cluster interaction energies  $J$ .

The main task of the CE consists in getting the effective cluster interactions  $J_f$  (ECI) connected to each figures  $f$ , as sketched in figure 2.5. The correlation functions can now be symmetrized for a set of symmetry equivalent figures,  $\bar{\Pi}_F(\sigma)$

$$\bar{\Pi}_F(\sigma) = \frac{1}{ND_F} \sum_{f \in F} \Pi_f(\sigma) \quad (2.29)$$

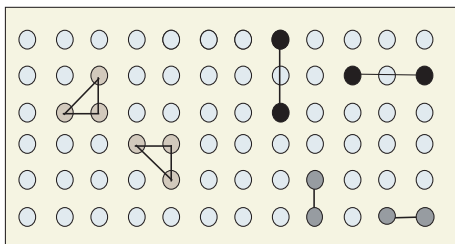


Figure 2.5: Example of figures in a two dimensional lattice. Two dublets and a triplets are shown in two different but symmetry equivalent arrangements.

where  $D_F$  is the number of symmetry operations by which the clusters  $f \in F$  are related. Now, the summation runs over all  $F$  symmetrized spin products. For the sake of normalization one divides by the number of lattice sites  $N$  as used in the actual CE. The energy of a certain configuration  $\sigma$  is now decomposed by the expansion

$$E(\sigma) = N \sum_F D_F J_F \bar{\Pi}_F(\sigma) \quad (2.30)$$

Because of the given lattice the correlations  $\bar{\Pi}_F$  are known and can be constructed. What is not known are the ECIs  $J_F$ . The main task is now to calculate the ECIs. This is done by DFT calculations for the configuration dependent property of interest (e.g. the formation energy  $E_{DFT}$ ) for suitably selected compounds with a given structure and fitting these results to the corresponding CE for each configuration (=compound). The quality of the CE strongly depends on the quality of the fitting, for which sophisticated selfconsistent procedures were developed [1]. These fitting procedures are based on a least square fit,

$$\sum_{N_\sigma} |E_{DFT}(\sigma) - N \sum_{N_F} D_F J_F \bar{\Pi}_F(\sigma)|^2 = \min. \quad (2.31)$$

## 2.7 The UNCLE-code

All the CE calculations of the present work were done by making use of the program package UNiversal CLuster-Expansion (UNCLE) [1] which was developed by the group of S. Müller, now at the Technical Univeristy of Harburg-Hamburg. The code is able to perform a complete CE-fit using a genetic algorithm and to predict the ground states of systems containing up to three and more elements. For deriving results for temperatures  $T \neq 0$  Monte Carlo simulations are implemented (as discussed in section 2.8). By



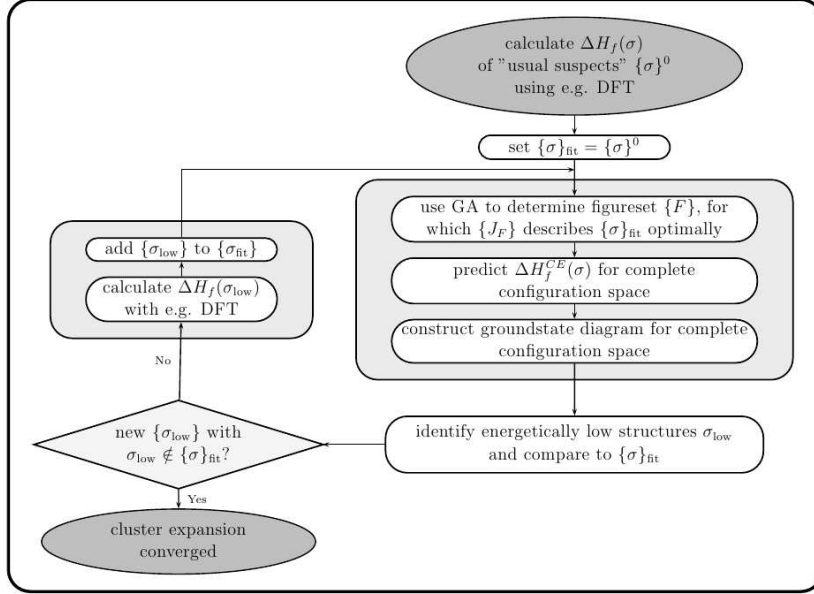


Figure 2.6: Selfconsistent working plan as used by UNCLE for the cluster expansion for finding new input structures [1]

this, configurational entropies are taken into account. The working scheme for a cluster expansion is sketched in figure 2.6.

### 2.7.1 Selecting the input structures

A very important task of a convergent CE is to guarantee that the figures, that are chosen are not biased by the set of input structures. To prevent a wrong interpretation of the whole system by choosing the wrong input, UNCLE uses the chosen figure set to fit the energy of other structures. New structures can now be designed and if they lie energetically below the existing ground state line they are recalculated by DFT, providing a new set of input structures. Then, a new set of figures is fitted and the procedure repeated. Such an iterative approach has the advantage that a reliable ground state line can be achieved together with a figure set which yields accurate results.

### 2.7.2 Determination of the ECIs

Equation (2.31) shows the basic procedure for deriving the set of ECIs. However in practice this procedure has to be modified for efficiency reasons by giving smaller figures a larger weight. The expression is extended by a damping term.

$$\sum^{N_\sigma} (E_{DFT}(\sigma) - \sum^{N_F} D_F J_F \bar{\Pi}_F(\sigma))^2 + \sum^{N_F} f_F J_F = \min \quad (2.32)$$

$f_F$  is the damping factor, which lowers the importance of figures containing more atoms. It is defined by the mean spatial extension  $r_F$  of pairs and multiplets by

$$\begin{aligned} f_F &= c_1 r_F^{\lambda_1} && \text{for pairs} \\ f_F &= c_2 r_F^{\lambda_2} && \text{for multiplets} \end{aligned} \quad (2.33)$$

By variation of the parameters  $c_i$  and  $\lambda_i$  the importance of the different cluster sizes can be scaled. An example of the importance of figures containing more atoms is a system with strong relaxation of the structures.

To select the figures for a (hopefully) convergent CE two possible techniques can be applied.

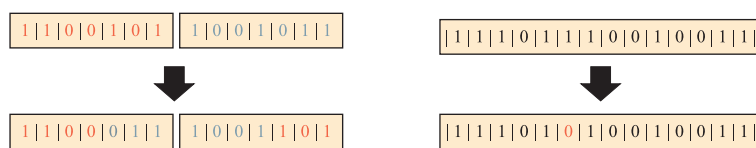
- **Hierarchical approach:** Figures including a smaller number of atoms get a higher weight in the determination of configuration dependent properties. In the method from Zarkevich and Johnson [32] the figures are listed by their dimensions. A maximum extension for the figures is chosen and the figures, which exceed this limit are neglected. The disadvantage is that this approach needs a large number of smaller figures in the final set. Since strong relaxations are better described by larger figures with more vertices, the final figure set needs to contain every partial figure of the set, which build up the more extensive ones.
- **Selective approach:** A large pool of figures is generated. Using convenient algorithms the best set of these figures can now be chosen. The quality of the figure set is defined by the so-called *Cross validation score* (CVS)  $S_{CV}$ . For its calculation first a set of input structures ( $N_{fit}$ ) is determined which is taken for fitting the ECIs, and then a set of structures ( $N_{pred}$ ) for predicting energies for structures different from the input set. These are now used for testing the convergency. The energy of the test set is calculated by the CE of equation (2.31) and compared to the input DFT energies. By repeating these scheme and changing both sets  $n$  times – so such that every structure has been predicted at least once – the cross validation score can be defined as the mean error in prediction over all  $n$  sets.

$$S_{CV} = \sqrt{\frac{1}{nN_{pred}} \sum^n \sum^{N_{pred}} |E_{DFT}(\sigma) - E_{CE}(\sigma)|^2} \quad (2.34)$$

The procedure is considered to be convergent if CVS is smaller than a given value; for energies such values are 1 – 2 meV per atom.

### 2.7.3 The genetic algorithm

UNCLE uses a selective approach with a genetic algorithm (GA). It was first described in 1975 by J. H. Holland in his book *Adaption in natural and artificial systems* [33].



(a) Crossing: Parts of the parent individua are exchanged to form children. (b) Mutation: Single bits of the individuum are switched

Figure 2.7: Operational scheme of the genetic algorithm for creating a new generation of children from their parents. An individuum is represented by a chain of bits, i.e. a sequence of the numbers 0 and 1. After determining the fitness values (for a CE these are the cross validation scores) of a population the fittest individua (described by the binary chains) are mated by exchanging parts of their binary chain (left panel). In a next step the fittest individua are taken and bits are switched randomly (right panel).

The basic principle is the *survival of the fittest*. Like in nature the weaker elements of a fitting set are replaced by other in a stochastic way until the fittest *population* evolves. At the start of a GA-run a starting population is defined in terms of *individuals*, which are possible solutions of the problem. In a CE an individuum would be a set of figures, appropriate for the given structure and number of atoms. A binary chain is used to code these individuals according to figure 2.7. The figures used in such a binary chain are determined by 1, the ones neglected by 0. Each solution is now examined according to its fitness, which in the CE is determined by the value of its cross validation score. Depending on the fitness of a set of individuals a new generation of individuals is created in two ways:

- **Crossing:** Two *parent* individuals are used to produce two new *children*. This is done by exchanging pieces of the chains with the two different binary codes of the parents. The cutting points are chosen randomly way. The idea behind this method is, that good parts (figures that describe the system best) of the individuals binary codes may bond and create a fitter individuum. Usually a *n-point crossover* is done, which means that the chains are cutted in n places. Doing so fitter combinations of the figures are generated, as sketched in the left panel of figure 2.7.
- **Mutation:** One bit of the binary chain, which describes an individuum, is changed as described in the right panel of figure 2.7. The selection of the involved bit is random.

The characterization of the individua can also be done in more complex ways than using a binary chain: for example constructing a chain of rational numbers. In this case the function of mutation and crossing have to be changed. However, for the CE a binary chain is sufficient, because the configurational quantity is defined by a linear combination of the clusters. This means, that a figure occurring in the sum gets a value 1, otherwise its value is 0. Within the concept of a GA the fittest individuuum would be the one containing all the figures, since it would lead to the best fit or  $S_{CV}$ . To avoid such a big figure set a maximal extension of the binary chain is chosen. The selection of the parent individuals, which produce the children for the next generation is done in a stochastic way by the *roulette wheel* method. Every individuuum gets a weight dependent on its  $S_{CV}$ . An individuuum with a better  $S_{CV}$  has then a better chance to be chosen. After crossing the chosen parent individua the children mutate by switching randomly bits of their chains. By that individua, which have a bad cross validation score, are replaced by fitter children. The thus produced individua become now the parents for the next generation.

The end of the genetic algorithm can be defined in two ways:

- Production of an individuuum, which has an  $S_{CV}$  smaller than the one defined before starting the genetic algorithm.
- Determination of a maximum number of GA runs. When these predefined number of runs is finished the best individuuum (death or alive) is chosen as the figure set for the CE. Using this method also the best figure sets can die during the GA: if a set is found, whose value is a local minimum of the  $S_{CV}$  the whole population is killed and substituted by a new one produced randomly. In that way, different starting generations can lead to different minima. The best set is chosen in the end.

#### 2.7.4 Running the Cluster Expansion

After the genetic algorithm has converged a set of figures is chosen to describe the system best. This set predicted all the DFT derived ground state energies of the starting input set and resulted in the lowest  $S_{CV}$ . Structures, which were not members of the input set of the GA run, should now be predicted sufficiently correct. Now, the ECIs –as derived from the fitting– are taken to describe all possible structures of the system on the given parent lattice. If the enthalpy of formation of one of these structures is below the ground state line –as defined by the DFT input data– this structure is included in an enlarged input set. As a consequence, its formation enthalpy is calculated by DFT and added it to the list of input structures. With this enlarged input set a new GA is done. This procedure is repeated until no new ground states are predicted by the CE. As a result, the stable structures of the system are obtained and the final ground state line (for a binary

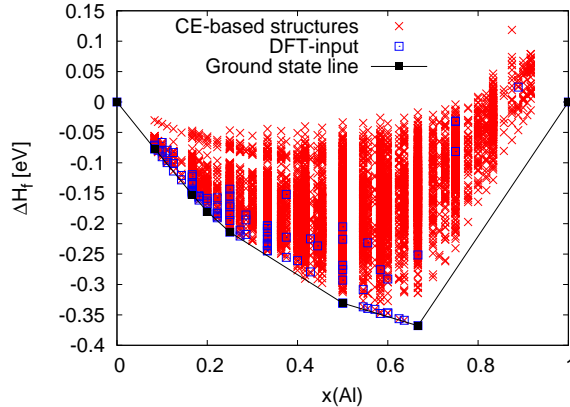


Figure 2.8: Ground state line of the binary AlFe systems for a bcc-parent lattice. Black dots are the structure with lowest formation energies defining the ground state line; blue squares denote the DFT results taken as input for the CE; red crosses represent the energies predicted by CE. The largest unit cells of the predicted structures contained 12 atoms.

system, shown in figure 2.8) or the convex hull (for a ternary system) can be constructed. For calculating phase stabilities at  $T > 0$  Monte Carlo simulations are performed making use of the figures and ECIs of the converged CE.

## 2.8 Monte Carlo simulations

The cluster expansion needs effective interaction energies (ECI), which in the present case were derived from standard DFT calculations. Strictly, speaking DFT total energies are only valid for  $T=0\text{K}$ . To include temperature effects one might think first about configurational entropies, which in this work are included by performing Monte Carlo calculations based on the cluster expansion ingredients. Another and very important temperature effect comes from vibrational entropies, which can be derived from DFT calculations for suitably selected displacements, like it is currently done by David Reith in his PhD. thesis [30]. This is computationally very demanding in particular for ternary cases, and is far beyond the scope of a diploma thesis. Doing this then the ECI would become temperature dependent and with that also the whole CE. In the present work the Monte Carlo (MC) technique without lattice vibrations is applied.

The Monte Carlo method (MC) is a stochastic method and it is often used for statistical thermodynamics. Its major application consists in the approximation of integrals, the calculation of mean values and the search for global minima in phase space. Since it is often very demanding or even impossible to cover the complete phase space just a

sample of it is taken into account. The choice of this sample is the most crucial point in the simulation. In the so-called simple or naive MC the sample is chosen randomly. This procedure is not very efficient for tasks such as finding a global minimum since the chosen phase points are distributed over the whole phase space. For such a distribution the probability to jump into the global minimum is quite small. An improvement would be a sample of suitably weighted points in phase space, which then leads into the global minimum. In this way, points in phase space with low weight would be neglected. Such an MC simulation is reasonable in describing a thermodynamical system at finite temperatures since the configurational entropy can be derived. For elucidating the application of MC in combination with the cluster expansion (CE) the basic principles will now be explained together with the MC implementation in the UNCLE-code.

### 2.8.1 Random walks and Markov-chains

As already mentioned before the choice of the sample is the crucial point in finding thermodynamic characteristics of the investigated system. The crucial question is, how does the jump from one phase point to the next one happen? MC uses a random procedure for changing the point in the phase space: by applying the so-called *random walk* strategy every point has the same probability to be chosen as the next one to be considered. The corresponding transition probability  $P$  depends now only on the current point in phase space, but not on the  $n-2$  points, which have been chosen before. This description of the transition probability is called a *Markov chain*.

$$P(K_n = i | K_{n-1} = j | \dots | K_0 = l) = P(K_n = i | K_{n-1} = j) = P_{ij}(n). \quad (2.35)$$

Assuming that each transition probability  $P$  can be written as  $P_{ij}(n)$  a matrix which contains the transition into each point of phase space can be defined as

$$\mathbf{P} = \begin{pmatrix} P_{11} & \dots & P_{1K} \\ P_{21} & \dots & P_{2K} \\ \vdots & \ddots & \vdots \\ P_{K1} & \dots & P_{KK} \end{pmatrix} \quad (2.36)$$

This matrix has to fulfill two conditions, because it is stochastic, namely:

1. Because the matrix elements are probabilities, all the components have to be positive,  $P_{ij} \geq 0$ .
2. The probability to *change* position in phase space has to be 1, which means  $\sum_{j=1}^K P_{ij} = 1$ , with  $i$  being the current point and  $K$  being the number of points in phase space.

The next step in the random walk through phase space consists in defining the stationary probabilities of a point  $i$  to be populated after  $n$  steps:

$$w_i(n) = P(K_n = i) \quad (2.37)$$

Now the stationary probability vector  $\mathbf{w}(n)$  is defined whose components are the probabilities of arriving at each point of the whole phase space,

$$\mathbf{w}(n) = (w_1(n), w_2(n) \dots w_K(n))^T \quad (2.38)$$

This vector has to fulfill again the conditions rules as the transition matrix  $\mathbf{P} \equiv P_{ij}$ . Knowing the probability  $w$  of a given point in phase space for step  $n$  the probability for step  $n+1$  is then defined as

$$w_j(n+1) = \sum_{i=1}^K w_i(n) P_{ij}, \quad (2.39)$$

which –in a matrix notation– looks like

$$\mathbf{w}(n+1) = \mathbf{P}\mathbf{w}(n) \quad (2.40)$$

The vector  $\mathbf{w}$  can now be constructed for  $s$  following steps by

$$\mathbf{w}(n+s) = \mathbf{P}^s \mathbf{w}(n) \quad (2.41)$$

which for  $n=0$  is

$$\mathbf{w}(s) = \mathbf{P}^s \mathbf{w}(0) \quad (2.42)$$

At this point the probability distribution over the whole phase space after  $s$  steps can be predicted by knowing the probabilities of the points in phase space being populated and the transition probabilities at the start. Since in a random walk approach every step has the same probability, until now each element of the transition matrix and the stationary probability vector have the form

$$P_{ij} = \frac{1}{K}, \quad w_i = \frac{1}{K} \quad (2.43)$$

In order to construct an efficient algorithm a weight for the transition to different points in the phase space has to be implemented.

## 2.8.2 The Metropolis Rosenbluth algorithm

A still valuable method for MC simulations is the algorithm proposed by *Metropolis and Rosenbluth* by which already in the year 1953 a system of 32 hard spheres was simulated. This approach is still used nowadays. The transition probability in the Metropolis-Rosenbluth algorithm is defined to be dependent on the stationary probabilities,

$$P_{ij} = \begin{cases} \frac{1}{K} & \text{if } w_j > w_i \\ \frac{1}{K} \frac{w_j}{w_i} & \text{if } w_j < w_i \end{cases} \quad (2.44)$$

The random walk probability is still present in the factor  $\frac{1}{K}$ , but the transition rate  $P_{ij}^*$  in the calculation can now be defined as an accepted step and a neglected step by just comparing the fraction  $\frac{w_j}{w_i}$  to a random number  $\epsilon$  between 0 and 1.

$$P_{ij}^* = \begin{cases} 1 & \text{if } \epsilon < \frac{w_j}{w_i} \\ 0 & \text{if } \epsilon > \frac{w_j}{w_i} \end{cases} \quad (2.45)$$

For  $w_j > w_i$  the fraction in equation (2.45) is always larger than 1 and therefore the step will always be accepted.

For starting a simulation a definition of the stationary probabilities  $w_i$  is needed. Since the energy of a system is often the property of interest in most of the cases a Boltzmann distribution is used to weight the points in phase space,

$$w_i = \frac{e^{-E(x_i)/k_b T}}{\sum_{i=1}^K e^{-E(x_i)/k_b T}} \quad (2.46)$$

The symbols in this equations are the *Boltzmann constant*  $k_b$ , the energy  $E(x_i)$  at the point  $x_i$ , the total number  $K$  of points the phase and the temperature  $T$ . Within the Metropolis- Rosenbluth-algorithm the transition rates  $P_{ij}^*$  to a randomly chosen point is defined by

$$P_{ij}^* = \begin{cases} 1 & \text{if } \epsilon < e^{-(E(x_j)-E(x_i))/kT} \\ 0 & \text{if } \epsilon > e^{-(E(x_j)-E(x_i))/kT} \end{cases} \quad (2.47)$$

Analogous to the case described in equation (2.45), the transition will be accepted if the energy of the point reached after the transition is smaller than the one for the starting point, because the Boltzmann factors in relation (2.47) is larger than 1. If the energy of the reached point is higher then one of the previous point it is compared to a random number between 0 and 1: if the value is larger than  $\epsilon$  the step is accepted. Due to this procedure local minima on the potential surface can be left.

### 2.8.3 Implementation of the MC simulation in the UNCLE code

In the UNCLE code a MC calculation with a grandcanonical and a canonical ensemble is possible. The system the calculation is dealing with is a box of atoms with a given extension and it obeys periodic boundary conditions: the box is a unit cell. For both the grandcanonical and the canonical calculation different implementations are made, as illustrated in figure 2.9.

#### Grandcanonical ensemble

In a grandcanonical ensemble the system can be seen as the crystal of interest, which is connected to a reservoir of atoms that can propagate into the system. The total number



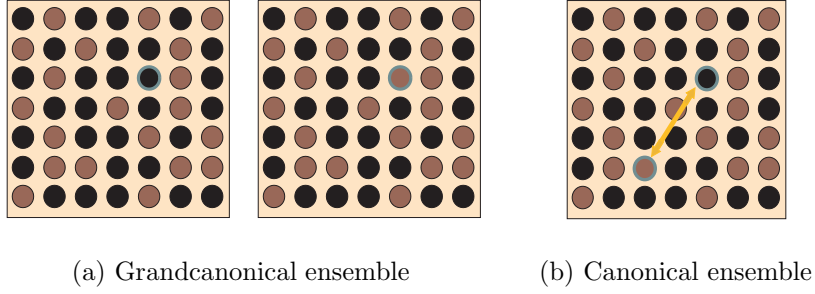


Figure 2.9: Visualization of a MC step in UNCLE. In the grandcanonical simulation the type of one atom in the crystal is changed, in the canonical approach the positions of two atoms in the crystal are changed. In both cases the Boltzmann distribution of the old and the new system are calculated and compared to decide if the transition is made or not.

of atoms in the simulation box has to stay constant, which means that if an atom is added into it another one has to be removed. The thermodynamic which controls the propagation of the atoms in and out of the box is the chemical potential  $\mu$ . If the chemical potential of one atom type in the system is raised, then the number of atoms of this type will be decreased. The reason for that is that if one atom (e.g. atom A) is removed from the system and another one (e.g. B) is added then the chemical potential changes by  $\Delta\mu = \mu_A - \mu_B$  with  $\mu_i$  being the chemical potentials for the atomic species. The transition rate for changing a configuration  $\sigma$  into  $\sigma'$  is then defined as

$$P_{\sigma\sigma'}^* = \begin{cases} 1 & \text{if } \epsilon < e^{-(\Delta E - \Delta\mu)/kT} \\ 0 & \text{if } \epsilon > e^{-(\Delta E - \Delta\mu)/kT} \end{cases} \quad (2.48)$$

where  $\Delta E = E(\sigma') - E(\sigma)$ . This means, that if the energy of the system after the atom exchange is lowered by a larger amount than the change of the chemical potential then the step will be accepted, otherwise it will be compared to the random number in the usual way as described above. Using the Ising model of the cluster expansion makes it easy to change an atom type at a defined position. The atom is chosen randomly and by changing the spin variable of it the atom type is obviously changed. In the next step the energy of the simulation box is calculated using the ECIs and the energy difference  $\Delta E$  can now be calculated. Since the chemical potentials of the atom types are essential starting parameters  $\Delta\mu$  and the Boltzmann factors are defined as well.

## Canonical ensemble

In a canonical ensemble the conserved quantity is the concentration of each atom type in the simulation box. In each step the position of two randomly chosen atoms is exchanged. Doing so the energy of the composition in box changes and the transition rate can be written as

$$P_{\sigma\sigma'}^* = \begin{cases} 1 & \text{if } \epsilon < e^{-(E(\sigma')-E(\sigma))/kT} \\ 0 & \text{if } \epsilon > e^{-(E(\sigma')-E(\sigma))/kT} \end{cases} \quad (2.49)$$

The random walk through phase space is continued until a chosen number of steps is done or the change in the energy of the system is below a given numerical limit. In the present work the grandcanonical simulations as done for the binary systems were limited to a certain number of steps done. The ternary system was treated canonically with the change of energy as the convergence criterion. The parameters set for convergence will be shown in chapter 4 and section 5.4.

## 3.1 Nickel (Ni)

Ni is a hard silvery-white metal. Its nuclear charge is 28 and the electronic configuration of the free atom is  $[Ar]4s^23d^8$ . Ni has a molar weight of 58.6934 g/mol. Ni metal crystallizes in an fcc-lattice with an experimental lattice constant of 3.524 Å. Because of the unsaturated 3d shell the atoms carry spin magnetic moments. In the metal they are ferromagnetically aligned with a Curie temperature of 355°C. [34]

The need of pure Nickel in industrial application is low in comparison to Fe. It is used for corrosion-resistant surface coverages of metallic substrates and for equipments chemical laboratories because it has a high stain and chemical resistance. Ni surfaces of particles on surfaces are used for catalytic purposes, e.g. for the hydrogenation of fatty acids.

More important than the pure metal are Ni alloys. Most of the produced Nickel is taken to refine steel because of strengthening corrosion resistance and hardness, and improving ductility. The alloy formed of 55% Cu and 45 % Ni known as Konstantan plays an important role in producing accurate resistances, since its electrical resistivity is constant against changing temperatures. Nickel-superalloys are high temperature and corrosion resistant materials composed by Ni and a mixture of other elements with the intention to maximize the melting point (for example: 0.04 % C, 19 % Cr, 3.0 % Mo, 52.5 % Ni, 0.9 % Al,  $\leq 0.1$  % Cu, 5.1 % Nb, 0.9 % Ti, 19 % Fe). Their (future) main application is for turbines needed for aircrafts and gas fired power plants, and for instruments in chemical industry. Further applications are Raney-Nickel for catalysis and Nickel silver (alloys composed of Ni-Cu-Zn) in electronics. This work was also (partially) motivated by technological aspects: NiAl precipitates hardens steel (=Fe) and NiAl alloys with additions of Fe belong to the class Ni-alloys as described above.

### 3.1.1 DFT results

Metallic Ni element was studied by applying VASP with PBE and LDA pseudopotentials. The fcc as well as the bcc structure was studied. In the PBE pseudopotential 16 (valence)

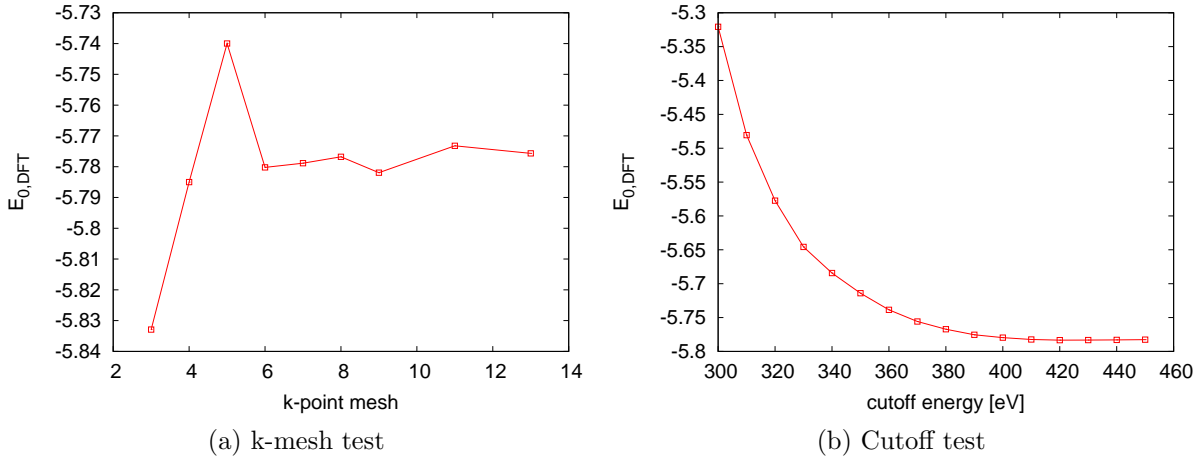


Figure 3.1: Convergency tests for fcc ferromagnetic (FM) Ni using the PBE pseudopotential. panel (a): varying  $\mathbf{k}$ -point meshes with a fixed basis function cutoff of 490 eV. A  $7 \times 7 \times 7$  Monkhorst Pack  $\mathbf{k}$ -point set [35] is found to be sufficient; panel (b) varying cutoff for a fixed  $7 \times 7 \times 7$  mesh. A cutoff of 400 eV yields sufficiently accurate results.

electrons have been calculated explicitly regarding the 3p, 3d and 4s atomic orbitals. The calculations done with the LDA pseudopotential just computed 10 electrons explicitly regarding only the 3d and 4s atomic orbitals. The optimized cutoff for the plane wave basis functions was 400 eV, and a  $7 \times 7 \times 7$   $\mathbf{k}$ -point mesh was found to be sufficient, (see figure 3.1.1).

The resulting ground state properties are listed in table 3.1. As expected, the DFT results for the GGA-PBE calculation agrees well with experiment. The ground state as derived from the minimum of the total energy as a function of volume was determined to be fcc-ferromagnetic with the cubic lattice parameter  $a=3.52 \text{ \AA}$ . The LDA calculation overestimates the binding, which in particular is noticeable for 3d transition metals: because of that the optimized lattice parameter is 3% smaller than experiment. Nevertheless, also for the LDA calculations the ferromagnetic fcc state is the ground state.

	Structure	a [rÅ]	$\Delta E_0$ [eV/atom]	$\mu$ [ $\mu_B$ ]
PBE	bcc FM	2.802	0.103	0.48
	bcc NM	2.793	0.116	
	fcc FM	3.520	0	0.58
	fcc NM	3.515	0.050	
LDA	bcc FM	2.720	0.103	0.42
	bcc NM	2.722	0.115	
	fcc FM	3.420	0	0.51
	fcc NM	3.418	0.05	
Exp.	fcc FM	3.5241*		0.62*

Table 3.1: Ground state properties of Ni calculated with VASP for bcc and fcc structures with ferromagnetic (FM) ordering and without spin polarization (NM). Two approximations for the exchange-correlation interaction are studied: a GGA type (PBE; [9]) and an LDA type [8] potential. The quantities in the table are the lattice parameter (a), the energy difference ( $\Delta E_0$ ) relative to the ferromagnetic fcc ground state, and the magnetic moment  $\mu$ . As a cutoff energy of 400 eV and a  $\mathbf{k}$ -point set of 7x7x7 have been determined to give reasonable results for Ni. The last line shows experimental values. [34]

## 3.2 Aluminium (Al)

Aluminium is a silvery white, light metal with a nuclear charge of 13 and the electron configuration of the free atom of  $[Ne]3s^23p^1$ . It crystallizes in the fcc structure. Al is widely used in technology, because of its remarkable low density and its ability to form a passivation layer on its surface: Al is used to produce light weight and corrosion resistant materials. Pure Al is rarely needed but its alloys are important. Al alloys are part of the modern life, they are used for automobiles, cans, foils, window frames, construction material, and so on. Nevertheless its low fatigue strength, leads to Al alloys with a relatively low lifetime. In spite of its low melting point of 660°C Al occurs in materials which are used for aircraft and rocket engines, because it forms high temperature stable alloys with transition metal elements, such as NiAl (as will be also studied in this work) with a melting point of 1680°C.

### 3.2.1 DFT results

Table 3.2 presents the results of the search for the ground state. As for Ni, the calculations were done with both the PBE and LDA pseudopotentials. Three electrons with a (valence) electronic configuration of  $3s^23p^1$  were computed explicitly in both the pseudopotentials. Again as expected for lighter elements the GGA (PBE) approximation is superior to

LDA, because it yields more reliable ground state properties, e.g. the calculated lattice parameter for fcc Al of 4.03 rA, is in accordance with the experimental value of 4.05 rA [36] The determination of the best  $\mathbf{k}$ -point set and the cutoff energy was done for the PBE pseudopotential. A mesh of 11x11x11 point was found to be optimal, and for the cutoff energy a value of 450 eV was chosen.

	Structure	a [rA]	$\Delta E_0$ [eV/atom]
PBE	bcc	3.325	0.085
	fcc	4.03	0
LDA	bcc	3.189	0.097
	fcc	3.980	0
Exp.	fcc	4.05	

Table 3.2: VASP results for the ground state properties of Al with a cutoff of 450 and a  $\mathbf{k}$ -point mesh of 11x11x11 using the PBE pseudopotential. For the bcc as well as the ground state fcc structure the lattice parameter  $a$  and the total energy difference with respect to the fcc ground state energy is presented. Experimental value according to reference [36]

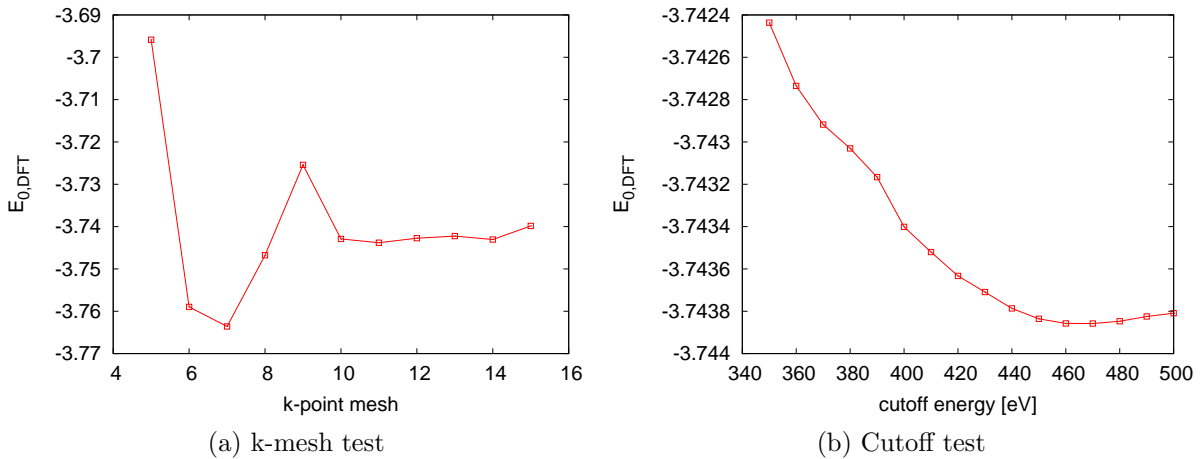


Figure 3.2: VASP convergence tests for the fcc ground state of Al. panel (a): the optimized  $\mathbf{k}$ -point set is searched for a fixed cutoff of 500 eV and the 11x11x11 Monkhorst Pack mesh [35] is the result. panel (b): the optimal cutoff energy is determined for a fixed 11x11x11 mesh. Its optimal value is 450 eV.

## 3.3 Iron (Fe)

Iron is a silver ductile metal with a nuclear charge of 26 and the electron configuration  $[Ar]3d^64s^2$ . In the ground state ( $\alpha$ -Fe) its crystal structure is bcc with ferromagnetically aligned spin moments. Its large magnetic moment of  $2.22 \mu_B$  (experimental value) is the consequence of the large number of unpaired  $3d$  electrons. There are at least four allotropic forms of iron, depending on temperature and pressure. The most important ones at ambient pressures are the  $\alpha$  and the  $\gamma$  phase. The bcc  $\alpha$  Fe or Ferrite is ferromagnetic with a Curie temperature  $T_C$  of  $910^\circ\text{C}$ . Its lattice parameter is  $2.86 \text{ \AA}$  [37]. Above  $T_C$  up to  $1397^\circ\text{C}$   $\gamma$  Fe or Austinite is stable with an fcc structure and the lattice parameter of  $a=3.65 \text{ \AA}$ . Its magnetic properties are still under discussion. DFT calculations allow no conclusion either. First principle calculations done by Paduani and Silva have proposed an antiferromagnetic ordering at  $T=0$ , with spin alternating layers in the crystal [38]. Both Fe phases are of great interest for steel industry and technology. Steel is a very important material used in many ways. At temperatures between  $1670\text{K}$  and its boiling point ( $1808\text{K}$ ) the fcc- $\gamma$ -iron changes into a bcc crystal again and  $\delta$ -iron ( $\delta$ -Ferrite) is formed. An experimental Fe-C phase diagram, which is important for steel fabrication, can be found in reference [39].

### 3.3.1 DFT results

Fe was calculated in both the bcc and fcc structure with PBE and LDA pseudopotentials. In both the pseudopotentials seven electrons in the  $3d$  orbitals and one electron in the  $4s$  orbital have been calculated explicitly. Using a PBE pseudopotential Fe the ground state is bcc in contrast to LDA, which yields an fcc ground state. Actually, the crass LDA failure for Fe was one of the major driving forces for the application and development of GGA potentials, such as PBE. The PBE derived lattice parameter is  $2.83 \text{ \AA}$  and for the ferromagnetic ordering a magnetic moment of  $2.17 \mu_B$ , is obtained which agrees well with experiment, see table 3.3. As mentioned, LDA leads to a wrong structure for the ground state with its magnetic configuration rather undefined. A theoretical improvement can be obtained by the so-called LDA+U approach as applied by Zhu et al. [40]. Within LDA+U the  $d$ -states are considered to be strongly localized and their (high) correlation is included by the Coulomb interaction parameter  $U$ .

The optimum  $\mathbf{k}$ -point mesh was determined to be  $9 \times 9 \times 9$ . For the cutoff energy a value of  $450 \text{ eV}$  is suitable (see figure 3.3).

	Structure	lattice constant [rÅ]	$\Delta E_0$ [eV/atom]	magnetic moment [ $\mu_B$ ]
PBE	bcc FM	2.834	0	2.17
	bcc NM	2.756	0.047	
	fcc FM	3.483	0.137	0.99
	fcc NM	3.445	0.142	
LDA	bcc FM	2.754	0.091	2.01
	bcc NM	2.690	0.34	
	fcc FM	3.373	0	0.0
	fcc NM	3.373	0	
Exp.	bcc FM	2.866		2.22

Table 3.3: VASP derived ground state properties of Fe calculated with PBE and LDA pseudopotentials. For the fcc and bcc structure ferromagnetic (FM) and non spinpolarized (NM) calculation were made. Experimental values according to [41]. The quantities in the table are the lattice parameter  $a$ , the energy difference ( $\Delta E_0$ ) relative to the ferromagnetic bcc (PBE) and the ferromagnetic/nonmagnetic fcc (LDA) ground state, and the magnetic moment  $\mu$ . For the cutoff energy a value of 450 eV and a 9x9x9 Monkhorst Pack [35] were used.

By analyzing the results the elemental phases the  $\mathbf{k}$ -mesh set for all the the following VASP calculations was 11x11x11, and the cutoff energy  $E_C$  was set chosen to be 400 eV as a basis. The number of used  $\mathbf{k}$ -points was changed depending on the extension of supercell of the calculated structure. If the size of such a cell increased in one dimension the  $\mathbf{k}$ -point set in this direction was decreased by the same scale, since an increase in real space leads to a shortening in the reciprocal space where the  $\mathbf{k}$ -point set is applied. The convergency studies hinted at somewhat larger values for  $E_C$ . However, because of the huge computational effort in particular for deriving the input data for the cluster expansion, a value of  $E_C = 400$  eV is considered to be a good compromise. Furthermore it should be noted, that for the compounds the formation energy is needed which is an energy *difference* and thereby small numerical inaccuracies due to the slightly smaller  $E_C$  will cancel out.



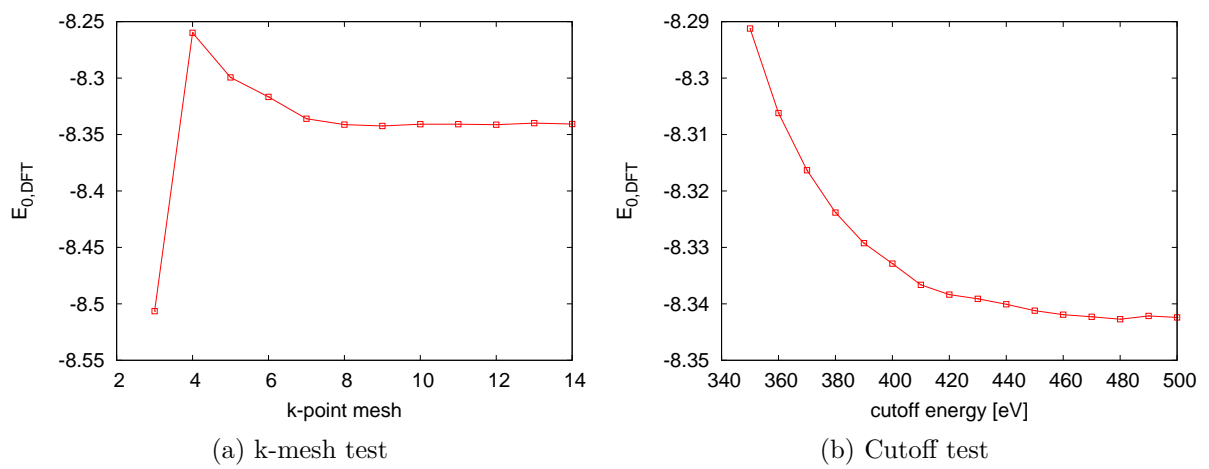


Figure 3.3: Convergence tests for bcc ferromagnetic Fe using the PBE pseudopotential. VASP Convergence tests for fcc ferromagnetic (FM) Ni. panel (a): varying  $\mathbf{k}$ -point meshes with a fixed basis function cutoff of 500 eV. A 9x9x9 Monkhorst Pack k-point set [35] is found to be sufficient; panel (b) varying cutoff for a fixed 9x9x9 mesh. A cutoff of 450 eV yields sufficiently accurate results.



Before starting the full ternary system the respective binary systems have to be studied by searching for the phase stabilities along the sides of the ternary Gibbs triangle. The study was done in the same way as for the ternary system (see chapter 5). A Cluster Expansion (CE) based on a body centered cubic lattice was performed, which yielded the ground state phase diagram of the three binary alloy systems Fe-Al, Ni-Al, and Fe-Ni. Since nickel and aluminium crystalize in a fcc lattice the description in a bcc lattice might seem inappropriate at a first glance. There are two points to consider for justification. Firstly, this work is mostly interested in the study of Fe-rich ternary Fe-Ni-Al alloys, which definitely crystallize in bcc-type structures. Secondly, the binary alloys and compounds of the Ni-Al and Fe-Al system (and a large part of the ternary phases) prefer a bcc-type structure, which are strongly bonding. The most important phase for the present work is NiAl with a B2 (prototype CsCl) structure, which is highly stable and occurs in a wide concentration range of the experimental phase diagram. Concerning the Fe-Al a very stable B2 FeAl phase exists. The only exception is the Fe-Ni system, which shows no tendency to crystallize in a bcc lattice. As a consequence of that the modeling in the present work of the Fe-Ni system has turned out to be rather difficult, because of its very weak stability. More details will be discussed in the next sections.

It should be mentioned, that the CE can be done for any lattice type. Because of that, an fcc lattice type study is also possible. For the final determination of the stable phases the bcc and fcc phase diagrams have to be overlayed, which was and can be done. However, doing the fcc CE requires an effort comparable to the bcc CE. All both of them are beyond the scope of a diploma work.

## Technical details of the Cluster expansions

To start the iterative CE on the binary systems the formation energies of the small-unit cell structures such as B2, B32, and DO<sub>3</sub> in all their modifications for all the three systems were calculated by VASP. The actual number of starting input structures will be shown in the specific sections (sec. 4.1,4.2,4.3). To get the ground state DFT-energies for the relaxed structures the calculations were done in 3 steps:

1. Volume relaxation: In a first step of the VASP calculation only the volume of the unit cell was relaxed but the atomic positions were kept fixed. Doing so the unit cell maintains the given symmetry minimizing the energy as a function of volume. This is important since –even if the unit cells of the DFT calculated structures are relaxed– the symmetry of the bcc structures has to be maintained because the CE can only fit the energy on a given parent lattice.
2. Ion position relaxation: After the equilibrium volume of the cell was determined in the first step the atomic positions were relaxed for the fixed volume maintaining the given symmetry. Combining volume and ion relaxation lead to an almost completely relaxed system.
3. Volume, atomic relaxation and cell shape relaxation: In a final step the volume and ionic positions were relaxed simultaneously. There are two reasons for this step:
  - (a) By further relaxing the system when modifying volume and the atomic positions at the same time the true ground state can be found and taken as input of the genetic algorithm.
  - (b) Comparing the ground state energy after step 2 and step 3 gives an idea of how large the change of the ideal bcc lattice to the relaxed structure is. If the DFT-energy difference between the ideal and fully relaxed structure was larger then 10 meV/atom the energy after step 2 was taken as the CE input.

The thus derived DFT-energies were then used as input data for the fitting in the Cluster Expansion via the genetic algorithm. After the best set of cluster energies was determined the prediction of new structures was done and the structures with an energy below the actual ground state line were re-calculated with VASP to include all the ground states as the CE-input and to enlarge the input set.

After the CE is converged and the ECIs for this set were fitted the final ground state line was searched and the Monte Carlo (MC) simulations in a periodic simulation box were started. A grandcanonical ensemble was chosen for finding the stable phases at elevated temperatures. In a first step the range of the chemical potential difference  $\Delta\mu$  was determined. This range can only be estimated approximately because for the calculation of the internal energy the composition has to be known. As demonstrated in section 2.8.3 the preparation of the ensemble of atoms in the simulation box (meaning the exchange between atom types) is done randomly and a large number of internal energies is calculated, leading to a iterative approach in finding the energy minimum at a given  $\Delta\mu$ . Through the Boltzmann factor the box with minimal energy at the given chemical potentials is found. The chemical potential at this point plays the role of a constant term, which influences the probability of a build up composition to form a minimum in

the energy landscape. The only value of  $\Delta\mu$ , which can be estimated in advance is when  $x_A = x_B$ . This is the same value as the one for the difference of the formation enthalpies containing the pure elements.

After determining the range of the chemical potential difference it was changed in small steps always starting with the final configuration of the step before. The number of MC steps needed for convergence is different for the three binary systems. The actually chosen parameter will be discussed in the sections dealing with the calculations. Six different temperatures have been investigated for each binary alloy: 100K, 250K, 500K, 750K, 1000K and 1200K.

At the end of the MC runs the ordered phases and the slope of  $\Delta\mu$  versus the concentration were used to derive phase diagrams for the corresponding systems.

# 4.1 Nickel-Aluminum

## 4.1.1 Experimental findings

The Ni-Al binary system is a very important system for forming Ni-based superalloys. According to Huang and Chang [42] the well ordered compound  $\text{Ni}_3\text{Al}$  with the fcc-type  $\text{L1}_2$  structure is mainly responsible for the high temperature properties. But this phase has not the the highest melting point ( $\sim 1668$  [43]) of the Ni-Al system, because NiAl with the bcc-type B2 structure has a melting point of  $\sim 1680^\circ\text{C}$  [44] reflecting its high stability. B2-NiAl is often used in the construction of high energy materials in e.g. aircraft turbines because of its high thermal stability and its oxidative resistance. As it is usual for these intermetallic alloys and compounds they are brittle at room temperature [45], i.e. its ductility is poor. The ductility can be raised by adding ternary (or more) elements. [46]. The thermoelastic transition from the B2-NiAl to the  $\text{L1}_0$  phase (tetragonal structure) is used in Ni-based shape-memory alloys [47]. The metastable  $\text{L1}_0$  structure is formed by quenching hot B2-NiAl rapidly. By increasing the temperature the system can return to the B2 phase and vice versa. The transition temperature may be as high as  $900^\circ\text{C}$ , depending on the chemical composition. Fig 4.1 shows the NiAl phase diagram as derived from experimental informations. Seven stable phases are formed:

- fcc Ni-rich solid solution
- fcc Al-rich solid solution
- $\text{L1}_2$ - $\text{Ni}_3\text{Al}$  (fcc-type)
- B2-NiAl (bcc-type)
- $\text{D5}_{19}$ - $\text{Al}_3\text{Ni}_2$  (trigonal)
- $\text{D0}_{20}$ - $\text{Al}_3\text{Ni}$  (orthorombic)
- “ $\text{Ga}_3\text{Pt}_5$ ”-  $\text{Al}_3\text{Ni}_5$  (orthorombic)

Table 4.1 presents the calculated ground state structures of the Ni-Al system. The formation enthalpies of B2-NiAl,  $\text{L1}_2$ - $\text{Ni}_3\text{Al}$ ,  $\text{D0}_{20}$ - $\text{Al}_3\text{Ni}$  and ” $\text{Ga}_3\text{Pt}_5$ ”-  $\text{Al}_3\text{Ni}_5$  were determined by DFT calculations with the PBE potentials. Although the structural data could in principle be optimized by DFT calculations, for the compounds with more complex structures they were taken from experiment, such as  $\text{D0}_{20}$ - $\text{Al}_3\text{Ni}$  [48], “ $\text{Ga}_3\text{Pt}_5$ ”-  $\text{Al}_3\text{Ni}_5$  [49],  $\text{D5}_{19}$ - $\text{Al}_3\text{Ni}_2$  [50].

struc./compound	$E_0/\text{atom}$ [eV]	$\Delta H_{f,DFT}$ [meV]
fcc Ni	-5.783	0.0
$L1_2 - Ni_3Al$	-5.704	-0.435
$Ga_3Pt_5$ - $Ni_5Al_3$	-5.404	-0.393
B2-NiAl	-5.425	-0.670
$D5_{19} - Al_3Ni_2$		-0.660 [50]
$D0_{20} - Al_3Ni$	-4.663	-0.423
fcc Al	-3.725	0.0

Table 4.1: DFT derived total energies per atom  $E_0/\text{atom}$  and formation enthalpies of the ground state structures of the Ni-Al system. The corresponding crystal structure is denoted for each of the compounds.

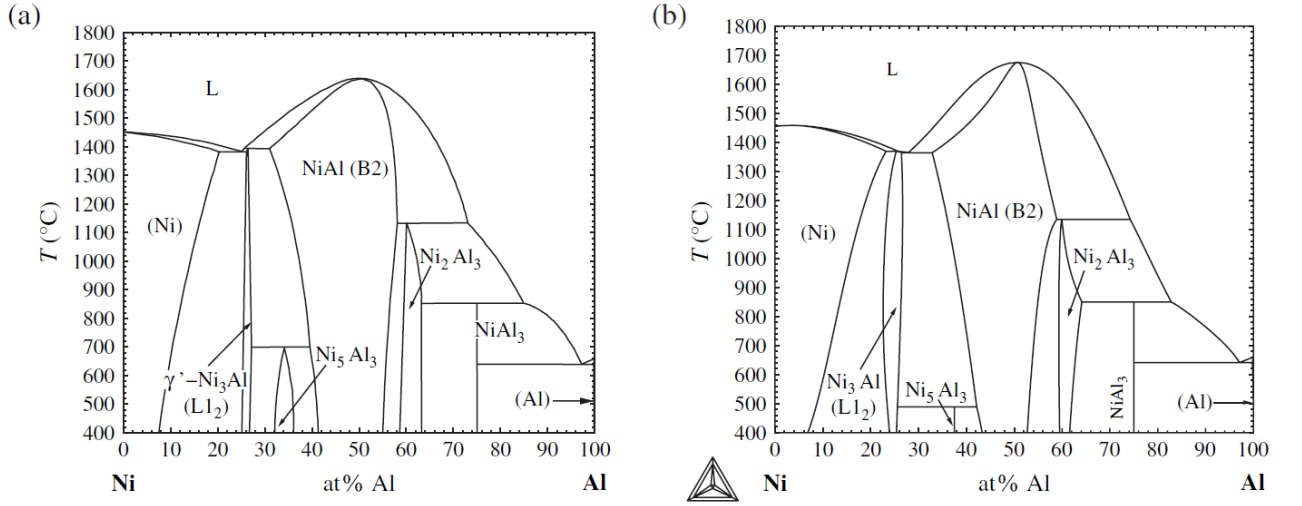


Figure 4.1: Experimental/empirical phase diagrams of Ni-Al: a) collection of experimental data according to Singleton et al. [51], b) CALPHAD derived empirical data. [52].

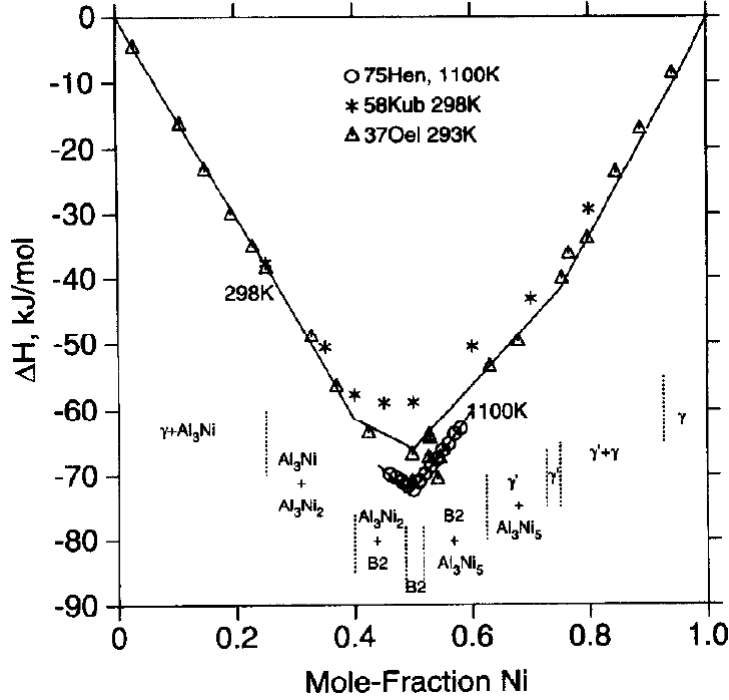


Figure 4.2: Ground state line of the Ni-Al system as derived from model: full lines calculated data of by Huang et al. [42] at 298K and 1100K using a Bragg-William model; symbols are experimental results. [53–55]

#### 4.1.2 Search for the ground states

To start the CE for searching for the ground states of the Ni-Al system the DFT energy formation enthalpies of B2-NiAl,  $D0_3$ -Ni<sub>3</sub>Al,  $D0_3$ -NiAl<sub>3</sub> and B32-NiAl were computed. In addition, 25 other structures -as suggested by the genetic algorithm (GA)- were added. By starting a GA with these structures a cross validation score (CVS) of 15.4 meV per atom was achieved and a new input structure -which was predicted as a ground state by the CE- was chosen in this first run to be calculated with VASP and to be added to the input set. The maximal size of the unit cells for the CE predictions were adjusted during the fitting procedure and finally the largest unit cells contained 12 atoms. When no new ground state structures were found by CE, the system was considered to be converged.

Figure 4.3 shows the progress during minimization of the cross validation score, their deviation from the DFT data and the increase of the number of input structures with the number of GA runs. As can easily be seen after a few starting runs the CVS decreases along with the increase of the number of input structures. The final energy fit was done with an input set of 84 structures and resulted in a CVS of 2.1 meV per atom.

The final ground state line relative to the fcc ground states of the elements and the predicted enthalpies of formation are shown in figure 4.4. The blue squares show the



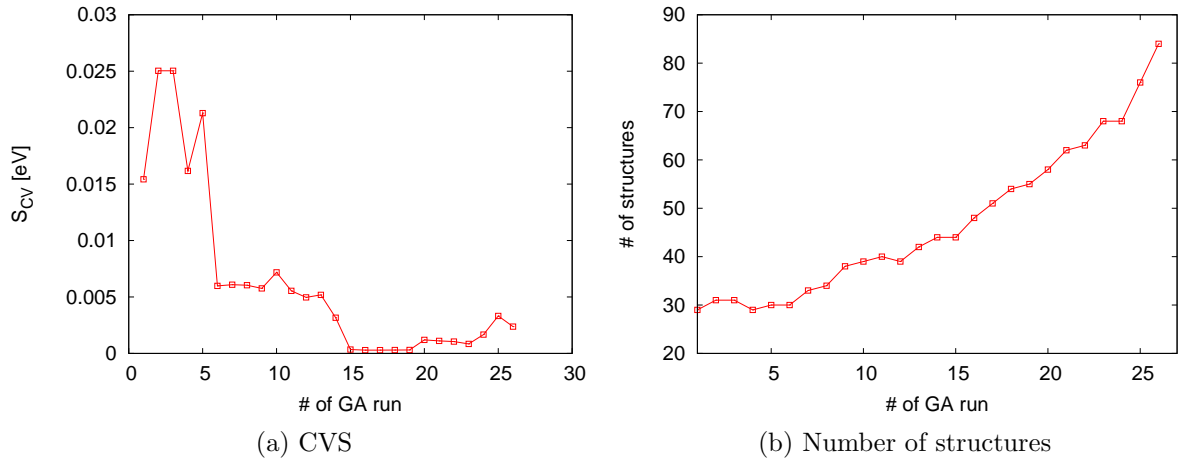


Figure 4.3: Progress of the CE fit for Ni-Al; (a) CVS versus number of GA runs; (b) number of input structures versus number of GA runs.

phases which were predicted as ground state structures in the previous CE runs and which were recalculated by DFT. The ECIs were fitted to these phases and then used for the CE to predict all the possible bcc-type structures with maximal 12 atoms per unit cell (red crosses). The ground state line is characterised by the stable structures of B2-NiAl, Ni<sub>5</sub>Al<sub>3</sub>, Ni<sub>3</sub>Al, whose calculated properties are revealed in table 4.2. The B2-phase has the lowest enthalpy of formation, followed by the Ni<sub>5</sub>Al<sub>3</sub> structure.

From the averaged distance of the predicted structures from the final ground state line the preference of the system to crystalize in a bcc lattice can be estimated. In the extremal parts of the concentration range (near the pure elements) the predicted structures show formation enthalpies, which are more distant from the ground state line. At intermediate concentrations the enthalpies of formation reach lower values, which show comparable stability (lie directly above the ground state line). This behaviour results in more DFT derived structures for this segment of the phase diagram, since these structures often occurred to be the predicted as real ground state structures during the CE-fit. The comparison of the ground states for the experimentally established structures and the CE for the bcc-lattice (see figure 4.5) enforces the interpretation of the energetical behaviour on concentrations distant from the 50:50 B2-NiAl structure. Towards pure Al the formation enthalpies have the largest differences to the (metastable) bcc-type phases, because the Al-rich compounds crystallize in a quite different crystal structure (i.e. orthorhombic and trigonal structures). Out of the in total 329 possible clusters in the CE 39 were chosen at the end for deriving the ECIs. These ECIs were then used for the Monte Carlo simulation as discussed in the following section.

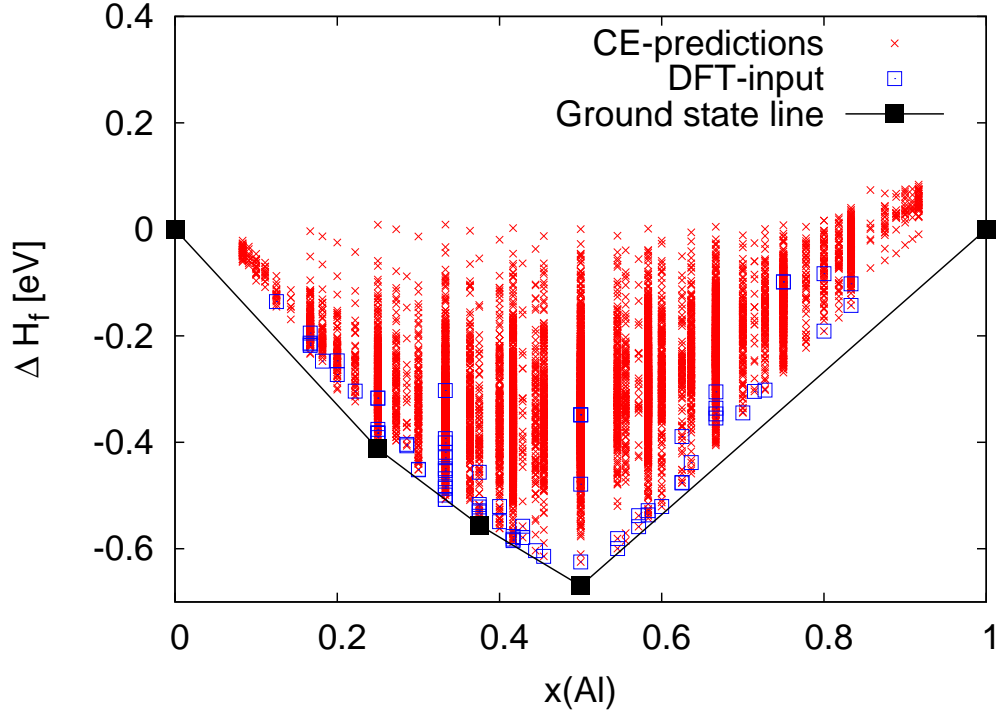


Figure 4.4: Final ground state line of the Ni-Al system: enthalpy of formation versus Al concentration. and ground state structures. Black circles represent the structures, which are the most favourable within a bcc-type lattice. As a reference for the formation enthalpy the DFT-calculated energy of fcc Ni and fcc Al were used. Other CE predicted structures shown as red circles. 10850 CE-predicted structures are shown in this figure. The blue squares represent the DFT input structures as used for the CE-fit.

	$E_{0,DFT}/\text{atom}$ [eV]	$\Delta E_0$ [meV]	$E_{0,CE}/\text{atom}$ [eV]	$\Delta H_f, DFT$ [eV]	$\Delta H_f, CE$ [eV]
Al-fcc	-3.725	0.0	-3.7250	0.0	0.0
B2-NiAl	-5.425	-1.026	-5.424	-0.671	-0.670
Ni <sub>5</sub> Al <sub>3</sub>	-5.564	2.755	-5.567	-0.535	-0.538
Ni <sub>3</sub> Al	-5.683	-1.962	-5.681	-0.414	-0.412
Ni-fcc	-5.783	0.0	-5.783	0.0	0.0

Table 4.2: Ni-Al system: the ground state enthalpies of formation as derived by DFT and CE.

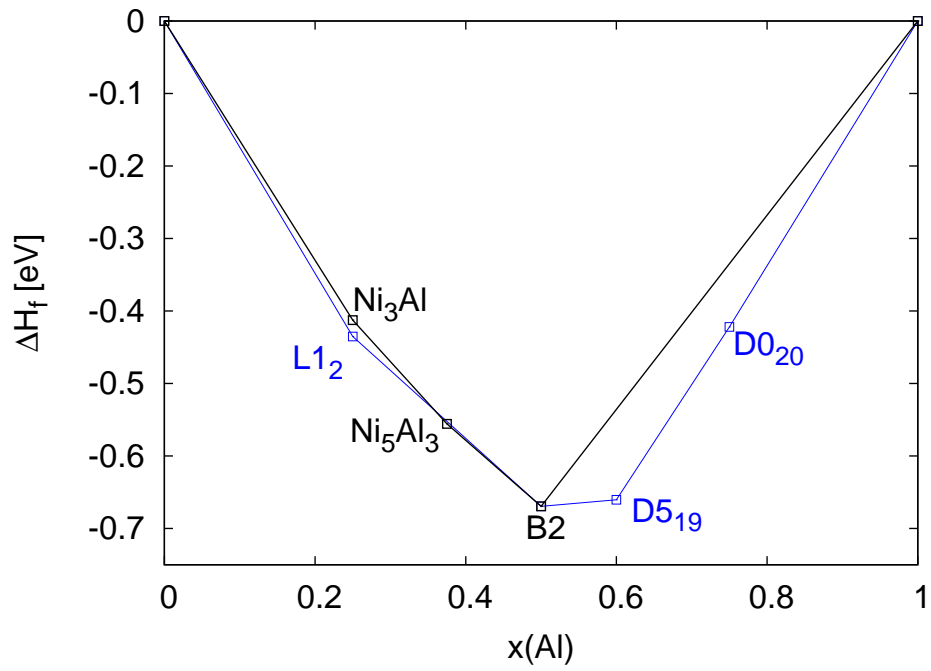


Figure 4.5: Ground state lines derived by CE for the bcc lattice and by DFT for the experimentally found structures (both at  $T=0\text{K}$ ). The DFT calculation for  $\text{Ga}_3\text{Pt}_5\text{-Ni}_5\text{Al}_3$  yields a formation enthalpy  $\Delta H_f$ , which lies above the ground state line and therefore was not included in the figure.

### 4.1.3 Monte Carlo simulations

#### Computational aspects

A grandcanonical ensemble was chosen for the Monte Carlo (MC) simulation of the Ni-Al system. Periodic boxes containing 40x40x40 atoms were used. A reasonable range for the chemical potential difference  $\Delta\mu = \mu_{Ni} - \mu_{Al}$  from 0.3 eV to 3.85 eV was chosen, which was studied in steps of 0.05 eV. In practice this was done by setting the chemical potential of Ni to 0 and varying the chemical potential of Al accordingly. The calculations were always done isothermic over the whole concentration range. At the beginning, every third grid point of the  $\Delta\mu$  range was studied (e.g. 0.3, 0.45, 0.6, and so on) running two cycles with 50,000,000 MC steps each to compute the starting simulation boxes for the final simulation run. In the next step the full  $\Delta\mu$  range was split into sets containing 3 consecutive  $\Delta\mu$  (e.g. 0.3 0.35 0.4 in one set) values each. By reading in the already prepared boxes the final simulation has been started by computing the first  $\Delta\mu$  contained in the set (which was also chosen to prerelax the box, 0.3 in the example). Two cycles with 50,000,000 steps each were used to converge the simulation. The resulting simulation box was now taken as the input for the second  $\Delta\mu$  step ( $\Delta\mu = 0.35$  in the example) in the set, which was simulated with the same number of steps. The routine was repeated for the missing third step ( $\Delta\mu = 0.4$  in the example).

After the MC runs were finished the convergence of the MC simulation at each step was checked. Figure 4.6 presents the convergence of such a set of MC runs. If the system did not converge after the two shown cycles the simulation was repeated reading the simulation box of the not converged run as a starting point.

The calculations were done in parallel for all investigated temperatures.

The interpretation of the formed phases in the simulated box was done by attributing locally ordered atomic arrangements to crystal structures. This was done by arbitrarily defining the range of local ordering in terms of small boxes consisting of 3x3x3 atoms. For the ordered phases the identification was first done by eye and the atomic distributions over the full concentration range were scanned for periodically repeating clusters. After an ordered structure was recognized the structural data of the corresponding periodical structures was implemented in the search routine. The search consisted of a scanning of the whole box for the 3x3x3 clusters consistent with periodical boundary conditions. The minimal size for the definition of a elemental exclusion was defined at 10 atom.

#### Results and Discussion

The three ground states found in the Ni-Al system are stable also at  $T > 0$ . Being the most stable structure in the system the B2-phase dominates the phase diagram. It is stable over a range of  $\Delta\mu = 2.5$  eV. In terms of the concentration this means that the

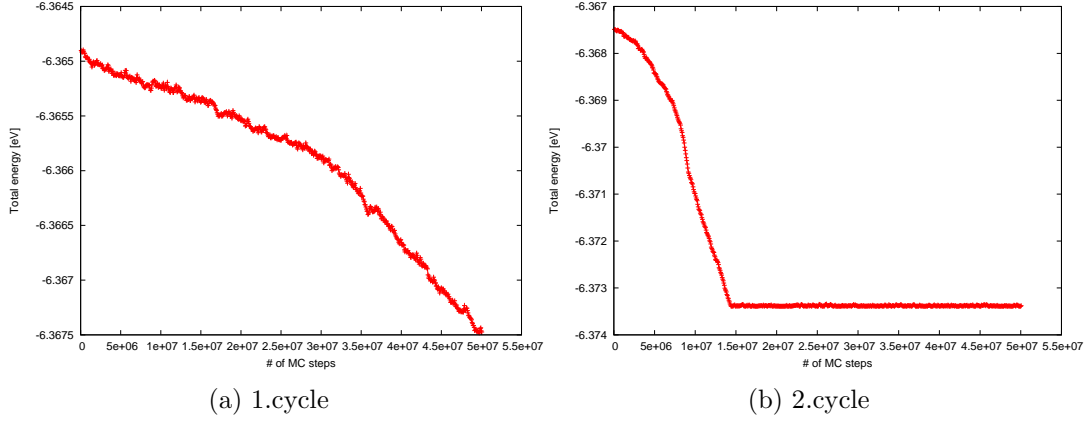


Figure 4.6: Convergency test for Ni-Al at a temperature of 1000K and for  $\Delta\mu = 1.9$ . The left figure (a) shows the first cycle of the simulation. There, the box as prepared in a previous simulation was taken as input and relaxed in  $5 \cdot 10^7$  steps. The resulting atomic distribution was taken as an input for the final simulation (b) which finally reached the convergency criterion.

ordered phase is stable in the range of 40% to 51 % Al. In the experimental phase diagram shown (figure 4.1) the B2 phase extends from  $\approx 42\%$  Al to  $\approx 55\%$  Al at 400 °C and this range even widens, namely to 32 % - 56 % Al at 1400 °C.  $\text{Ni}_3\text{Al}$  crystallizes in the fcc-type  $\text{L}_{12}$  structure, which is not included in the present CE, since it just deals with bcc-type structures. Nevertheless, at the 3:1 composition even the bcc-type phase diagram (see figure 4.4) indicates a possible phase stabilization. In both the experimental and the CE-MC derived phase diagram a phase forms at concentrations of 25 % - 27 % Al. According to the present calculations, at lower temperatures, which are not shown in the experimental diagram, the concentration range of  $\text{Ni}_3\text{Al}$ -like phase even widens.

The CE-MC derived  $\text{Ni}_5\text{Al}_3$  phase forms at temperatures larger than 500K. Since such low temperatures are not treated in the experimental phase diagram [51] the calculation can not be compared to experiment. Raising the temperature in the simulation the  $\text{Ni}_5\text{Al}_3$  phase is formed by the eutectic reaction  $\text{Ni}_3\text{Al} + \text{B2-NiAl} \implies \text{Ni}_5\text{Al}_3$ . A small mixed phase area was found between  $\text{Ni}_5\text{Al}_3$  and the surrounding phases. There is good agreement to the experimental phase diagram, in which  $\text{Ni}_5\text{Al}_3$  is formed in a range of 32 % to 36 %, whereas the CE-MC derived stability range is 29 % to 33 % Al. The small range of phase mixtures containing the  $\text{Ni}_3\text{Al}$  and the NiAl phase and the range of formation of  $\text{Ni}_5\text{Al}_3$  could be a consequence of the property of both phases to form in the same (bcc) lattice by Monte Carlo simulation. Changing between these two structures is done by just replacing Ni in the crystal with Al. Similar ordered cells have been taken as the input crystal. The two phases are shown in figure 4.7 a) and b).

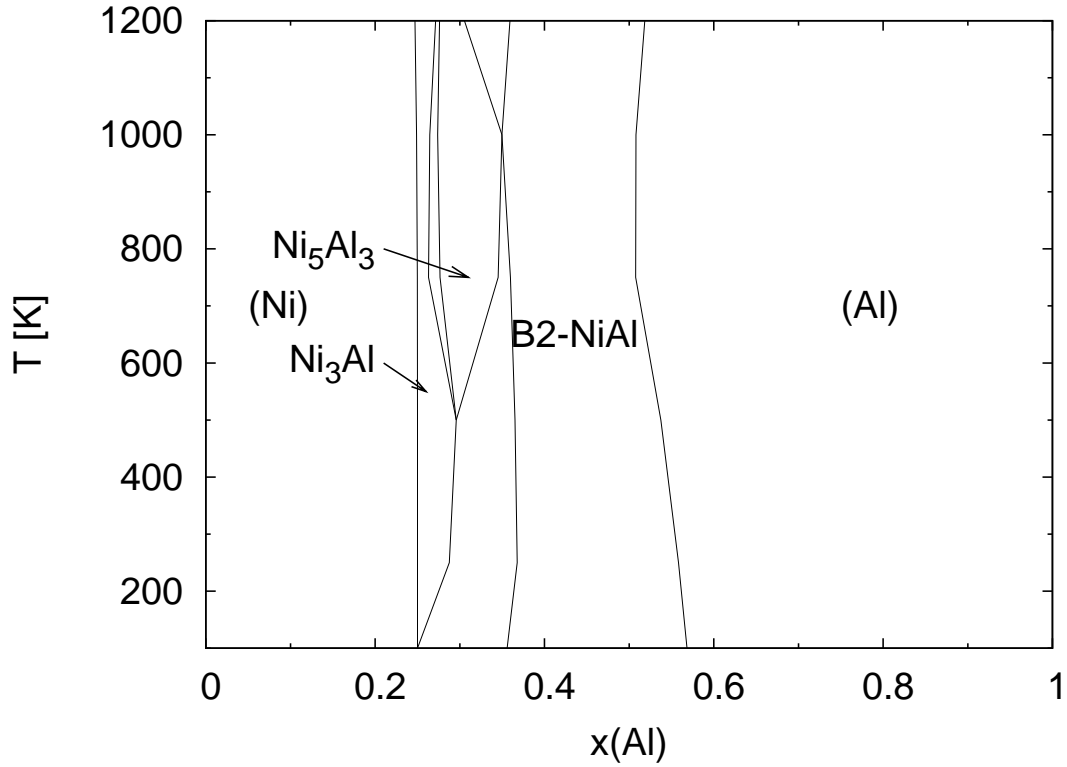


Figure 4.8: Phase diagram of NiAl-system as a result of a grandcanonical Monte Carlo simulation.

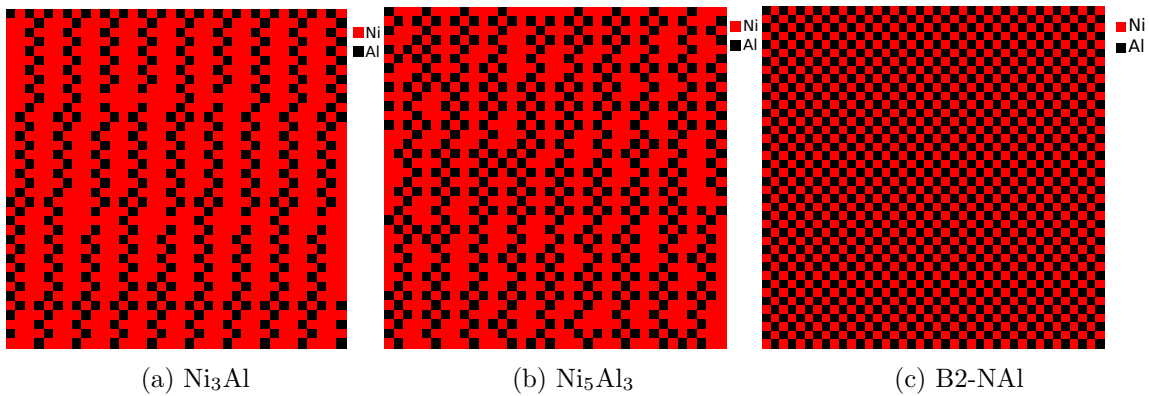
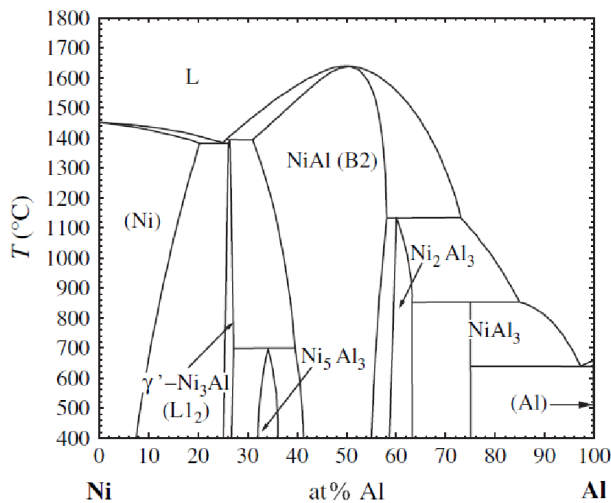
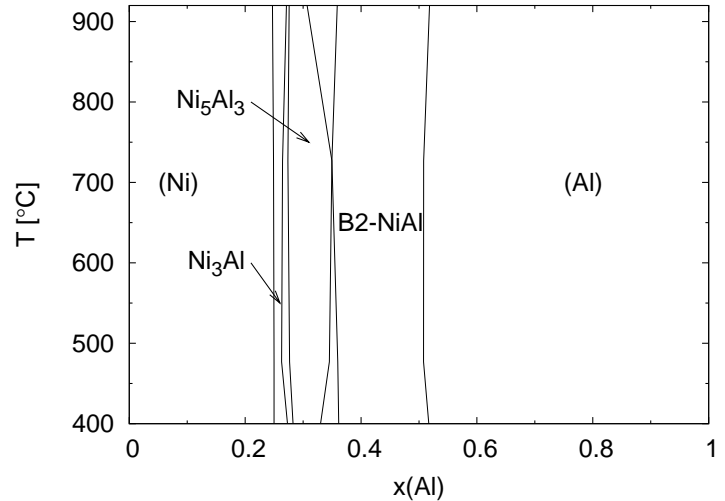


Figure 4.7: Atomic distribution in planes of the  $40 \times 40 \times 40$  atoms simulation box of a Monte Carlo simulation, in which the ordered phases as described in section 4.1.3 are recognized. Red squares: Ni, black squares: Al.



(a) Experimental phase diagram [51]



(b) CE calculated phase diagram

Figure 4.9: Comparison of the experimental phase diagram by Singleton et al. and the Cluster Expansion + Monte Carlo simulation calculated phase diagram in this work. It is important to mention that the investigation in the present work has only been done in the bcc lattice.

#### 4.1.4 Summary

The Ni-Al system consists of ground states which form in different lattice types, and one should keep in mind that the CE+MC calculations were done for bcc-type structures. Since the only ground state structure ordering in a bcc structure is the B2-NiAl phase, it was the only one of the experimental ground states predicted by the present study. Other ground states like the  $L1_2$ -Ni<sub>3</sub>Al phase could not be described since it is fcc-based, but another phase with the same stoichiometry has been found instead. This indicates a strong ordering tendency even if the structure is not the one for the actual ground state. As a consequence, the enthalpy of formation of the bcc-type variant is not so stable as for the  $L1_2$ -structure. Experimentally, Ni<sub>5</sub>Al<sub>3</sub> is also a stable ground state and it crystallizes in the Ga<sub>3</sub>Pt<sub>5</sub> structure. Nevertheless, the bcc-type CE+MC again finds a ground state phase for this composition. For the experimentally stable phases of D0<sub>20</sub>-NiAl<sub>3</sub> and D5<sub>19</sub>-Ni<sub>2</sub>Al<sub>3</sub> no CE+MC bcc-related phase could be found at higher temperatures. Summarizing, the CE-MC derived phase stabilities at finite temperatures behave similarly to the experimental ones as shown in figure 4.1, which indicates the quality of the present approach for extending DFT precision to system with a large number of atoms at elevated temperatures.

## 4.2 Iron-Aluminum

### 4.2.1 Experimental findings

Iron-Aluminium compounds became materials of great interest in the last decades. Their corrosion and oxidation stability at high temperatures in combination with their relatively light weight are promising properties for e.g. resistant coatings [56, 57] preferable to steel. Furthermore, Al-Fe materials are easily available and their cost is comparably low. As it is usual for intermetallic compounds also Fe-Al alloys (consisting of FeAl and Fe<sub>3</sub>Al) is brittle and breaks even at lower temperatures. Its low thermal ductility at room temperature in combination with its low flow stress at temperatures above 500°C are problematic shortcomings. A lot of effort went into improving their properties by adding ternary (or more) elements for hardening [58, 59], by introducing second phase precipitates [60] or by adding grains of borides, oxides and Laves phase intermetallics [61–63]. Nevertheless, its corrosive/oxidation resistance was intensively studied at higher temperatures, for which the Fe-Al alloys are of interest.

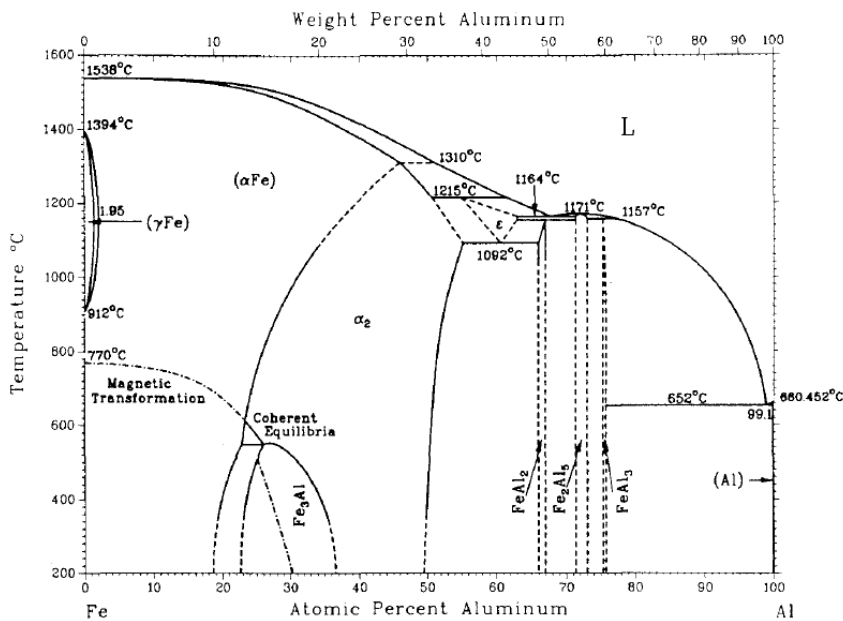


Figure 4.10: Al-Fe phase diagram [64]

Figure 4.10 shows the phase diagram of the Al-Fe system [64]. Note, that a number of stable phases can be found.

- $\alpha$  and  $\delta$  (bcc)- Fe and  $\gamma$  (fcc)- Fe
- D0<sub>3</sub>-Fe<sub>3</sub>Al
- triclinic - FeAl<sub>2</sub> [65]



- orthorombic -  $\text{Fe}_2\text{Al}_5$
- $\text{FeAl}_3$  (complex structure, see refence [66])
- fcc- Al

### 4.2.2 Search for the ground states

Similar to the Ni-Al system the cluster expansion for Al-Fe has been started by calculating the simple bcc structures B2-AlFe,  $\text{D0}_3\text{-Al}_3\text{Fe}$ ,  $\text{D0}_3\text{-AlFe}_3$  and B32-AlFe with all their possible modifications. After a short starting period were the best starting input set was identified. 10 structures with 8 atoms per unit cell were chosen as a starting set. The first fit led to a cross validation score of 26.25 meV and CE predicted 7 new structures , which were found to lie below the ground state line. This new structures were re-calculated by DFT and added to the original input. As for the Ni-Al system the size of the unit cell of the predicted structures was first set to 8 atoms and increased later on to 12 atoms until no new ground state structures were found.

Figure 4.11 shows the evolution of the cross validation score and the number of input structures during the complete energy fit. As already mentioned, at the beginning the fit was not good because the best starting input had to be found first. After CE reached convergency the input set consisted of 94 structures and the cross validation score had a value of 1.82 meV. 44 subsequently runs were needed to converge.

The final ground state line relative to bcc-Fe and fcc-Al is shown in figure 4.13. The ground state structures found in this system for the bcc parent lattice are  $\text{AlFe}_{11}$ ,  $\text{AlFe}_5$ ,  $\text{AlFe}_4$ ,  $\text{AlFe}_3$ , AlFe, and  $\text{Al}_2\text{Fe}$ . Their enthalpies of formation are presented in table 4.3. The dominating structure in the Al-Fe system is the  $\text{Al}_2\text{Fe}$  phase with an enthalpy of formation of  $\Delta H_f = -0.368$  eV. The overall enthalpies of formation are less stable than in the Ni-Al system. The trend to crystalize in the bcc-lattice can be realized from figure 4.13. Since pure Al crystalizes in an fcc structure CE derived phases with an excess of Al show a higher mean distance from the ground state line, resulting in even positive formation enthalpies (decomposition) for very Al-rich cases. Somewhat exceptional is  $\text{Al}_2\text{Fe}$  which dominates the phase diagram. At the Fe-rich region the predicted structures lie near the ground state line and no unstable bcc phases are derived.

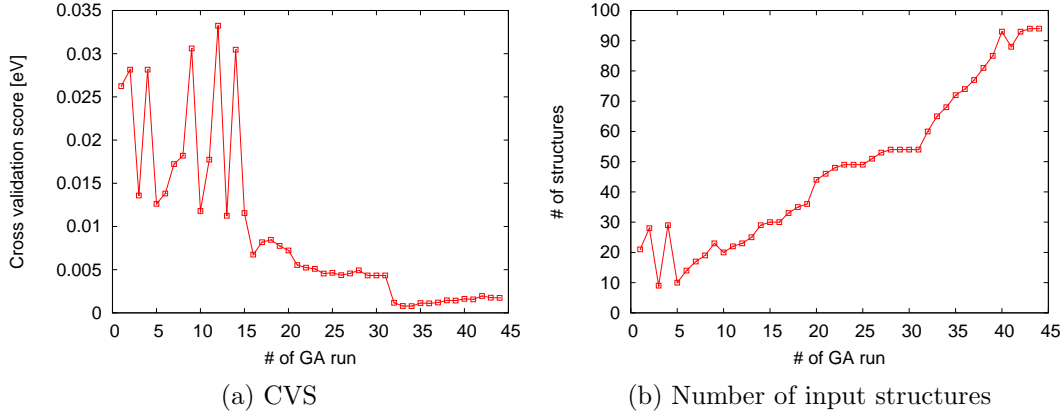


Figure 4.11: Evolution of the CE fit for Al-Fe: (a) decrease of the CVS with the number of GA runs; (b) increase of the number of input structures.

	$E_{0,DFT}/\text{atom}$ [eV]	$\Delta E_0$ [meV]	$E_{0,CE}/\text{atom}$ [eV]	$\Delta H_{f,DFT}$ [eV]	$\Delta H_{f,CE}$ [eV]
bcc- Fe	-8.333	0.0	-8.333	0.0	0.0
AlFe <sub>11</sub>	-8.023	3.28	-8.026	-0.081	-0.084
AlFe <sub>5</sub>	-7.716	0.66	-7.717	-0.166	-0.166
AlFe <sub>4</sub>	-7.591	0.82	-7.591	-0.193	-0.197
AlFe <sub>3</sub>	-7.395	0.06	-7.395	-0.235	-0.235
AlFe	-6.361	-0.67	-6.360	-0.332	-0.331
Al <sub>2</sub> Fe	-5.629	-0.17	-5.629	-0.368	-0.368
fcc- Al	-3.725	0.0	-3.725	0.0	0.0

Table 4.3: Al-Fe system: Formation enthalpies of the ground state structures predicted by CE and calculated by DFT.

### 4.2.3 Monte Carlo simulations

#### Calculation details

As for Ni-Al the Al-Fe system was computed in 40x40x40 simulation box with periodical boundary conditions. Since the difference between the DFT-energies of the two elements is 4.61 eV, a range for the difference of the chemical potential  $\Delta\mu$  from 3.0 eV to 6.55 eV has been chosen, which covers the whole concentration range. The step of width chosen for  $\Delta\mu$  was taken as 0.05 eV. The MC calculations for the Al-Fe system converge faster than for Ni-Al. Computational details are given in section 4.1.3, with a difference in the MC steps for the convergence. For the Al-Fe system 2 cycles consisting of 30.000.000 steps have shown to be enough for convergence.

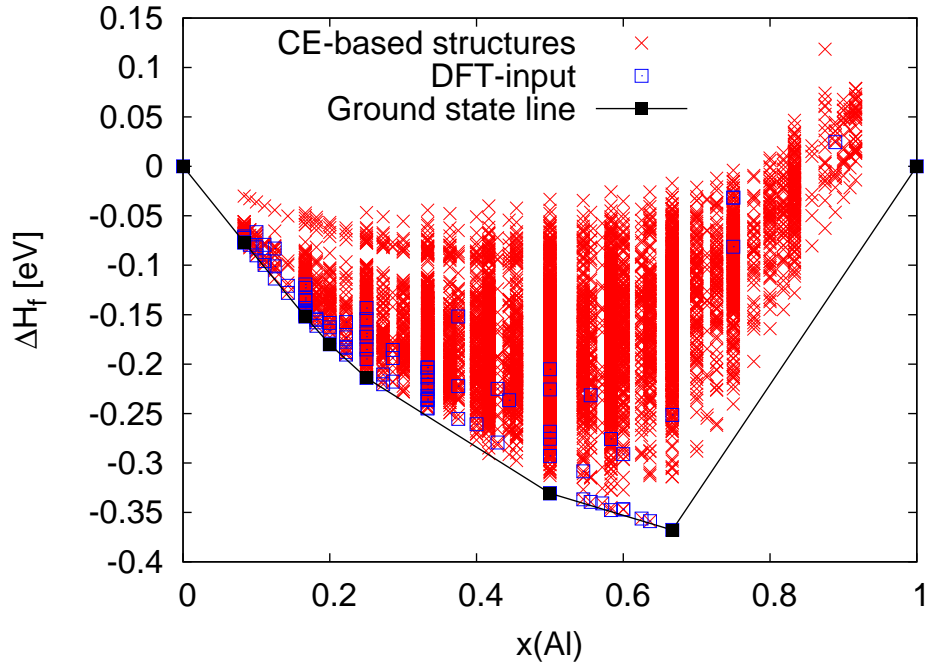


Figure 4.12: CE ground state line of the Al-Fe system for the bcc lattice. The red crosses represent the predicted structure energies by CE, the blue squares stand for the structures calculated by DFT after being predicted by CE. The enthalpies of formation are given relative to bcc-Fe and fcc-Al.

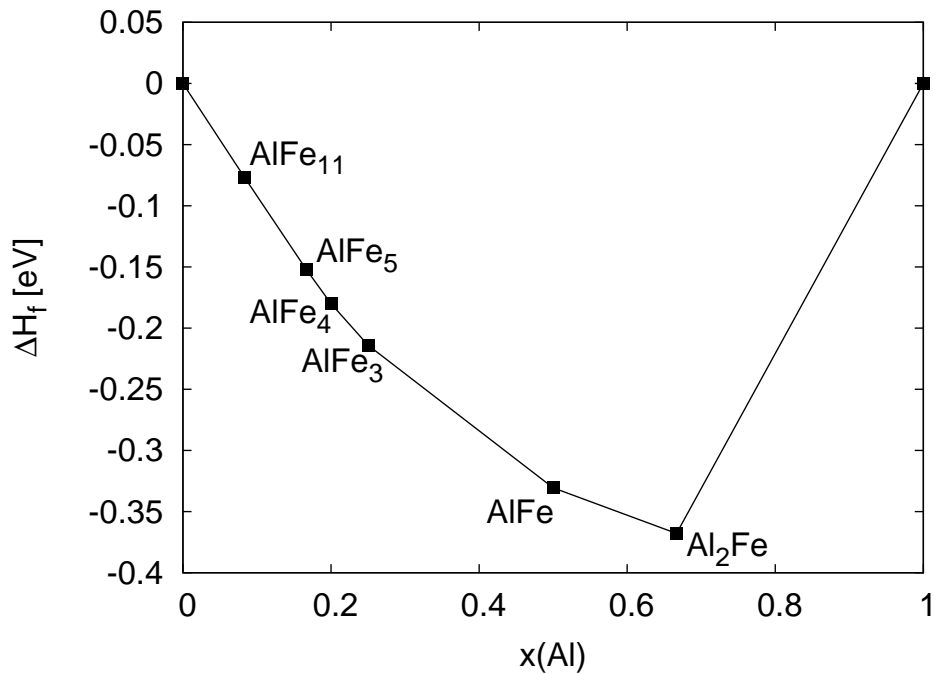


Figure 4.13: Ground state line of the Al-Fe system with the final ground state structures shown explicitly.

## Discussion

Figure 4.15 shows the ground state diagram including the ground state lines at the investigated temperatures. At all the temperatures the  $\text{Al}_2\text{Fe}$  structure is the most stable one with  $\Delta H_f = -0.352$  eV at  $T=0\text{K}$ . The other phases which have been found to be stable at  $T=0$  are mostly destabilized at higher temperatures. The B2-AlFe phase does not form as a pure phase. It was just found in combination with the  $\text{Al}_2\text{Fe}$  structure, but more of AlFe is stabilized at higher temperatures.

The ground state diagram predicts an  $\text{AlFe}_3$ -like stable phase (will be denoted as "c392") at  $\approx 25\%$  Al with its maximum stability at 500K indicating strong ordering: figure 4.14c shows a cut through the MC box revealing the well ordered structural nature of c392 because its typical local pattern fills most of the space. Comparing the experimental phase diagram with the MC simulations a few differences are observed. Only two bcc structures are described in experimental works:

- The B2-AlFe phase is documented in most of the experimental studies on Fe-Al, see e.g. Crimp and Vedula [67]. However, the experimental phase diagram shown the present work [64] does not contain this ground state. The result from the binary CE plus grandcanonical MC leads to the result shown in the phase diagram. The B2-phase occurs only as a mixed phase in combination with  $\text{Al}_2\text{Fe}$ . A test using canonical MC was done at 50:50 composition revealing, that the AlFe does actually form in this system but contains lot of antisite atoms (i.e. Fe sitting on Al-sublattice sites). Accordingly, the structure was drawn in the phase diagram symbolizing that it was found at the fixed B2-concentration (result of canonical MC) and as a mixed phase in combination with the  $\text{Al}_2\text{Fe}$  phase (result of the grandcanonical MC).
- The  $\text{D0}_3$ - $\text{AlFe}_3$  as phase documented in the experimental literature has not formed, and it also not been part of the ground state line at  $T=0\text{K}$ . DFT calculations yield a difference of 0.014 eV between the unstable  $\text{D0}_3$  phase and the most stable phase ("c392") whose structure was predicted by MC at the same concentration. It might be possible that temperature dependent phonon free energies resolve this problem, because experimentally the phase with the  $\text{D0}_3$  structure only appears at elevated temperatures.

The temperature dependant stability of the in this work found well ordered c392- $\text{AlFe}_3$  structure is particular. It is formed in a temperature range of 250K-750K and transforms into a solution of Al in Fe at higher temperatures.

The  $\text{Al}_2\text{Fe}$  phase turned out to be the most stable phase in the bcc alloy system and it has formed in accordance to the experiment even if the experimental found  $\text{Al}_2\text{Fe}$  structure crystallizes in a triclinic lattice. According to Corby and Black [65] its unit cell contains 6.5 Fe and 11.5 Al atoms and has the space group P1. The concentration range where the phase appears is broadened in comparison to the experimental value leading to a stability at concentrations of  $\approx 32\%$ - $38\%$  Al.

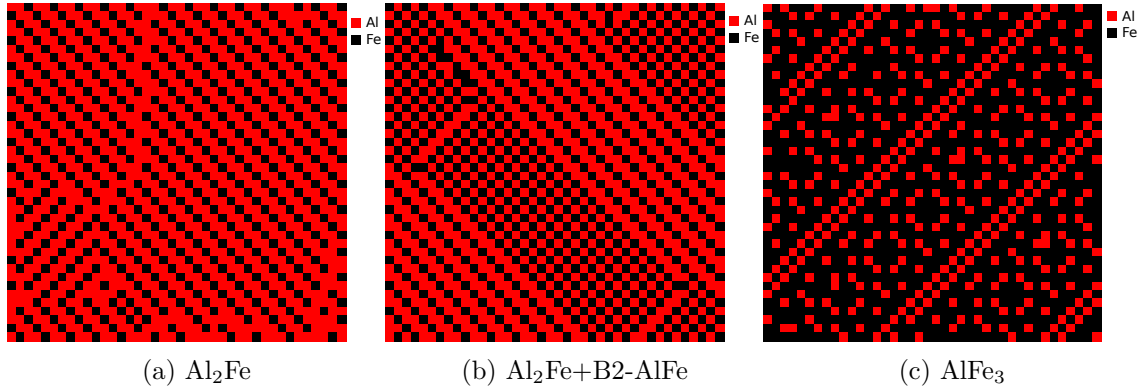


Figure 4.14: Cut through the MC boxes for the  $\text{Al}_x\text{Fe}_{1-x}$  system. The figure shows the found stable phases at finite temperatures. (a) and (c) have been taken from the MC simulation at 500K, since  $\text{AlFe}_3$  has its highest stability at this temperature.  $\text{Al}_2\text{Fe}$  is stable at every investigated temperature. (b) is taken from the simulation at 1200 K since the B2-phase is stabilized at higher temperatures.

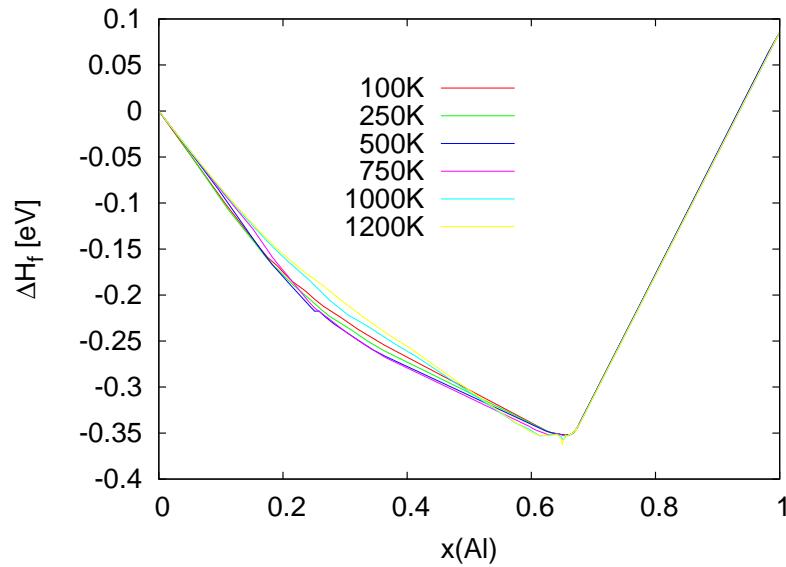


Figure 4.15: Fe-Al: enthalpy of formation at the investigated temperatures calculated by grandcanonical MC. Values are calculated relative to the ground states of bcc-Fe and fcc-Al. Since CE+MC was done for a bcc lattice the enthalpy of formation gets even positive near pure fcc Al. The value of 0.085 eV for pure Al is the difference between fcc and bcc Al.

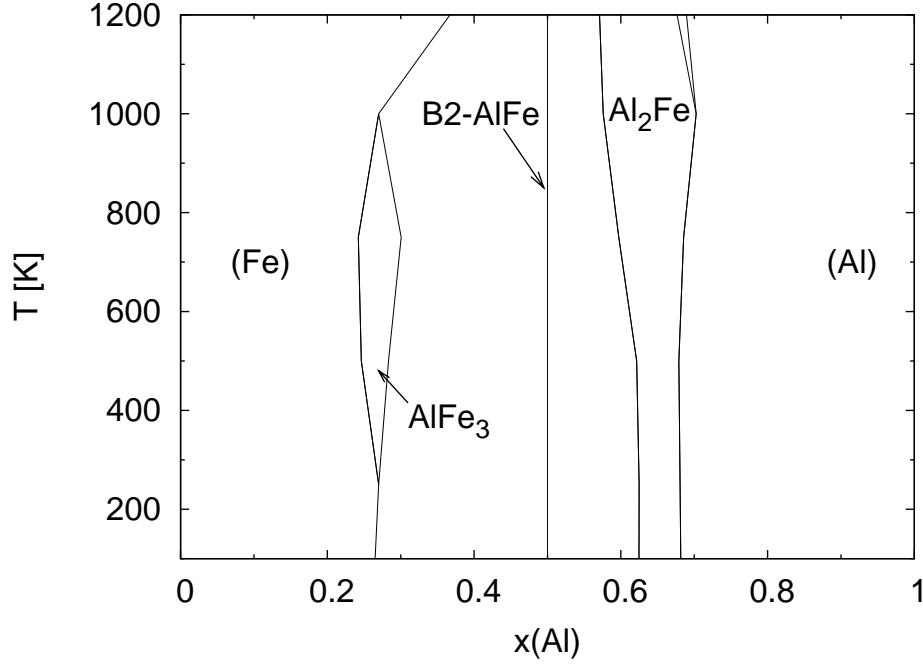


Figure 4.16: Cluster expansion and grandcanonical MC calculated phase diagram of the Al-Fe system for a bcc parent lattice. The most stable ordered phase is  $\text{Al}_2\text{Fe}$ . Experimentally, its structure was found to be triclinic.

#### 4.2.4 Summary

A variety of stable ground states are found in the binary Al-Fe alloy system by the CE for a bcc parent lattice. The stable structures reveal some complex ordering: cubic, orthorombic and triclinic structures were documented by experiment. The ground state line at  $T=0\text{K}$  consists of the following phases:  $\text{AlFe}_{11}$ ,  $\text{AlFe}_5$ ,  $\text{AlFe}_4$ ,  $\text{AlFe}_3$ ,  $\text{AlFe}$  and  $\text{Al}_2\text{Fe}$ . According to experiment from all these phases only  $\text{AlFe}$  has a bcc like structure, namely B2. The experimentally claimed high temperature phase  $\text{AlFe}_3$  of bcc-like  $\text{D}_{03}$  structure is not stable in the CE plus MC calculations. The most stable phase in the system is  $\text{Al}_2\text{Fe}$  with an enthalpy of formation of  $\Delta H_f = -0.352$  eV/atom, which in experiment is found to crystalize in a triclinic symmetry [65]. The experimentally more important phase is the B2-phase  $\text{AlFe}$ , which was studied extensively, see like e.g. [68–70]. According to the results of the present work it is the second most stable phase at  $T=0\text{K}$  with a value of  $\Delta H_f = -0.288$  eV/atom. From the Fe-rich phases only  $\text{AlFe}_3$  is a topic in literature. As already mentioned its ground state conformation is mostly described as an  $\text{D}_{03}$  structure. The ground state predicted in the present work is 0.014 eV lower in energy, but it should be noted that the  $\text{D}_{03}$  is experimentally stable only at elevated temperatures. The MC simulations at finite temperatures resulted the ground state diagram of figure 4.15 and the phase diagram of figure 4.16. As it is the case at  $T=0\text{K}$   $\text{Al}_2\text{Fe}$  dominates the

phase diagram at every investigated temperature. It shows a broadened concentration range in comparison to the phase diagram in figure 4.10, which even increases at higher temperatures. The B2-AlFe phase is not part of the ground state line as derived from grandcanonical MC. At Al concentrations of 60 to 66 % Al B2 AlFe only occurs in combination with Al<sub>2</sub>Fe structural fragments . Nevertheless a canonical MC results in a stable B2-phase formed with perfect stoichiometry. From the Fe rich structures formed at T=0 only AlFe<sub>3</sub> remained stable at finite temperatures.

## 4.3 Nickel-Iron

### 4.3.1 Experimental findings

Experimental investigations on the Ni-Fe binary alloys have shown that the system forms a solid solution with fcc structure over the whole concentration range at elevated temperatures. Only two ordered phases are reported, namely NiFe with the tetragonal L1<sub>0</sub> structure and Ni<sub>3</sub>Fe with the cubic fcc-like L1<sub>2</sub> structure. The Ni<sub>3</sub>Fe phase is indeed a stable phase with a melting point of 517 °C documented in the paper of L.J. Schwartzendruber et al. [71]. On the other hand, the stability of NiFe was not described in this experimental work. Nevertheless Peterson et al. identified the L1<sub>0</sub> structured NiFe phase in the iron meteorite “Cape York“ [72]. The meteorite was studied with X-ray and Mössbauer spectroscopy resulting in the finding that the ordered L1<sub>0</sub> structures has formed in the lamella of the meteorite under the circumstances in space (cooling rate of 1°C over 10<sup>6</sup> years).

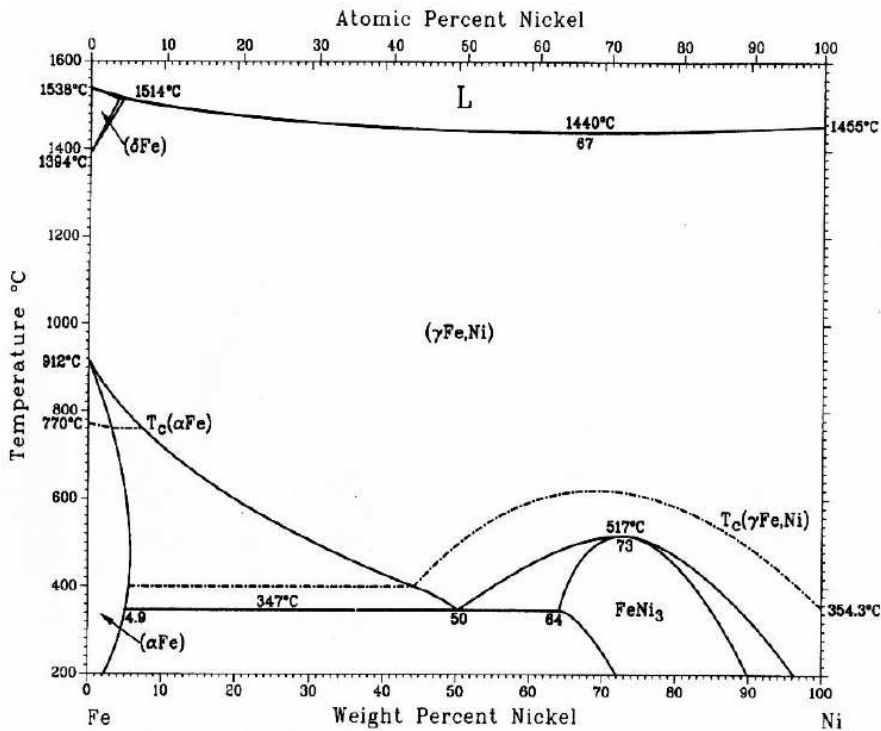


Figure 4.17: Experimental phase diagram of the Ni-Fe alloy system [71]. Most of the region of solid phases at elevated temperatures is covered by a solid solution of fcc-Ni and fcc- $\gamma$ -Fe. structure. At lower temperatures the ordered compound Ni<sub>3</sub>Fe with fcc-L1<sub>2</sub> is stable.

Figure 4.17 presents an experimental phase diagram [71] showing only one stable compound, namely Ni<sub>3</sub>Fe. However, according to the DFT calculations of the present



study NiFe is also a stable ground state. The reason why this structure is not found experimentally because at elevated temperatures it might be entropically destabilized in comparison to its neighbouring phases, which are a Ni-rich solid solution and Ni<sub>3</sub>Fe. For this it is important that Ni<sub>3</sub>Fe has the lowest  $\Delta H_f$  according to table 4.4.

	$E_{0,DFT}$ [eV]	$\Delta H_f$ [eV/atom]
bcc-Fe	-8.333	0.0
L1 <sub>0</sub> -NiFe	-7.127	-0.069
L1 <sub>2</sub> -Ni <sub>3</sub> Fe	-6.510	-0.090
fcc-Ni	-5.783	0.0

Table 4.4: DFT formation enthalpies of Ni-Fe for the experimental ground state structures. The reference phases are fcc-Ni and bcc-Fe.

### 4.3.2 Search for the ground states

To start the ground state search 28 DFT input structures varying from pure Fe to pure Ni were used. By applying the cluster expansion on these structures a cross validation score of 16.05 meV was achieved. Since there are almost no stable ordered structure in the whole concentration range the description of the ground state line is rather subtle. Therefore, in subsequent MC runs  $\Delta H_f$  was calculated relative to bcc-Ni and not for fcc-Ni (the stable phase of Ni). Of course, for the second elemental reference ground state bcc-Fe was taken. Then a stable ground state line could be derived because of one stable phase as shown in panel (b) of figure 4.19 with  $\Delta H_{f,bcc-Ni} = -0.0027$  eV. When now using fcc-Ni enthalpy of formation is lowered to a value of  $\Delta H_{f,fcc-Ni} = -0.0012$  eV as shown in panel (a) of figure 4.19.

The size of the unit cells of the predicted structures was limited to 8 atoms, which was sufficient for a converged CE. Similar to the other binary systems the cross validation score varied strongly variation at the beginning of the CE. After  $\approx 10$  runs the input set was quite stable and the CVS decreased finally to a value of 1.1 meV. At this point the CE was considered to be converged. In total, DFT calculations for 101 structures were made. The evolution of the CVS runs with the number of DFT input structures is sketched in figure 4.18.

	$E_{0,DFT}/\text{atom}$ [eV] $\Delta E_0$ [eV]	$E_{0,CE}$ [eV]	$\Delta H_{f,DFT}$ [eV]	$\Delta H_{f,CE}$ [eV]	
fcc-Ni	-5.7848	0	-5.784	0	0
bcc-Ni	-5.68	0	-5.68	0	0
NiFe <sub>3</sub>	-7.697	-0.0007	-7.697	-0.028	-0.027
bcc-Fe	-8.333	0	-8.333	0	0

Table 4.5: Ground state and formation enthalpies as derived by DFT and predicted by CE for Ni-Fe for bcc-like parent structures. It should be noted, that the bcc-Ni was taken as a reference and not the fcc ground state phase.

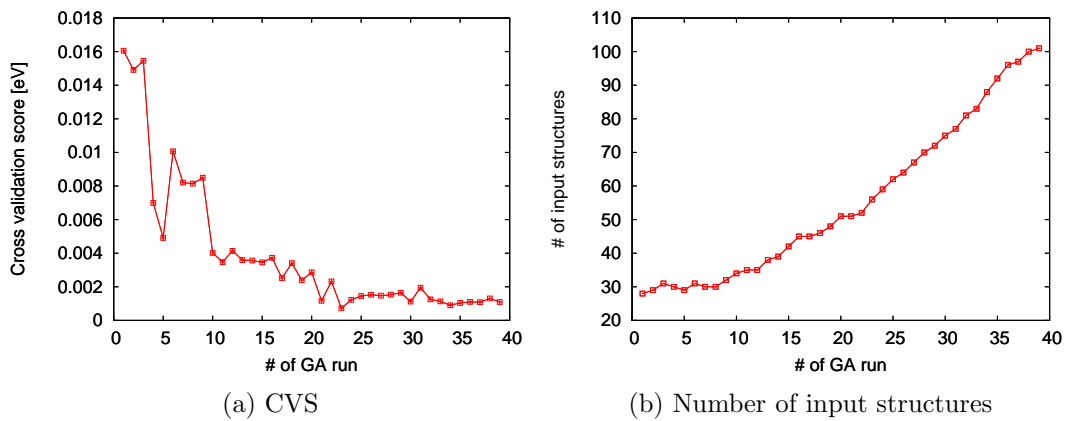


Figure 4.18: Evolution of the CE fit for Ni-Fe. (a) Decrease of CVS vs. number of GA runs; (b) increase of number of input structures vs. CE runs.

### 4.3.3 Monte Carlo simulation

#### Calculation details

As a consequence of the low  $\Delta H_f$  of the only ground state structure and the systems tendency to form a solid solution at elevated temperatures the range of chemical potential differences  $\Delta\mu$  needed for the grandcanonical Monte Carlo simulation was rather small. At 100K the  $\Delta\mu$  range which leads to a simulation box containing both the elements goes from 2.5 up 3.05 eV but it widens to a range of 2.0-4.5 eV at 1200K. Taking into account this range of  $\Delta\mu$  and knowing that the difference between the ground state energies of the elements is 2.652 eV the final range of  $\Delta\mu$  was chosen to reach from 2.0 eV to 5.0 eV with a step size of 0.025 eV for varying  $\Delta\mu$ . Because no ordered phase is found for the bcc-like parent lattice the grandcanonical MC converges very fast. Because of that a larger 50x50x50 simulation box could be taken. Then, two cycles with 10,000,000 MC steps for each of them were sufficient for converging the MC at every each temperature.

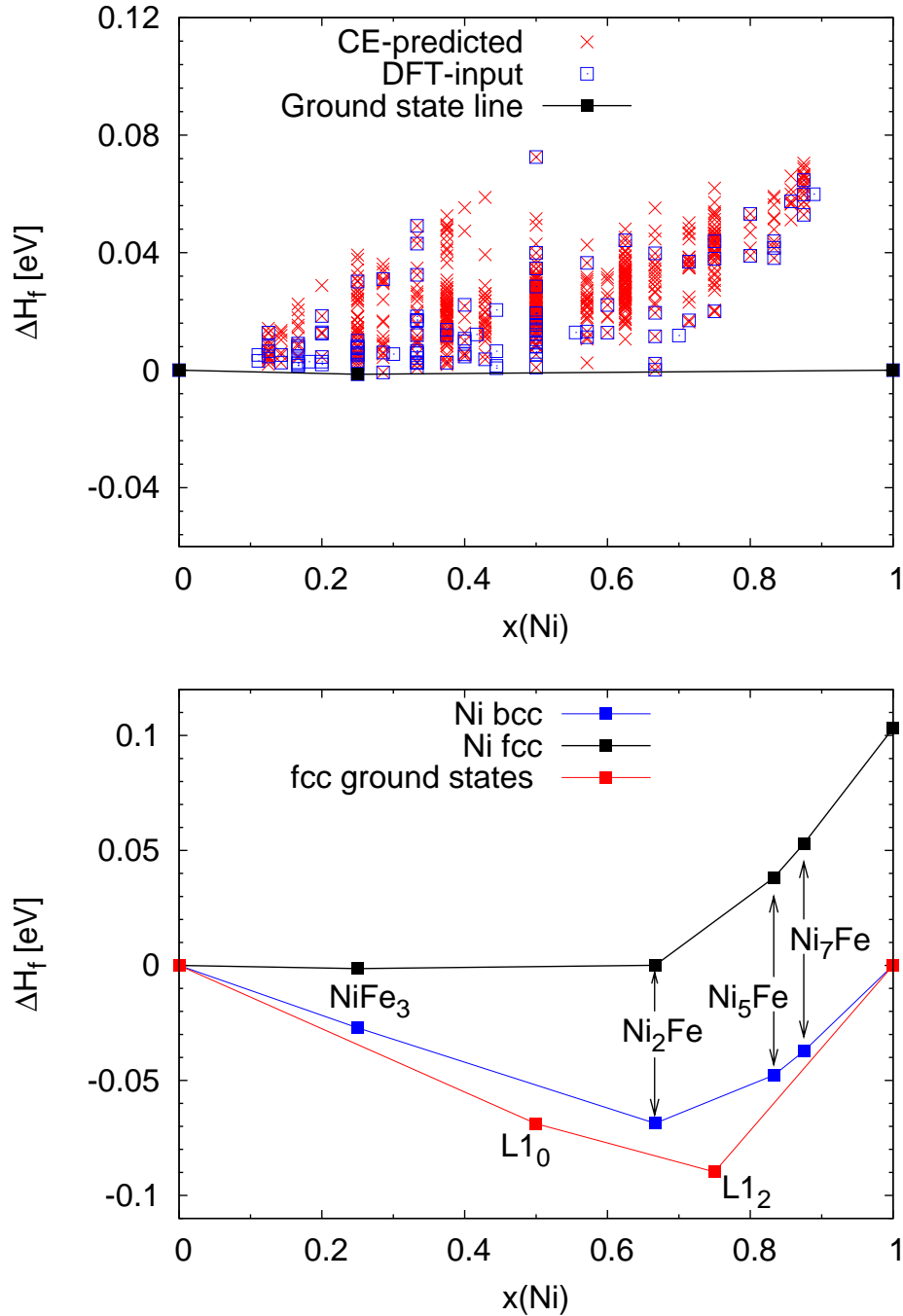


Figure 4.19: Calculated ground state line of Ni-Fe. The calculated ground state line relative to the fcc-Ni and bcc-Fe is shown in both panels. Upper panel (a): ground state diagram containing input DFT (blue squares) and CE-predicted (red crosses) results. Lower panel (b): Ground state line containing the phases described in the literature as calculated by DFT (formation enthalpies, see table 4.4) and predicted by CE for a bcc-like parent lattice. The black line shows the CE ground state relative to the fcc ground state of Ni; blue line refers to bcc-Ni as a reference; red line shows DFT results for the experimentally stable phases.

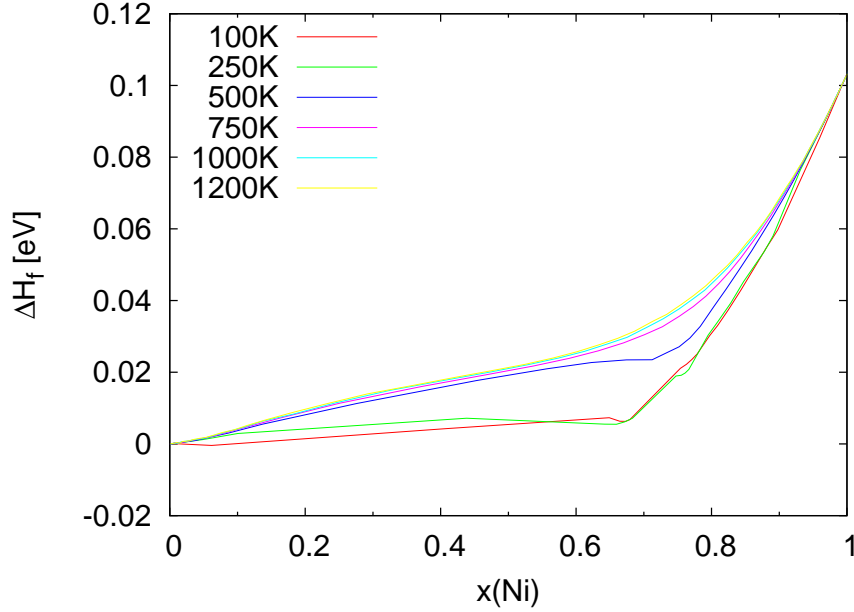


Figure 4.20: MC results of Ni-Fe for the bcc-like parent lattice: Enthalpy of formation at the investigated temperatures with fcc-Ni and bcc-Fe as reference phases. Even at elevated temperatures no stable phase was found. The rather large positive value on the Ni-rich side is due to the enthalpy difference between fcc- and bcc-Ni, which is 0.101 eV.

## Discussion

No stable phase was found in the bcc-lattice type system at finite temperatures according to the enthalpies of formation relative to fcc-Ni and bcc-Fe as shown in figure 4.20 over the whole concentration, since all  $\Delta H_f$  are positive. At temperatures under 500 K the  $\Delta H_f$ 's show similar behaviour as resulted from the CE at the temperature zero point. At and above 500 K the  $\Delta H_f$  reaches clearly positive values over the whole ground state diagram if calculated relative to fcc-Ni.

The raise of the  $\Delta H_f$  to values near to the zero point (fcc-Ni,bcc-Fe) can be interpreted as the tendency to form a random alloy instead of ordering in a defined crystal structure. As a consequence, for temperatures as low as 500 Kelvin the system behaves as a solid solution over the whole composition range. For the MC results at 100 and 250 K the formation enthalpies are close to zero at the Fe-rich end. Checking the atomic distribution in the MC boxes a trend to form stable structures is visualized. Since these ordered phases only occur at such low temperatures no comparison to experimental values is possible. No phase diagram was made because practically no ordered phase was found in the calculations.

#### 4.3.4 Summary

Experimentally, the Ni-Fe alloy system consists of solid solutions with fcc structure at higher temperatures. Doing the CE and MC for a bcc-type parent lattice (and also taking bcc-Ni as a reference) yields one stable ground state phase with a very small negative enthalpy of formation at  $T=0\text{K}$ , which is of the order of the fitting error of the CE. Furthermore, Monte Carlo simulations at finite temperatures reveal a tendency for ordering at temperatures above 250 Kelvin the system is a solid solution of the two elements over the whole concentration range.

For a more realistic simulation of the Ni-Fe system a CE for an fcc-type parent lattice would be necessary. However, this work is mainly interested in the formation of NiAl precipitations and phases at the Fe-rich side up to temperatures at which bcc-Fe, the ground state  $\alpha$  phase, is stable. When including also fcc-phases for the ternary case the complete set of studies –as presented here for the bcc parent lattice– must be done for the fcc lattice, and finally the two CE have to be merged: a scope which is certainly well beyond the time horizon given by a diploma thesis. Such a task, however, will be a promising adventure for a doctoral thesis.



## 5.1 Introduction

Deriving temperature dependent phase stabilities for the ternary alloy system Fe-Ni-Al is the ultimate goal of the present work. To do it with DFT precision –by means of the CE and MC– is a particularly challenging task. Nevertheless, thanks to the very recent developments of computational methods and computer hardware such a task is feasible in a diploma thesis since a suitable expertise is available.

As already mentioned in section 4.1 the compounds NiAl and Ni<sub>3</sub>Al exhibit high strength at high temperatures with a good oxidation resistance and low density but –as usual with intermetallic compounds– they are brittle at lower temperatures. To improve this failure third components are mixed to the binary Ni-Al alloys. Liu and Pope [73] deduced that small additions of boron result in an increase of the ductility of the alloys. Also adding small amounts of Fe to the binary system improved the ductility according by Darolia and Lahrmann [46], who investigated small crystal slabs of B2-NiAl with a substitution of up to 2 at. % of Al by Fe. A substantial improvement of the room temperature ductility occurred when adding 0.1-0.25 % Fe, but increasing the Fe content did not lead to further improvements. Letzig et al. [74] have even observed, that adding Fe to B2-NiAl at Ni-rich regions leads to a weakening by forming solid solutions of NiFe in the B2 phase. Also magnetic properties of the ternary system are of interest. Marcon et al. [75] studied the magnetic properties in the ternary system already in 1978. In their work the Fe<sub>2</sub>NiAl compound was suggested to be an interesting permanent magnet. The experimental investigations were mostly limited to selected concentration ranges and they show some differences in their results. The miscibility gap between  $\gamma$ -Fe and B2-NiAl is an example of such an inconsistent description.

From a theoretical point of view, the Fe-Ni-Al system is also of some interest. Pure Ni and Fe are two transition metals with localised valence d-states being ferromagnetic in their ground state, whereas Al is a simple metal and its electronic nature is rather free-electron like. Concerning binary compounds, Fe and Ni form ordered compounds with Al such as FeAl and NiAl, which is particularly stable. The crystal structure of both compounds is the bcc-type B2 structure, although pure Ni and Al prefer the fcc

structure. Only Fe (below the martensitic transformation temperature) crystallizes in a bcc structure. The 1:1 compounds NiAl as well as FeAl crystallize in the bcc-type B2-structure, and they are very stable. On the other hand Ni-Fe alloys tend to form a solid solution over most of the mixing range.

In the present work, we are mainly interested in the formation of Ni-Al phases within the Fe-rich Fe-Ni-Al alloy system. Therefore, a CE and subsequent MC simulations were done for concentration ranges defined by  $|x(\text{Ni}) - x(\text{Al})| < 0.3$  and  $0 < x(\text{Fe}) < 1$ .

## 5.2 Fe-Ni-Al phase diagram

A variety of experimental and theoretical studies were made on the phase stabilities of the Fe-Ni-Al-system.

Figure 5.2 shows a collection of phase diagrams as collected and reviewed combined by Eleno et al. [45] at different temperatures. Clearly, the phase diagrams are dominated by the B2-NiAl, the B2-AlFe, and the  $\alpha$ -Fe phases, which all form in bcc-type lattices. But also stable fcc phases such as the  $L1_2$ -Ni<sub>3</sub>Al and the Al<sub>3</sub>Ni<sub>2</sub> compounds are formed. The extension of the B2-NiAl phase reaches up to 90% of iron forming a mixed phase with the elemental A2-Fe phase at 750°C. Raising the temperature leads to decrease of the mixed phase extension. A small mixed phase between the B2 ordered composition and elemental iron is still formed at 950°C, but most of the area relevant for the present work is dominated by B2 ordering. The solid solution containing fcc Fe and Ni has been found in a relatively stable concentration range up to 10 % Al over all the shown temperatures. The mixed phase containing the mentioned solid solution and the B2 phase enlarges to both higher Ni and higher Fe concentrations (at constant Al concentration) rising the temperature. The description of the Al-rich side in the experimental Gibbs triangles is not described accurately. Since this part of the phase diagram is not contained in this work investigated concentration range, this fact can be neglected.

A theoretical study was done by Lechermann within his PhD thesis [23], where he modelled the phases by the so-called cluster variation method (CVM) for the fcc as well as the bcc parent lattice. CVM is a predecessor of CE, the main difference being that CE is based on DFT energies for *relaxed* structures. A Gibbs triangle as derived in this work is shown in figure 5.1. As described for the experiment the B2 phase (consisting of NiAl and AlFe) is the dominating stable ordered phase. It is formed up to Fe concentrations of about 80%. The other stable binary phases found are the  $L1_2$ -Ni<sub>3</sub>Al and the  $L1_2$ -AlFe<sub>3</sub>, which form in rather small concentration regions only. The phases formed by the elemental ground states are stable up to the regions of mixed phases.

In the thesis of Lechermann phase diagrams for the bcc-parent lattice only are shown



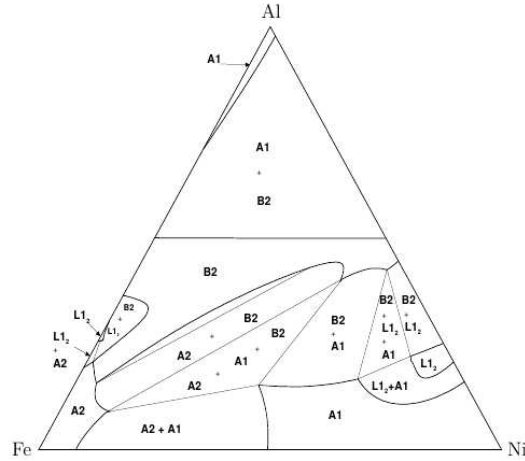


Figure 5.1: Gibbs triangle at 1250K of Fe-Ni-Al as calculated by the Cluster Variation Method of Lechermann [23]. Shown are phases formed within fcc and bcc parent lattices.

in figure 5.3. There, the  $D0_3$  phases  $Fe_3Al$  and  $Ni_3Al$  are stable over an extended region of the Gibbs triangle. However the thermal stability of  $AlFe_3$  is not very expressed because it is only stable to 500K. In contrast to that  $D0_3$ - $Ni_3Al$  does not extend over such a wide region, but is stable to high temperatures up to 1500K. Summarising, the stable bcc-structure that are found experimentally and theoretically are the  $B2$ -( $NiAl, AlFe$ ),  $D0_3$ -( $AlFe_3, Ni_3Al$ ) and the  $A2$ (fcc)-Fe phases.

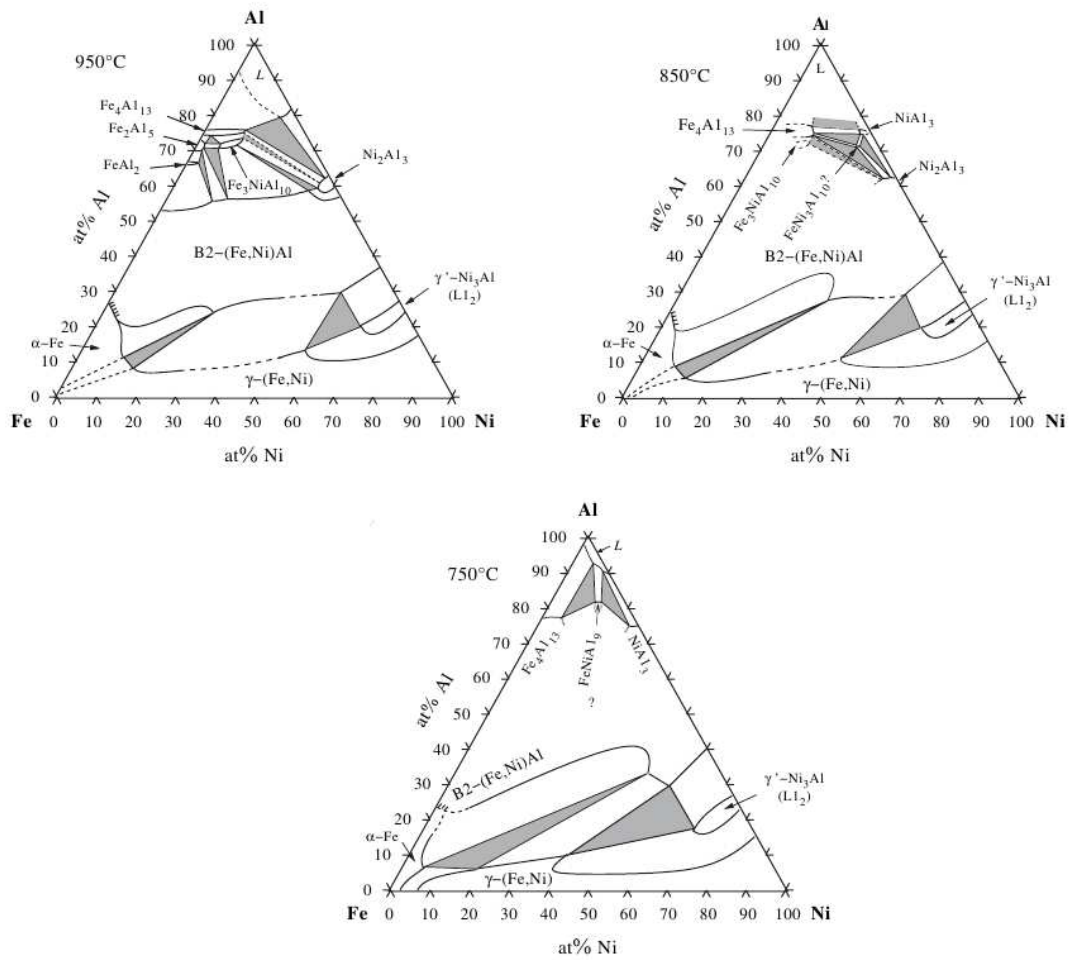


Figure 5.2: Fe-Ni-Al phase diagrams derived from experimental data as assessed by Eleno et al. [45] at several temperatures.

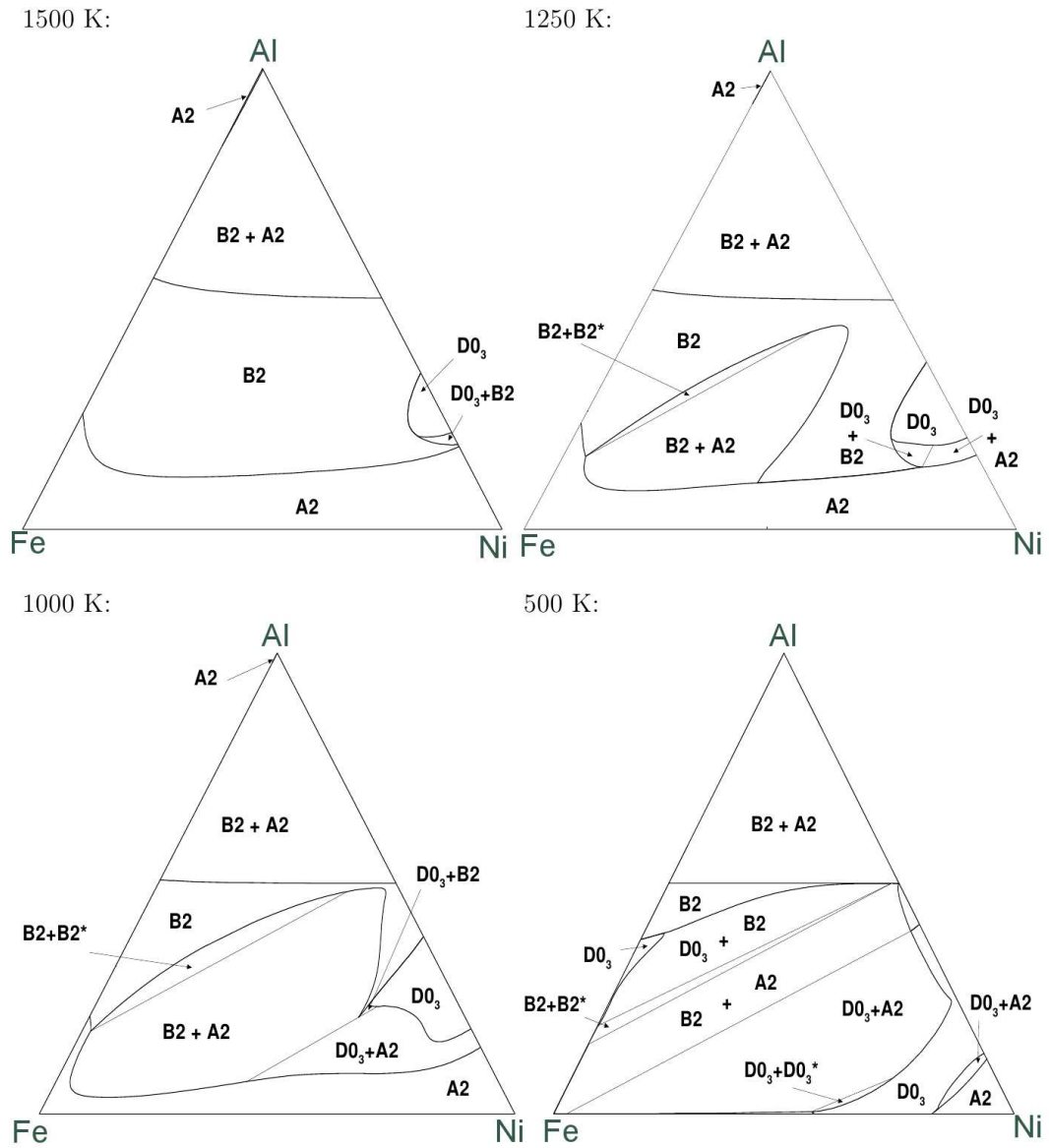


Figure 5.3: Fe-Ni-Al phase diagram for the bcc-type phases as calculated by Lechermann [23] with the Cluster Variation Method. The designation of the elements on the corners of the Gibbs triangles has been added by the author.

## 5.3 Ground state search

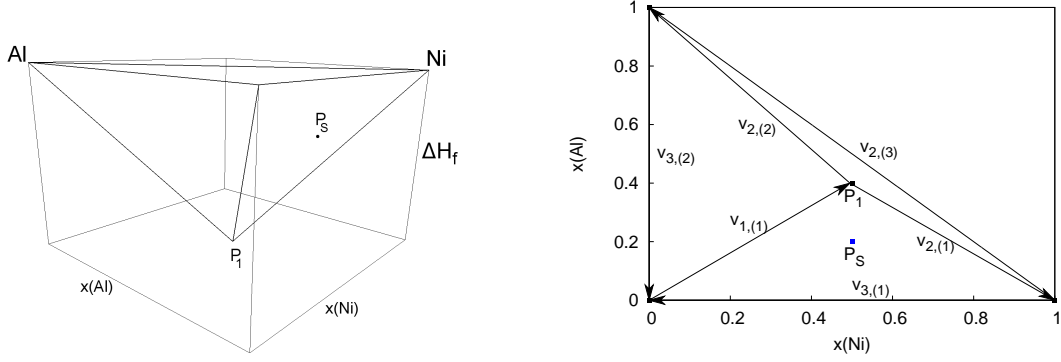
### 5.3.1 Technical details

In comparison to a CE for a binary alloy expanding the CE for a ternary system leads to several consequences. As already shown in section 2.6.1 the set of basis functions needs to be extended and the introduction of the third atom species increases the number of correlation functions, because each figure has now be described by more than one correlation function depending on the symmetry of the structure, which also increases the computational effort needed for the GA. Furthermore, the size of the configuration space for  $N$  lattice sites is now  $3^N$  instead of  $2^N$  for the binary case. Clearly, the number of input structures has to be raised significantly increasing the computational effort for the DFT calculations.

Introducing a third element needs an extension also for constructing the ground state diagram in the CE. Having determined the best set of figures, the ECIs and the corresponding enthalpies of formation the so-called convex hull has to be designed, which characterizes the now two-dimensional ground state *surface*. The convex hull is the ternary equivalent to the binary ground state line. The determination of the structures, which span the hull is much more elaborated. In a binary case the ground state line can be determined by starting with the phase with most negative (or smallest)  $\Delta H_f$ . If there are structures, whose enthalpies of formation lie below the line connecting the left- and right-neighbouring values in the phase diagram, they are by definition new ground states. Then, a new ground state line is designed and the CE-derived  $\Delta H_f$  of all possible compounds are compared to the values of the connecting lines.

Expanding this problem to a 3-dimensional representation, whereby the concentration  $x(E_i)$  of each element  $E_i$  constitutes a coordinate axis with the condition  $\sum_{i=1}^3 = 1$ , needs a more sophisticated mathematical treatment in finding the ground states and the enclosing 2-dimensional convex hull. At  $T=0K$  the convex hull is built up by planes and therefore, searching for the most stable phases with lowest  $\Delta H_f$  linear equations express the criterion for stability, correspondingly. The start of the CE may be done in the same way as for the binary case extracting the most stable phase of the total system. After introducing this phase into the ground state diagram three triangles are defined, which contain the value of  $\Delta H_f$  of the most stable phases and  $\Delta H_f$  of two of the three elements as their edges. In the next step, the equations of the planes describing the areas containing the formed triangles are constituted. Now the  $\Delta H_f$  values of all other CE-fitted structures can be compared to the value on the planes, which form such a triangle at the structures concentration.

In the present work this constructions was done by calculating the distance of the



(a) 3D convex hull containing the most stable phase

(b) Mapped 2D convex hull to determine which triangle contains  $P_S$

Figure 5.4: Mapping of the 3-dimensional ternary convex hull to 2-dimensional space. The vectors shown in panel (b) represent the construction for finding the triangle which contains the point  $P_S$ .

point

$$P_S = (x(Ni), x(Al), \Delta H_f) \quad (5.1)$$

characterising the structure of interest  $S$  by the vectors defining the formed planes in the ternary ground state diagram.  $x(Fe)$  in this description is defined by the relation  $x(Fe) = 1 - (x(Ni) + x(Al))$

To describe the routine used for the construction of the convex hull an example is given. Let us assume, that the most stable phase  $P_1$  has already been found with a composition of  $Fe_{10}Ni_{50}Al_{40}$  and  $\Delta H_f = -0.6$  eV.

$$P_1 = (0.5, 0.4, -0.6)^T \quad (5.2)$$

The sides of the three resulting triangles are described by the three vectors (also shown in figure 5.4 panel b mapped to 2-dimensional space):

1. triangle:

$$\mathbf{v}_{1,(1)} = (0.5, 0.4, -0.6)^T$$

$$\mathbf{v}_{2,(1)} = (0.5, -0.4, 0.6)^T$$

$$\mathbf{v}_{3,(1)} = (-1, 0, 0)^T$$

2. triangle:

$$\mathbf{v}_{1,(2)} = \mathbf{v}_{1,(1)} = (0.5, 0.4, -0.6)^T$$

$$\mathbf{v}_{2,(2)} = (-0.5, 0.6, 0.6)^T$$

$$\mathbf{v}_{3,(2)} = (0, -1, 0)^T$$

3. triangle:

$$\mathbf{v}_{1,(3)} = \mathbf{v}_{2,(2)} = (-0.5, 0.6, 0.6)^T$$

$$\mathbf{v}_{2,(3)} = (1, -1, 0)^T$$

$$\mathbf{v}_{3,(3)} = \mathbf{v}_{2,(1)} = (0.5, -0.4, 0.6)^T$$

In the next step we make a 2D projection (neglect the z-component, see figure 5.4) of the vectors since we only want to know which triangle contains a new structure  $P_S$ . Let us further assume that for a composition of  $Fe_{30}Ni_{50}Al_{20}$  we calculated a  $\Delta H_f = -0.4$  eV. The task now is to determine if this structure is a new ground state of the system.

$$P_S = (0.5, 0.2, -0.4)^T \quad (5.3)$$

To do so the equations of the lines

$$\mathbf{v}\mathbf{n} - c = 0 \quad (5.4)$$

defining the triangles are derived by computing the vectors  $\mathbf{n}$  (normalized to a length of 1) normal on the vectors  $\mathbf{v}_{i,(j)}$  and the constants (will only be shown for one triangle denoted with the index (1)):

$$\begin{aligned} \mathbf{n}_{1,(1)} &= (-0.625, 0.781)^T & c_{1,(1)} &= 0 \\ \mathbf{n}_{2,(1)} &= (0.625, 0.781)^T & c_{2,(1)} &= 0.625 \\ \mathbf{n}_{3,(1)} &= (0, -1)^T & c_{3,(1)} &= 0 \end{aligned}$$

Calculating the distance of the point  $P_S$  from the three lines can now easily be done by introducing the position vector in equation 5.4 resulting in the distances  $d$ :

$$\begin{aligned} d_{1,(1)} &= -0.156 \\ d_{2,(1)} &= -0.156 \\ d_{3,(1)} &= -0.2 \end{aligned}$$

All of the three distances are negative, which means that the structure lies in the triangle described by the vectors  $\mathbf{v}_{1,(1)}, \mathbf{v}_{2,(1)}, \mathbf{v}_{3,(1)}$ .

Now the  $\Delta H_f$  value on the triangle at the point (0.5,0.2) has to be defined. To do so the equation of the plane is derived analogue to the 2D picture is defined. A plane can be described by equation 5.4, with the difference, that the vectors are now 3 dimensional. The normalized normal vector  $\mathbf{m}$  to the plane can be calculated by the cross product of two of the plane delimiting vectors.

$$\mathbf{m}_{(1)} = \mathbf{v}_{1,(1)} \times \mathbf{v}_{2,(1)} = (0.0, -0.832, -0.555)^T \quad (5.5)$$

Since the chosen plane goes through (0,0,0) the constant is 0.

The  $\Delta H_f$  value on the plane at the concentration of  $P_S$  can now be calculated:

$$\begin{pmatrix} 0.0 \\ -0.832 \\ -0.555 \end{pmatrix} \cdot \begin{pmatrix} 0.5 \\ 0.2 \\ \Delta H_f \end{pmatrix} = 0 \Rightarrow \Delta H_f = -0.3 \text{ eV}$$

Comparing this value to the  $\Delta H_f$  of  $P_S$  (= -0.4eV) results in the finding, that  $P_S$  is a new ground state of the system, which can now be used as an edge of the new formed triangles.

	$E_{0,DFT}$ [eV]	$\Delta E_0$ [meV]	$E_{0,CE}$ [eV]	$\Delta H_{f,DFT}$ [eV]	$\Delta H_{f,CE}$ [eV]
fcc- Ni	-5.783	0.0	-5.783	0.0	0.0
fcc-Al	-3.725	0.0	-3.725	0.0	0.0
bcc- Fe	-8.333	0.0	-8.333	0.0	0.0
AlFe <sub>5</sub>	-7.717	3.5	-7.720	-0.152	-0.155
AlFe <sub>4</sub>	-7.591	0.1	-7.591	-0.179	-0.179
AlFe <sub>3</sub>	-7.395	-0.3	-7.395	-0.214	-0.214
AlFe	-6.361	-0.4	-6.361	-0.332	-0.332
Al <sub>2</sub> Fe	-5.629	0.1	-5.629	-0.368	-0.368
NiFe <sub>3</sub>	-7.697	0.5	-7.698	-0.002	-0.002
NiAl <sub>2</sub> Fe	-5.933	-0.2	-5.932	-0.609	-0.609
NiAl	-5.425	1.9	-5.427	-0.671	-0.673
Ni <sub>5</sub> Al <sub>3</sub>	-5.564	-6.2	-5.558	-0.553	-0.547
Ni <sub>2</sub> Al	-5.604	1.5	-5.606	-0.507	-0.509
Ni <sub>3</sub> Al	-5.683	0.5	-5.684	-0.414	-0.415

Table 5.1: DFT and CE derived total energies and enthalpies of formation at T=0K of the ground state phases as found for the Fe-Ni-Al system studying bcc-type structures only. The formation enthalpies are calculated relative to the experimental ground state structures of the elements (i.e. fcc for Ni and Al; bcc for Fe). The difference  $\Delta E_0$  represents the difference of the DFT and CE total energy.

### 5.3.2 CE calculations and results

To start a ground state search for the ternary system 19 structures with unit cells containing 16 atoms and the stoichiometry varying over the whole range of concentrations and the ground states resulting from the binary CEs were taken as the starting input set. The GA was started and the maximal size of the predicted structures was truncated to 4 atoms at the start. As described, only a selected concentration range had to be covered, namely all the structures, whose concentrations differ from  $x(\text{Ni})=x(\text{Al})$  by more than 15%. Now only those compositions within the range of  $|x(\text{Ni})-x(\text{Al})| < 0.3$  were used for the CE predictions and had the chance to become a new ground state.

Progressing the CE the maximal size of the predicted structures was increased steadily until it reached a size of 8 atoms per unit cell resulting in 6623 possible structures. This procedure led to a final input set consisting of 162 input structures with a very reasonable cross validation score of 2.0 meV. The maximal number of vertices for the figures, which were used to fit the energy of the system was truncated to 6 atoms. The best set of clusters -which led to a convergence of the cluster expansion- was truncated to 60 figures.

According to table 5.1 11 ground states with bcc-type structures were found for the

ternary system, including the ground states of the binary systems whose concentrations lie outside the concentration range of the ternary CE. From these results the convex hull of the system was constructed, as illustrated by figure 5.6. Its coordinate axes are represented by  $x(\text{Ni})$ ,  $x(\text{Al})$ , and  $\Delta H_f$ , respectively. The depth of the hull (i.e. z-axis) at different points represents the enthalpy of formation  $\Delta H_f$ , and by that the stability of the corresponding phase. As it can be seen from table 5.1 B2-NiAl is represented by the lowest point of the hull because the  $\Delta H_f$  is less negative in all directions until reaching zero at the corners, where the elemental phases are placed. Analyzing the boundary planes of the convex hull (i.e. the area of the binary phases) results in the energetical properties as discussed in sections 4.1,4.2, and 4.3. The triangular area between the points of the convex hull, which correspond to ground state phases, is a mixed phase region: it consists of a mixture of the phases defining the corner points of the triangle in question. The concentration of each stable phase in the mixture can be determined by the lever rule extended now to three components.

As a results of the ternary investigation of bcc-type phases,  $\text{NiAl}_2\text{Fe}$  is the only truly ternary ground state structure found. All the other ground state phases consist of mixtures of binary or elemental phases. The reason for this is that NiAl is dominating the investigated part of the phase diagram because of its lowest formation enthalpy. The binary ground states which populate the sides of the triangle are the ones also found for the binary ground state search with one exception, namely  $\text{Ni}_2\text{Al}$  is found to be a stable ground state of the ternary system. The reason of the difference to the binary CE is a very small discrepancy between DFT and binary CE derived enthalpies of formation for the compound. In more detail, the structure of  $\text{Ni}_2\text{Al}$  has already been included in the binary CE and has shown to be a ground state structure if the DFT calculated total energies were regarded. Figure 5.5 shows a comparison of the final ground state lines of the binary Ni-Al system regarding the DFT- and CE-derived values for  $\Delta H_f$ . It can be seen that the stability of  $\text{Ni}_3\text{Al}_2$  is overestimated in the CE fit by 2.8 meV compared to the DFT total energy. This small shift is sufficient to remove the  $\text{Ni}_2\text{Al}$  structure as a ground state of the binary system, since the CE-fitted  $\Delta H_f$  of  $\text{Ni}_2\text{Al}$  now lies 0.34 meV above the final binary ground state line resulting from CE. The CE-fit for the ternary system resulted in the determination of the  $\text{Ni}_2\text{Al}$  phase as a ground state of the system. Nevertheless, this small discrepancies between the different approaches is of no physical consequence because  $\text{Ni}_2\text{Al}$  is not stable anymore at slightly elevated temperatures.



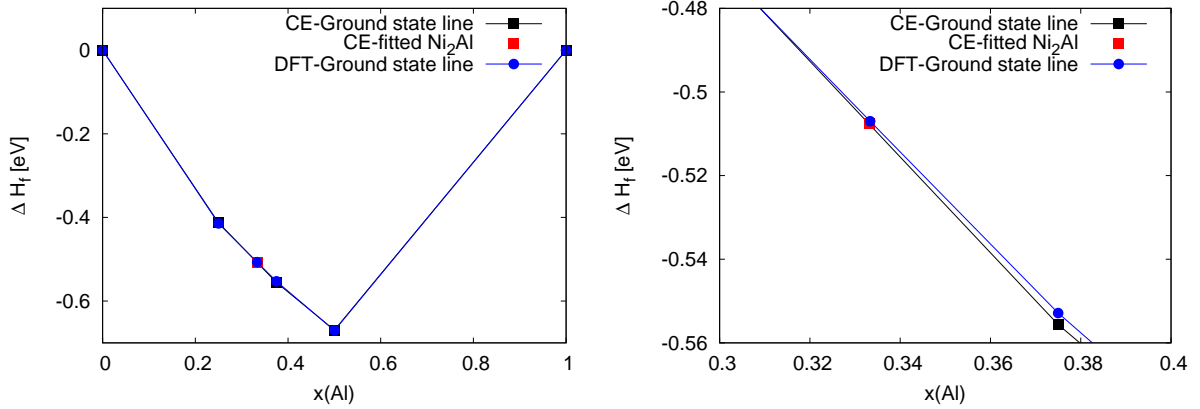


Figure 5.5: Comparison of the Ni-Al ground state lines gotten from DFT calculations and CE fit.

## 5.4 Monte Carlo simulations

### 5.4.1 Technical details

At the beginning of the MC simulations for the ternary system a grand canonical approach was tested for deriving the lowest internal energy at finite temperatures. For this task a path for  $\Delta\mu$  was searched, which described the evolution of the system on concentration trajectories ranging from  $x(\text{Fe})=0$  to  $x(\text{Fe})=1$  for a fixed ratio of  $x(\text{Ni})/x(\text{Al})$ . Such an approach, however, does not yield the result for the desired concentrations if the difference in the chemical potential is changed in equidistant steps since e.g. the formation of more stable areas in the energy landscape lead to a deviation from the estimated path. This means that the internal energy landscape had to be known before the values of  $\Delta\mu$  could be chosen, which described the system on such a chosen path. Because of that, for further MC simulations a canonical ensemble was used. By keeping the concentrations constant well defined parts of the phase diagram can be computed and the phases that form at this compositions can be described more easily.

Different to the MC simulations for the binary systems, which were done with a grand canonical ensemble, for the canonical description of the ternary system the number of steps used to converge the energy at a certain composition was defined by the change in the internal energy. For this purpose a number of steps was chosen for which the energy difference was calculated. If the difference in the internal energy was lower than the convergency limit then the simulation was stopped. Then the resulting energies and simulation boxes were used to define the phases in the phase diagram for the given temperature, at which the MC simulation was done.

Starting from completely random ordered distribution of atoms an energy difference

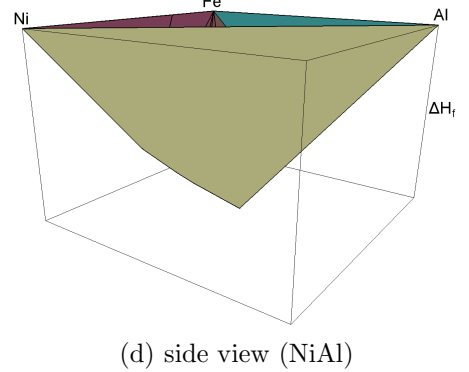
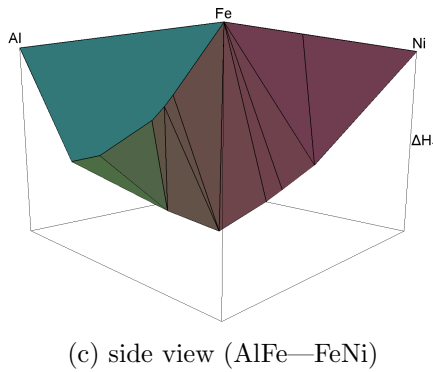
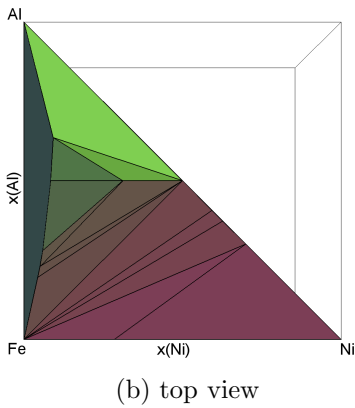
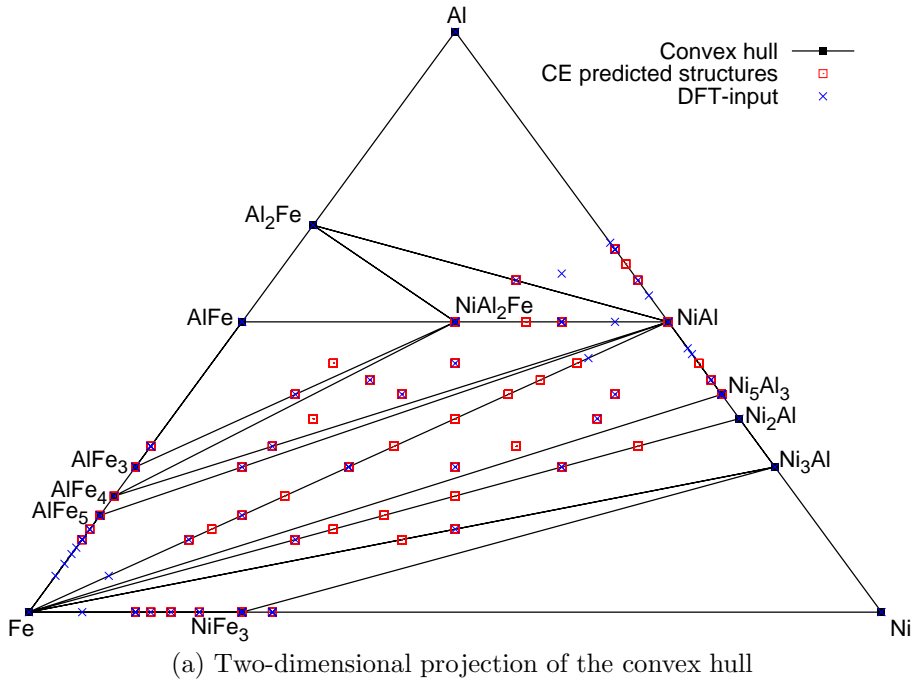


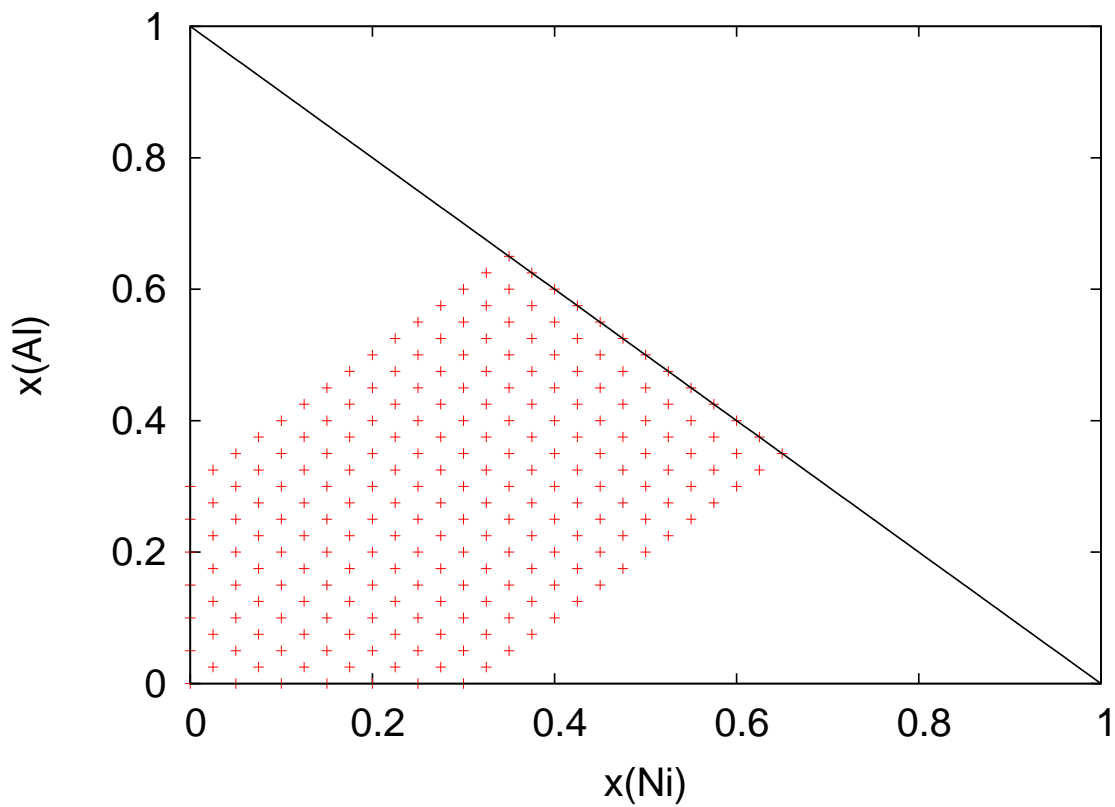
Figure 5.6: Convex hull as a result of the ground state search done by the ternary CE for bcc-type structures. Panel (a) shows a projection of the convex hull onto the Gibbs triangle. The ground states as described in table 5.1 are drawn as black squares. The DFT input phases are symbolized by blue crosses. Red squares denote structures, whose formation enthalpies were predicted by the converged CE ground state search. Because of the projection each red square represents more than one phase, since different ordering at a certain concentration leads to different energetical behaviour. In summary, 162 DFT-input structures (blue crosses) and 6623 predicted structures (red squares) are included in the plot. Panels (b-d) illustrate the three-dimensional convex hull form different points of view. The corners represent the elemental ground states of table 5.1. The differently coloured areas represent mixed phases consisting of the ground states, at the corresponding corner points.

of 10  $\mu\text{eV}$  after a set of 27,000 steps at 100 K was chosen as the convergence criterion for the chosen composition. In the next step the thus achieved distribution was taken as an input for an MC run with a refined convergence criterion of 5  $\mu\text{eV}$  after 100,000 steps. After convergence was achieved at 100 K the temperature was raised by 200 K and the converged simulation box was used as a starting point for the MC run for the new temperature. For some of the compositions, convergence happened into even lower internal energy when rising the temperature. The reason for that lies in the stochastic nature of the MC simulation due to the randomness of the choice of the next simulation step a local internal energy minimum might even be left at higher temperatures leading to the global minimum of the energy landscape. But since the temperature is just contained in the  $\beta=1/kT$  of the Boltzmann distribution (shown in section 2.8.3) a decrease of the internal energy at higher temperatures is not possible, since the value of  $E_i/kT$  in the canonical MC is lowered rising the temperature. As a result of this decrease the internal energy minimum is less deep and the Boltzmann distribution is broadened. The structural consequence is that the strict ordering -which leads to the minimum in the internal energy- is disturbed. Being aware of this fact lead to the following proceeding: The most stable composition formed at the temperature, which resulted in a lower minimum, was taken as starting point for a new MC run again starting at 100 K with the same convergence parameters.

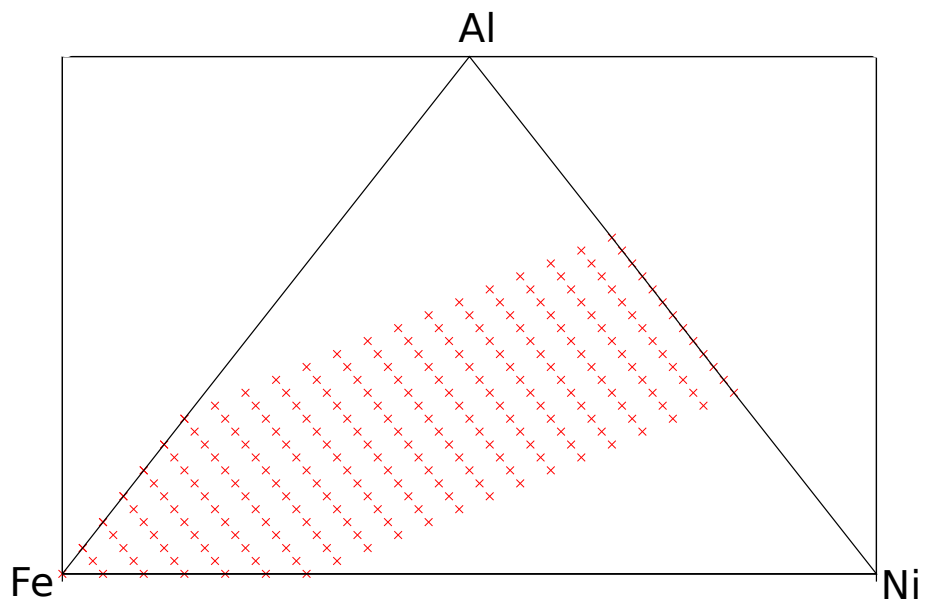
Another technical point is that the size of the simulation boxes had to be reduced for the ternary system. To get convergence in a reasonable time a 30x30x30 box with periodical boundary conditions was used for the final computations.

The already mentioned limiting of the investigated concentrations consisted in choosing a range of concentrations defined by a maximum deviation of 15% from the  $x(\text{Ni})/x(\text{Al})=1$  line. Figure 5.7 shows the calculated concentrations in two representations. Because  $x(\text{Fe})=1-x(\text{Ni})-x(\text{Al})$  is defined when  $x(\text{Ni})$  and  $x(\text{Al})$  are chosen, it was sufficient to vary the concentrations of Ni and Al. The chosen points of the range were constructed by the relation  $x(\text{Al})=x(\text{Ni})-d$  ( $-0.3 \leq d \leq 0.3$ ) according to panel (a) of figure 5.7. The concentration mesh was then constructed by steps of  $\Delta d = 0.05$  yielding 14 to 21 points per line and resulting in concentration steps of  $\Delta x(\text{Fe})=0.05$  and  $\Delta x(\text{Ni})=\Delta x(\text{Al})=0.025$  for each fixed  $x(\text{Fe})$ .

The analysis of the results of the MC simulations is focusing on two quantities. First, on the internal energy at each temperature and concentration and the subsequent calculation the formation enthalpy, which results in an image of the energy landscape of the system. This step was rather straightforwardly extracted from the MC output data in terms of the internal energies over the whole investigated concentration range and then deriving the enthalpies of formation from them. The resulting data are presented by contour plot in figure 5.13.



(a) Concentration mesh in a  $x(\text{Al})$  vs.  $x(\text{Ni})$  coordinate system.



(b) Concentration mesh in the Gibbs triangle

Figure 5.7: Two different representations of the selected concentrations.

A much more elaborate procedure was needed for the second task, for the definition of phases in the phase diagram in terms of pure and mixed phases, and for the formation of precipitations in the simulated alloys. The characterization method is already described in section 4.1.3. It consist in searching within a 3x3x3 box of atoms for local ordering, which is characteristic for the stable ordered phases.

## 5.4.2 Results and Discussion

Figures 5.10 to 5.12 show the phase diagrams as derived from the ternary CE and the subsequent MC simulation. The phase boundaries were constructed by fitting the shown data points with polynomials up to 5th order.

The phase diagram is dominated by B2-NiAl and mixed phases containing B2-NiAl and elemental phases. It is found at concentrations of  $x(\text{Fe})= 0$  up to 70 % Fe. The wide extension of the binary phase may be expected because of the very stable formation enthalpies of NiAl. This phase formation is in reasonable agreement to both experimental and other theoretical investigations, which indicate that a mixed B2-(NiAl,AlFe)phase forms even up to 80% Fe. On the Al rich side the B2-phase -consisting of mostly NiAl mixed with B2-AlFe- is stable up to higher Fe-concentrations compared to the Ni rich side. This behaviour can be explained by the stabilization of Fe precipitations in the B2- matrix, because Fe and Al tend to form a B2 ordered phase too. The Fe in the Al rich region is stabilized by the introduction into the B2 crystal replacing Ni in the Ni cubic sublattice by Fe atoms or by the formation of ordered phases, which do not destroy the B2-NiAl phase. At the nickel rich side such a stabilization is not favourable due to the fact, that bcc-Fe and Ni do not tend to form ordered stable phases. As a result the B2-NiAl phase breaks up at lower Fe concentrations at the Ni rich side of the Gibbs triangle, since the remaining Ni atoms -in contrast to the Al concentration- occupy antisite positions in the B2-NiAl phase instead of forming stable alloys with Fe. Figure 5.8 is an example of such a antisite formation at the Ni rich side in contrast to the Al rich region. It is obvious that on the Ni rich side the B2-phase is destroyed, while in regions with excess Al (relative to Ni) the system tends to maintain the B2-NiAl phase by placing Al into elemental Fe forming locally ordered  $\text{AlFe}_3$  and B2-AlFe alloys. Jiang *et al.* [76] studied theoretically off-stoichiometry effects in NiAl in terms of point defects by modeling quasi random structures in a concentration range of  $0.25 < x < 0.5$ . They derived formation enthalpies, lattice parameters and elastic constants of non-stoichiometric B2-NiAl phases in accordance with experimental data. The basic result of their work is, that the stabilization of B2-NiAl for varying concentrations happens via Ni-antisites (excess of Ni) or Ni-vacancies (excess of Al). The present CE approach does not describe vacancies, because for that an additional vacancy-sublattice would be necessary. However the formation of Ni antisites in the B2 ordered phase in Ni rich region agrees

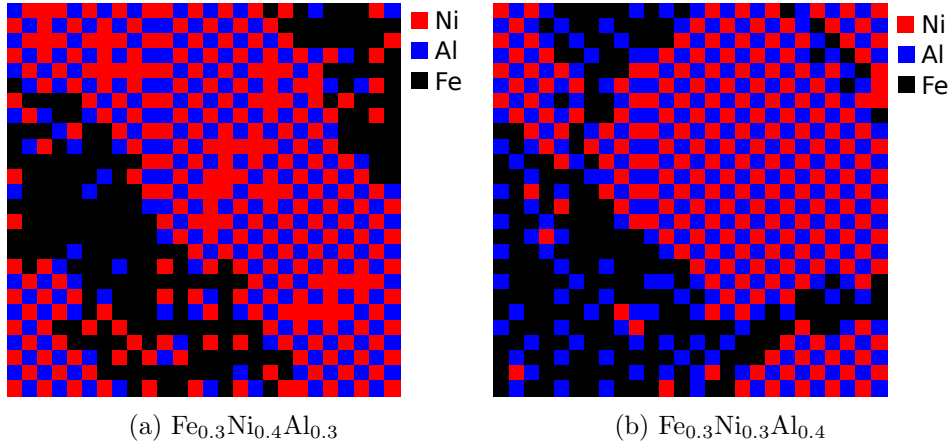


Figure 5.8: At 100K a cut through the MC simulation box at the Ni-rich (a) and the Al-rich (b) side of the phase diagram. At an excess of Ni the nickel atoms reside on Al sublattice sites (antisite defect). At the Al-rich side the B2-phase is not defective. The excessive Al atoms are found in regions containing Fe and tend to form ordered structures instead of forming antisites in the B2-NiAl phase.

nicely with previous findings. Basically this is an atomic size effect applying a simple model: Ni is smaller than Al and can be much more easily placed (i.e. the energy costs are low) on Al-sites than vice versa, because then Al would have Al-nearest neighbours.

The elemental phases are dominated by the A2-Fe phase. Due to the stability of the B2-NiAl phase into the ternary area the A2-Fe phase forms as a precipitation down to a Fe concentration of 60% Fe in the Al-rich side and down to almost 10% Fe in the Ni-rich side of investigated range. The reason for this behaviour may be illustrated by means of the binary phase diagrams. At the Ni rich side Fe precipitates up to higher Fe concentrations because the two elements do not tend to form ordered structures. Concerning Fe-Ni alloys (i.e. small Al concentrations) the binary and ternary CE give somewhat different results. In the binary CE the Ni-Fe system forms a solid solution over the whole concentration range already at 500 K, because Ni seems to be rather randomly distributed in the Fe matrix, and vice versa. According to the ternary CE, Ni atoms seem to precipitate in the iron matrix (and vice versa) even at 900 K. Possibly, the analysis of the short range order characteristics has to be refined, as will be implemented in a newer version of the UNCLE code.

In contrast to the trend of the Ni-Fe system in forming precipitations, the binary Al-Fe system tends to form ordered structures over the whole binary phase diagram. The formation of binary  $Al_xFe_y$  alloys is in contrast to the system containing B2-NiAl structures with A2-Fe precipitations. Other ground states than the B2-NiAl -as a single phase and as a mixed phase with B2-AlFe- found at the temperature zero point have not formed at finite temperatures in the ternary area of the Gibbs triangle. In the region

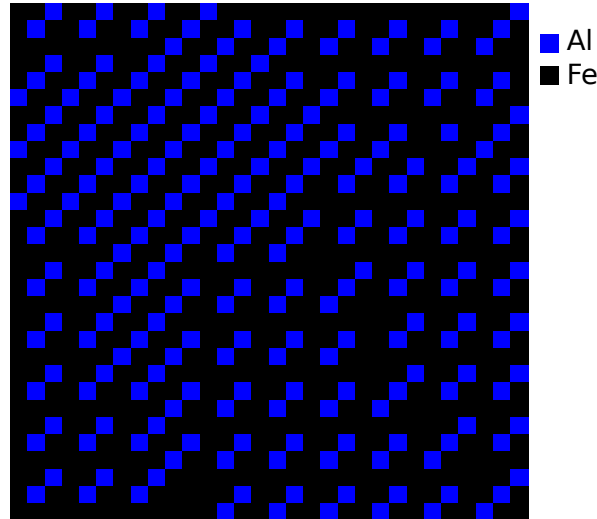


Figure 5.9: A cut through the MC simulation box for the binary alloy  $\text{Al}_{25}\text{Fe}_{75}$  at 100 K.

with very low Al concentration this trend was expected, since the formation enthalpy in this area has values, which are almost zero. As a consequence a formation of ordered structures at finite temperatures did not happen. At the quasi-binary Ni-Al side of the Gibbs triangle the B2-phase has formed over the whole investigated area. Comparing this result to the binary phase diagram would suggest that the  $\text{Ni}_5\text{Al}_3$  phase might form at the border of the investigated region. Nevertheless the phase was not identified at finite temperatures. The final quasi-binary subsystem is Al-Fe, which formed three ground states in the investigated area. From the ground states found by the binary CE only the  $\text{AlFe}_3$  structure has build on the side of the Gibbs triangle, which contains a neglectable Ni concentration. This finding is consistent with the description of the binary Al-Fe system (see section 4.2). Figure 5.9 shows an example of a layer in such a formed phase. The box contains a mixture of different oriented  $\text{AlFe}_3$  structures.

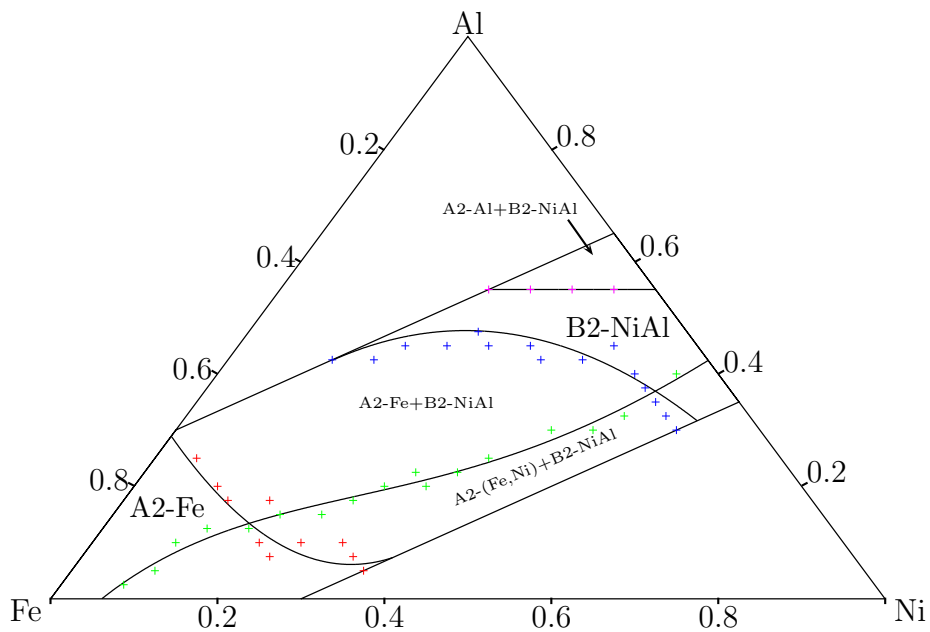


Figure 5.10: Fitted phase diagram at 100 Kelvin for the ternary FeNiAl system in a bcc lattice

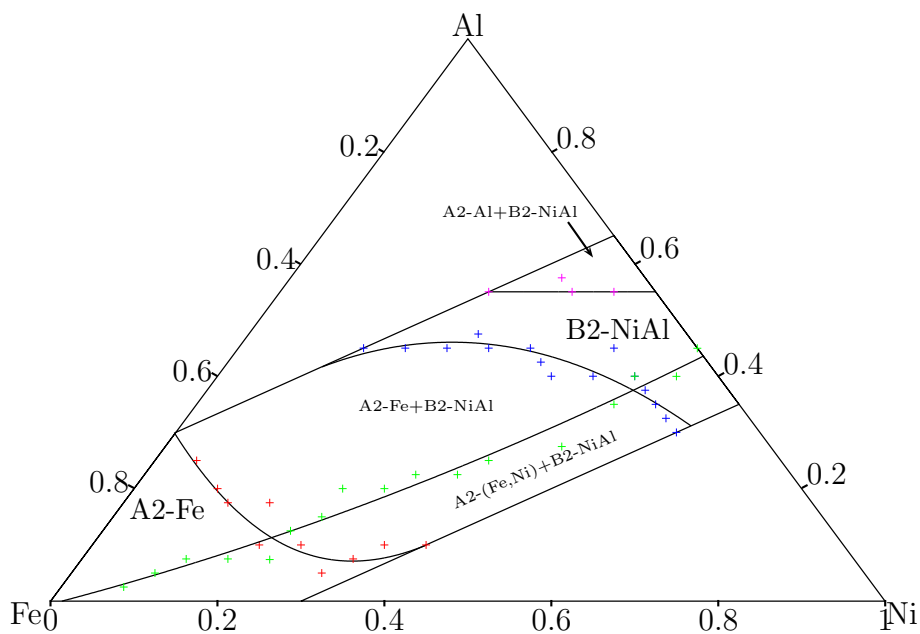


Figure 5.11: Fitted Gibbs triangle for the FeNiAl system in a bcc lattice at 700 Kelvin



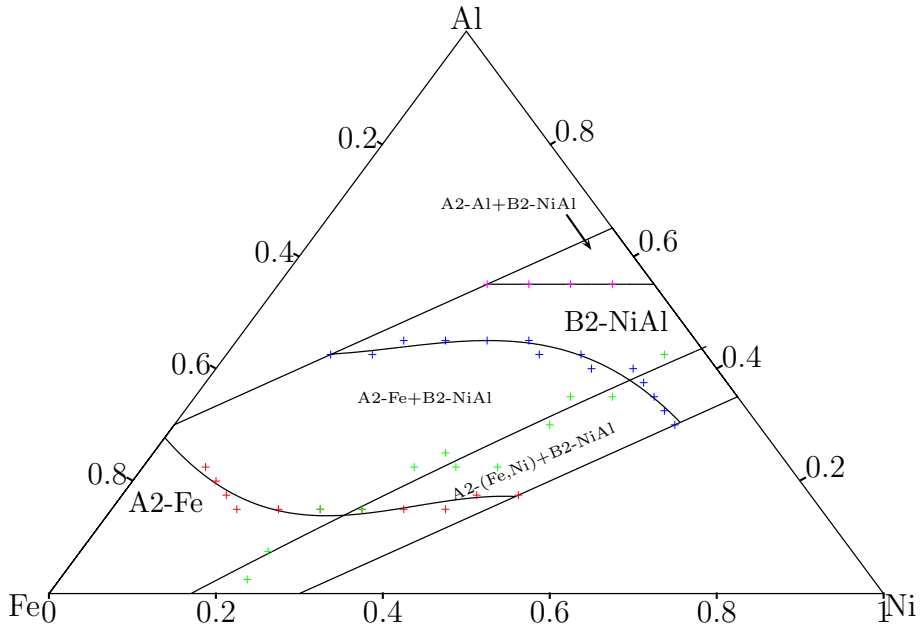


Figure 5.12: Fitted gibbs triangle for the FeNiAl system in a bcc lattice at 1300 Kelvin

### Enthalpies of formation

As already mentioned the B2-NiAl phase shows the lowest formation enthalpy in the system and is therefore dominating the energy landscape. Figure 5.13 shows contour plots of formation enthalpies for three of the investigated temperatures. As can be seen, the figure corroborates the role of the B2 phase as the dominating composition. Along the  $x(\text{Ni})=x(\text{Al})$  path the formation enthalpies are raised rather linearly until they reach 0 at pure Fe. Even more information can be extracted from the contour plots. A significant information is the thermodynamical stability of Fe-Al like phases in contrast to Fe-Ni phases. On the Al rich side of the investigated area the enthalpies of formation reach significantly lower values than on the corresponding Ni side. This trend has already been found for the binary systems. Since the binary phases are the main responsible for energy landscape in the ternary phase diagram too, this behaviour is not surprising.

Comparing the contour plots at different temperatures reveals, that by just introducing the configurational entropy as the main responsible for the behaviour of the system at elevated temperatures does not lead to high energetical differences. Comparing the contour plots at 100 and 700 K induces the interpretation, that the configurational entropy lead to no significant difference in the energy of the system. The transition from 700 to 1300 Kelvin shows more differences in the energy landscape. The weak tendency of Fe and Ni to order in (quasi-) binary structures is weakened even more at higher temperatures leading to formation enthalpies near the zero point in the binary area. As a

consequence, the formation enthalpy at the Al rich side of the Gibbs triangles is much less temperature dependent than on the Ni rich side. This leads to a notable raise in the negative value of the  $\Delta H_f$  of the ternary alloys when Al is alloyed to Fe-Ni.

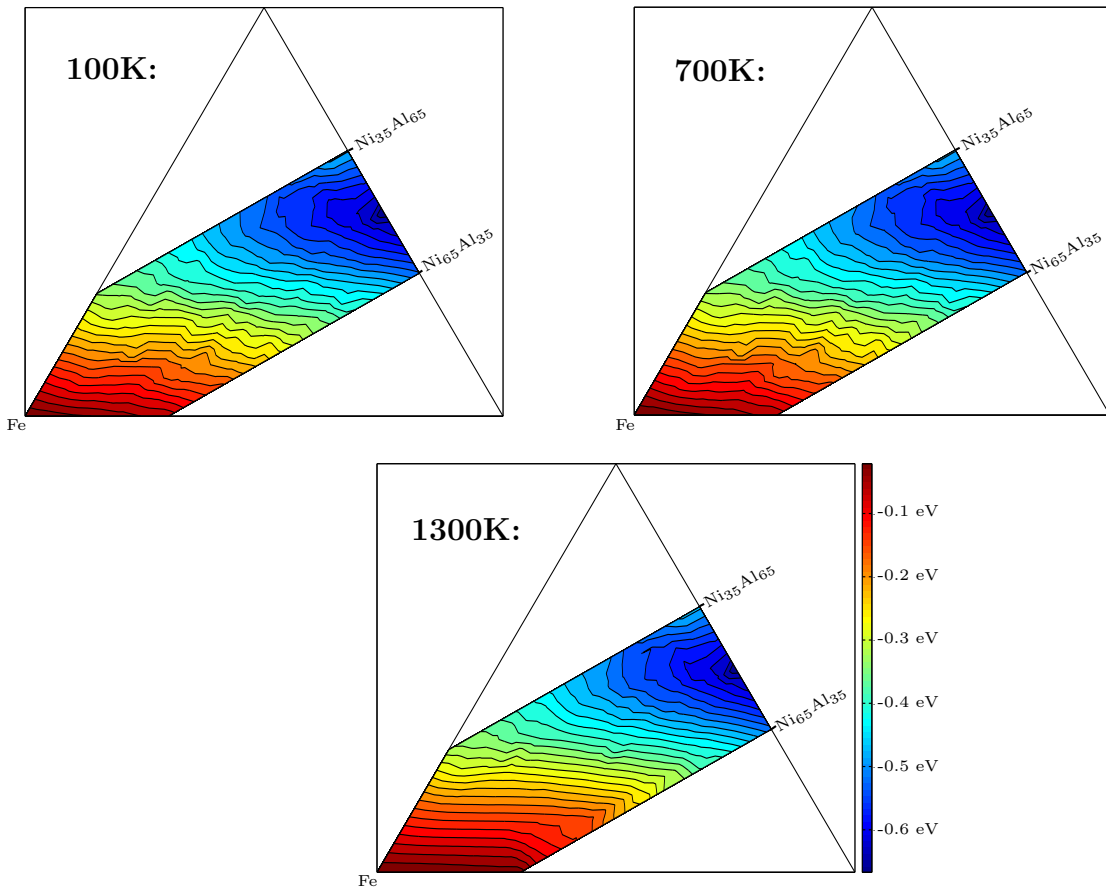


Figure 5.13: Formation energy contour plots at chosen temperatures in the investigated concentration area.

### 5.4.3 Pseudo binary $\text{Fe}_x(\text{NiAl})_{1-x}$ system

To describe the iron precipitations behaviour in system containing in presence of a stoichiometric ideal formed B2-NiAl phase the  $x(\text{Ni})=x(\text{Al})$  ( $y=x$  line of figure 5.7 (a)) was extracted explicitly from the ternary MC data.

Figure 5.14 presents a rather old experimental pseudo binary phase diagram elaborated in the year 1951 [77] and it reveals the interplay of the B2-(NiAl,AlFe) phase (denoted as  $\beta$ ) and the bcc-Fe elemental phase (denoted as  $\alpha\delta$ ). The B2 ordered structure reaches up to 95 at% of (NiAl) at a temperature of 500 °C. At higher temperatures the ordered phase is destabilized reducing the range down to 70 at% of NiAl at 1370 °C, where melting starts. The Fe exclusions in the mixed phases reach up to 97 at% Fe at 500 °C. At 1370 °C, where the mixed phase starts to melt the highest iron concentration forming exclusion is about 30 at%. It should be noted that the transition from bcc-Fe into fcc- $\gamma$ -Fe and vice versa is not part of the current work dealing with CE for bcc-type structures.

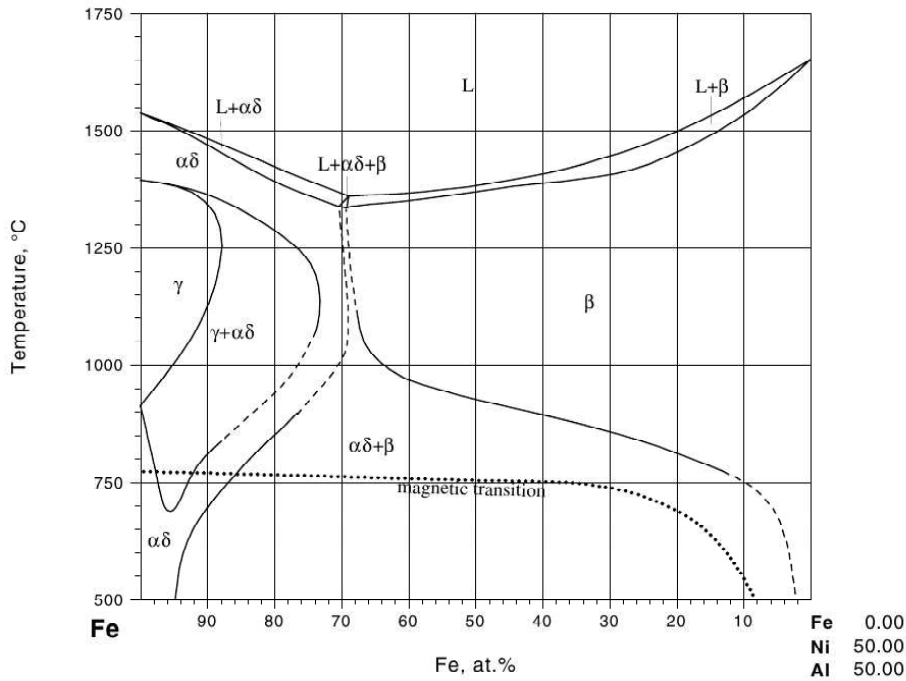


Figure 5.14: Pseudo binary phase diagram for  $\text{Fe}_x(\text{NiAl})_{1-x}$  [77]. The  $\beta$  phase displayed in the picture represent the B2-NiAl phase here. The phase denoted as  $\alpha\delta$  is the A2 (bcc) elemental phase, since iron crystallizes in a bcc-structure at lower ( $\alpha$ ) and higher ( $\delta$ ) temperatures splitted by the fcc- $\gamma$  phase.

Figure 5.16 compares the experimental phase diagram with the results of the present calculation. Regarding just configurational entropy in the MC simulation seems not to

contribute significantly to the stability of the two phases and the phases start to form at the same Fe concentrations at every temperature. The extension of the A2 phase of Fe at low temperatures is in good agreement to the experimental phase diagram. The raise of the concentration range, where the A2-Fe phase is formed as a single phase at higher temperatures have not resulted of the CE + MC simulation done. Introducing temperature dependency via vibrational free energies may lead to a better agreement to the experiment. In the calculation the extension of the B2-NiAl phase is underestimated over the whole temperature range. Figure 5.15 shows the transition from the mixed phase containing both the B2-NiAl and the A2-Fe phases to the pure A2-Fe phase with Ni and Al dissolved. It is obvious that at a concentration of  $\text{Fe}_{70}(\text{NiAl})_{30}$  the Ni and Al still cluster in form of a B2-NiAl patches but the formation of an explicitly ordered phase is hindered by the excess of Fe atoms. By comparing the temperature dependency the effect of the configurational entropy is visible. It is characterized by the destabilization of the ordered B2 phase. This effect is reduced at the transition from 100 to 700 K compared to the transition from 700 to 1300 K.

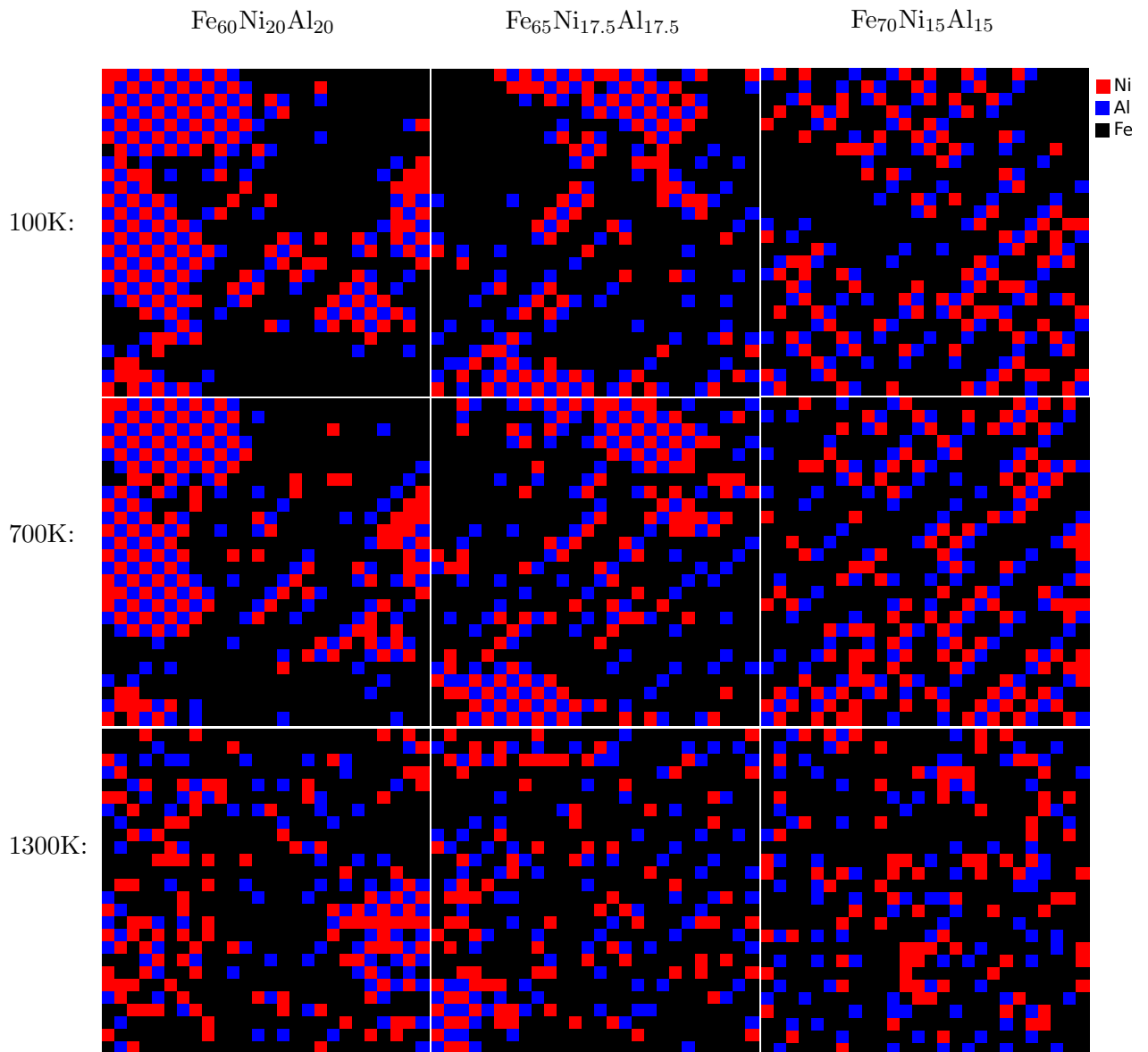


Figure 5.15: Selected layers of MC boxes for pseudo binary system. The concentration have been chosen to represent the transition from the mixed phase consisting of B2-NiAl and A2-Fe to the phase consisting of A2-Fe and dissolved Ni and Al atoms. By comparing the results for different temperatures the increase in entropy is visualized because at the  $\text{Fe}_{65}\text{Ni}_{17.5}\text{Al}_{17.5}$  and  $\text{Fe}_{60}\text{Ni}_{20}\text{Al}_{20}$  composition NiAl cluster are formed. At the concentration of  $\text{Fe}_{70}\text{Ni}_{15}\text{Al}_{15}$  Ni and Al still try to form B2-like clusters way, but the clustering is hindered by the presence of Fe atoms. At higher temperatures the formation of NiAl cluster gets less probable.

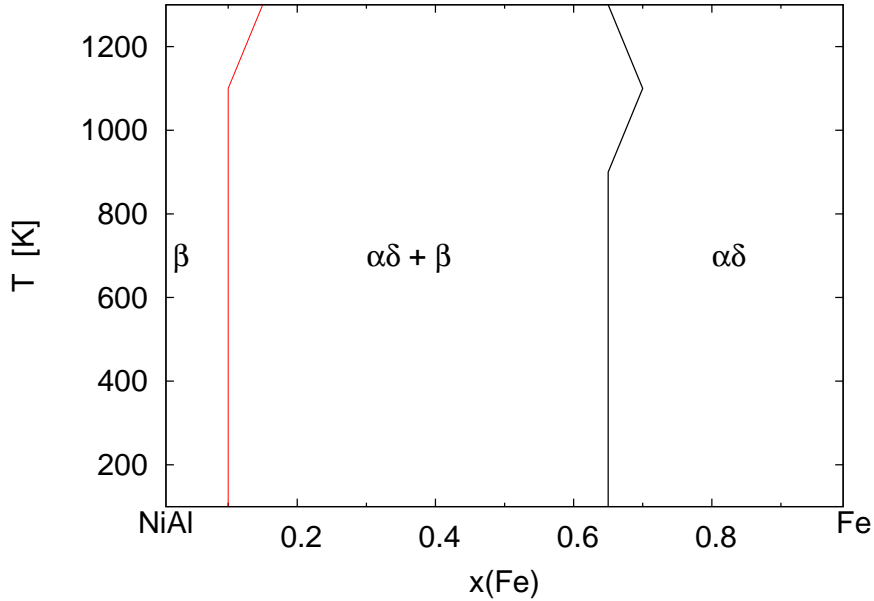


Figure 5.16: Pseudo binary phase diagram based on the results of the present work. The nomenclature has been taken from the work from Bradley [77]:  $\beta$  denotes B2-NiAl and  $\alpha$  A2-Fe.

#### 5.4.4 Fe-rich side of the phase diagram

Since the main scope of this thesis was the determination of the phase stability at the Fe rich side of the phase diagram this final section will deal in more detail with this part of the Gibbs triangle. The main characteristics of the system in this concentration area will be elaborated for zero up to 20% concentration of Ni and Al. from almost no nickel and aluminium concentration up to 20 percent.

Figure 5.17 shows the MC results at compositions from  $\text{Fe}_{95}\text{Ni}_{2.5}\text{Al}_{2.5}$  up to  $\text{Fe}_{80}\text{Ni}_{10}\text{Al}_{10}$ . At very low temperatures Ni and Al cluster in the Fe matrix forming precipitations and they already tend to assemble in a B2 like way. Raising the temperature the clusters dissolve quite easily and a solid solution of the two metal atoms in the Fe matrix is formed already at a temperature of 700 K. At even higher temperature the dissolution is enhanced. The situation is different when the Ni to Al ratio of is changed. Figure 5.18 shows the MC results for a ratio of 3:1 (and vice versa) and 90% Fe. When Ni is abundant compared to Al the formation of precipitations is in favor. Even at temperature of 700 K precipitations are formed. Nevertheless, mixing into the Fe matrix is enhanced. At the highest investigated temperature of 1300 K the clusters break up and a solid solution with Ni and Al in Fe s the result. In general, Al tends to assemble with Ni.

At an excess of Al the situation is completely different. Al dissolves in the Fe matrix already at 100 K and even tends to form ordered clusters corresponding to  $\text{AlFe}_3$ . As can

be seen, the MC simulation at this low temperature is dominated by  $\text{AlFe}_3$  precipitates. Raising the temperature to 700 K leads to a partially destruction of  $\text{AlFe}_3$  due to the mixing of Al in the Fe matrix. This trend is enhanced at higher temperatures. Adding Ni is always attracted by Al which finally weakens the formation of  $\text{AlFe}_3$ .

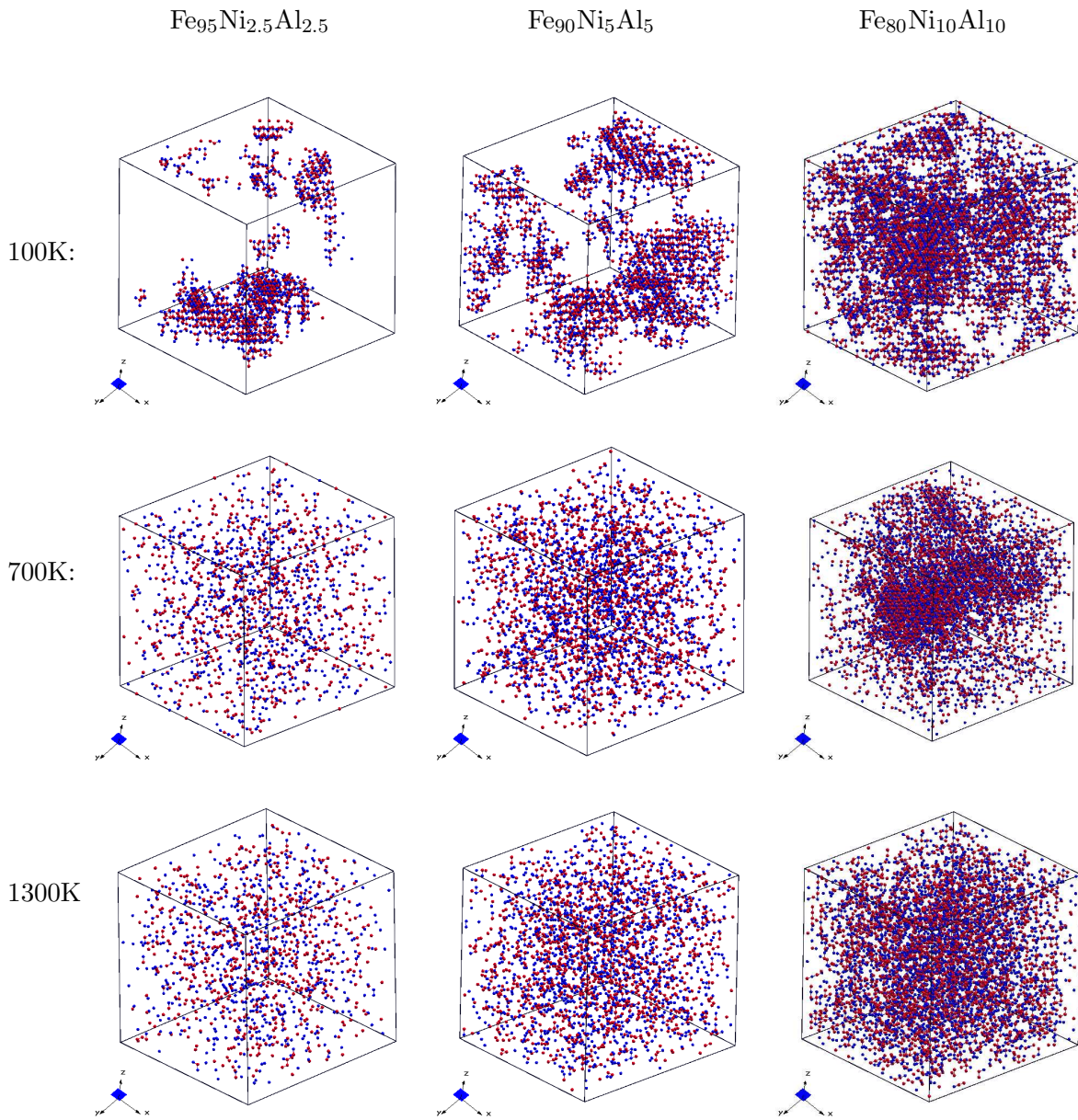


Figure 5.17: Visualization of the MC simulations at different temperatures and compositions in the Fe rich side of the Gibbs triangle. Ni atoms are colored in red, Al atoms in blue. The Ni/Al ration is 1.



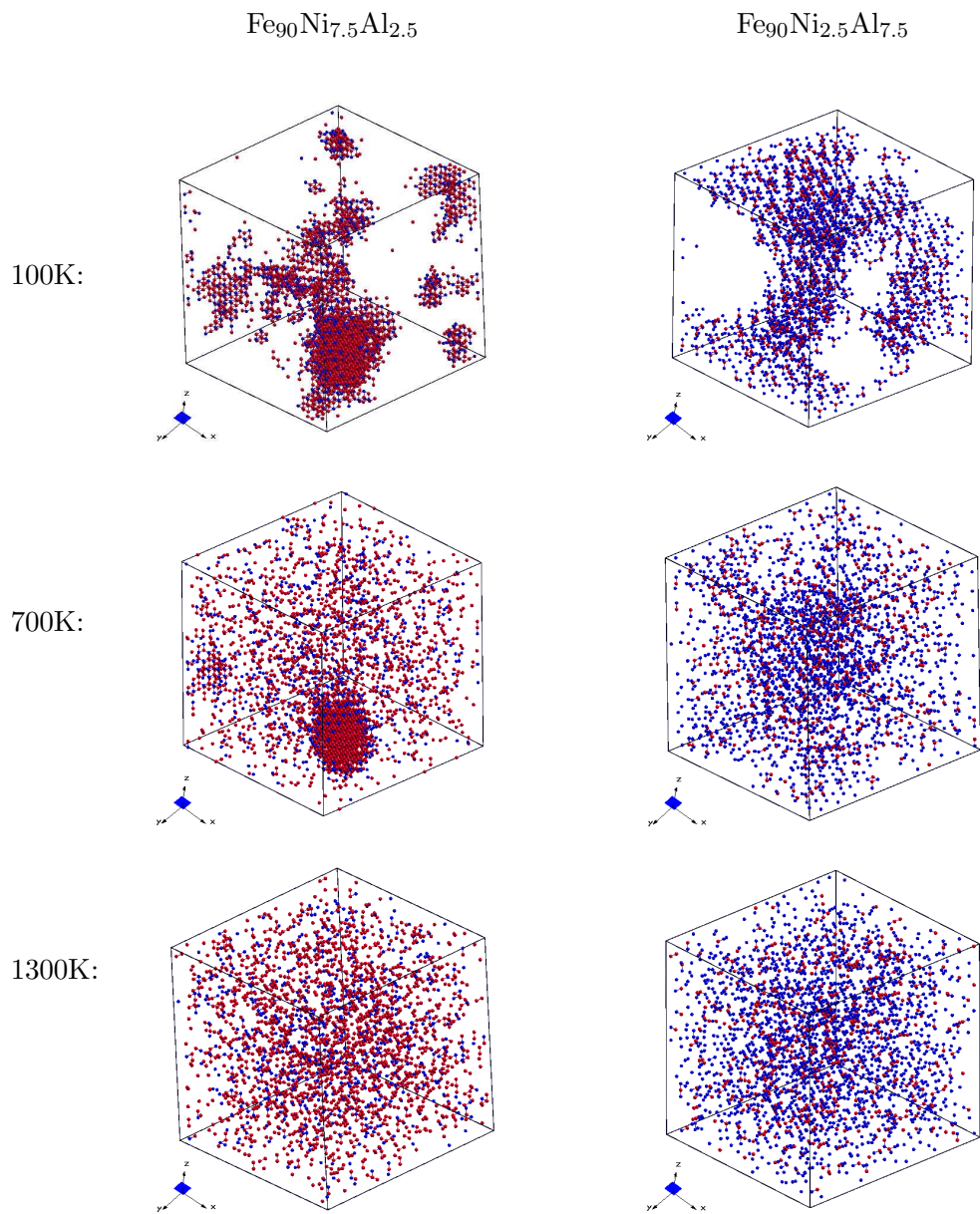


Figure 5.18: Visualization of the MC simulations at different temperatures and compositions in the Fe rich side of the Gibbs triangle. Ni atoms are colored in red, Al atoms in blue. The Ni/Al and Al/Ni ratio is 3:1.



The aim of the the present diploma thesis was the determination of phase stabilities of the ternary alloy system Fe-Ni-Al maintaining the accuracy, as customary for density functional theory calculations. The chosen procedure consisted in the application of the Cluster Expansion in combination with Monte Carlo simulations, whereby the interaction parameters were obtained from fitting to density functional theory calculations. Because the Fe-rich region of the ternary alloy system was of interest, the body centered cubic lattice was chosen as the parent lattice for the Cluster Expansion. All stable phases found on the basis of the Cluster Expansion have therefore bcc-type structures.

Starting with the density functional theory investigation of the elemental phases, then continuing with the binary systems for the complete concentration ranges the ternary phases were studied for the concentration ranges of  $|x(\text{Ni})-x(\text{Al})| < 0.3$  and  $1 < x(\text{Fe}) < 0$ .

The most remarkable result of the binary phases is that a very stable B2-NiAl compound is formed which dominates the energy landscape also for the ternary case. Other two ground states of the Ni-Al system were identified, namely Ni<sub>3</sub>Al and Ni<sub>5</sub>Al<sub>3</sub>. For the Al-Fe system it was discovered, that the most stable phase is Al<sub>2</sub>Fe, followed by AlFe in the B2 structure. Also, an AlFe<sub>3</sub>-phase with a bcc-type structure has been found as a ground state, which so far is not found in literature. More investigations on this phase are in progress. The overall enthalpies of formation of the Al-Fe alloys has less negative values than for Ni-Al alloys, but still reflect high stability. The third binary system, Ni-Fe, did not tend to form ordered structures in the bcc lattice.

The results of the Cluster Expansion for the binary systems were then taken as starting configurations for the ground state search of the Cluster Expansion of the ternary phases. In addition to the stable binary phases one ternary phase, namely FeNiAl<sub>2</sub>, was found to be a ground state structure.

The converged set of cluster interaction energies was used to perform Monte Carlo simulations, which where based on a grandcanonical ensemble for the binary systems and a canonical ensemble for the ternary case. An adequate procedure of heating and cooling was elaborated to simulate the ordering of the formed phases starting from completely unordered systems (infinite temperature) and cooling down to 100 Kelvin. The effect of the configurational entropy was studied by then slowly heating up again.

The identification of the formed phases in the Monte Carlo simulation boxes was done by analyzing the short range ordering in an extension of  $3 \times 3 \times 3$  atoms for the binary and ternary phases. Elemental precipitations were identified by clusters consisting of at least 10 atoms.

Because of the expressed stability of the NiAl binary phase, it also occurs in larger regions of the Gibbs triangle for the ternary case. NiAl is detected to form down to 20 % NiAl, while the Fe forms elemental precipitations. In the Fe-rich part of the ternary system the phase behaviour as already found for the binary systems leads to different orderings for varying Al and Ni concentrations. While in a Al rich region stable phases of  $\text{AlFe}_3$  type, the Ni rich side of the Gibbs triangle is characterized by Ni precipitates in the iron matrix. In both cases Ni and Al already tend to cluster in a B2 like way.

# Bibliography

---

- [1] D. Lerch, O. Wiekhorst, G. L. W. Hart, R. W. Forcade, and S. Muller, “UNCLE: a code for constructing cluster expansions for arbitrary lattices with minimal user-input,” *Modelling Simul. Mater. Sci. Eng.*, vol. 17, p. ., 2009.
- [2] P. Hohenberg and W. Kohn, “Inhomogeneous Electron Gas,” *Phys. Rev.*, vol. 136, pp. B864–B871, Nov 1964.
- [3] L. H. Thomas, “The calculation of atomic fields,” *Mathematical Proceedings of the Cambridge Philosophical Society*, vol. 23, pp. 542–548, 1926.
- [4] E. Fermi, “Un metodo statistico per la determinazione di alcune proprieta dell’ atome,” *Rend. Accad. Naz. Lincei*, vol. 6, pp. 602–607, 1927.
- [5] P. Dirac, “Note on Exchange Phenomena in the Thomas Atom,” *Mathematical Proceedings of the Cambridge Philosophical Society*, vol. 26, pp. 376–385, 1930.
- [6] W. Kohn and L. J. Sham, “Self-Consistent Equations Including Exchange and Correlation Effects,” *Phys. Rev.*, vol. 140, pp. A1133–A1138, Nov 1965.
- [7] Herman, Frank, V. Dyke, J. P., Ortenburger, and I. B., “Improved Statistical Exchange Approximation for Inhomogeneous Many-Electron Systems,” *Phys. Rev. Lett.*, vol. 22, pp. 807–811, Apr 1969.
- [8] D. M. Ceperley and B. J. Alder, “Ground State of the Electron Gas by a Stochastic Method,” *Phys. Rev. Lett.*, vol. 45, pp. 566–569, Aug 1980.
- [9] J. Perdew, K. Burke, and M. Ernzerdorf, “General gradient approximation made simple,” *Phys. Rev. Lett.*, vol. 23, pp. 3865–3868, 1996.
- [10] G. e. Chiarotti, *1.6 Crystal structures and bulk lattice parameters of materials quoted in the volume*. SpringerMaterials, .
- [11] G. Kresse and J. Fuerthmueller, “Efficient iterative schemes for ab intio total energy calculations using a plane-wave basis set,” *Phys. Rev. B*, vol. 54, pp. 11169–11186, 1996.
- [12] G. Kresse and D. Joubert, “From ultrasoft pseudopotentials to the projector augmented-wave method,” *Phys. Rev. B*, vol. 59, pp. 1758–1775, 1999.
- [13] P. Bloechl, “Projector augmented-wave method,” *Phys. Rev. B*, vol. 50, pp. 17953–17973, 1994.

- [14] R. P. Feynman, “Forces in Molecules,” *Phys. Rev.*, vol. 56, pp. 340–343, Aug 1939.
- [15] H. Hellmann, “Einführung in die Quantenchemie,” *Angewandte Chemie*, vol. 54, p. 156, 1937.
- [16] J. M. Sanchez, F. Ducastelle, and D. Gratias, “Generalized cluster description of multicomponent systems,” *Physica A: Statistical and Theoretical Physics*, vol. 128, no. 1-2, pp. 334 – 350, 1984.
- [17] Asta, Mark, D. de Fontaine, M. van Schilfgaarde, M. Sluiter, and M. Methfessel, “First-principles phase-stability study of fcc alloys in the Ti-Al system,” *Phys. Rev. B*, vol. 46, pp. 5055–5072, Sep 1992.
- [18] M. Asta, R. McCormack, and D. de Fontaine, “Theoretical study of alloy phase stability in the Cd-Mg system,” *Phys. Rev. B*, vol. 48, pp. 748–766, Jul 1993.
- [19] C. Colinet, A. Pasturel, D. Nguyen Manh, D. G. Pettifor, and P. Miodownik, “Phase-stability study of the Al-Nb system,” *Phys. Rev. B*, vol. 56, pp. 552–565, Jul 1997.
- [20] K. Yuge, A. Seko, A. Kuwabara, F. Oba, and I. Tanaka, “First-principles study of bulk ordering and surface segregation in Pt-Rh binary alloys,” *Phys. Rev. B*, vol. 74, p. 174202, Nov 2006.
- [21] P. R. Alonso and G. H. Rubiolo, “Relative stability of bcc structures in ternary alloys with  $Ti_{50}Al_{25}Mo_{25}$  composition,” *Phys. Rev. B*, vol. 62, pp. 237–242, Jul 2000.
- [22] A. Van der Ven and G. Ceder, “Vacancies in ordered and disordered binary alloys treated with the cluster expansion,” *Phys. Rev. B*, vol. 71, p. 054102, Feb 2005.
- [23] F. Lechermann, *Ab-initio Betrachtungen zur Elektronenstruktur und Statistischen Mechanik von mehrkomponentigen intermetallischen Systemen am Beispiel Ni-Fe-Al*. PhD thesis, Universität Stuttgart, 2003.
- [24] O. Wieckhorst, *Theoretische Untersuchungen zur Struktur und Stabilität binärer intermetallischer Phasen auf ab-initio Basis*. Shaker Verlag, 2007.
- [25] E. Ising, “Beitrag zur Theorie des Ferromagnetismus,” *Zeitschrift für Physik A Hadrons and Nuclei*, vol. 31, pp. 253–258, 1925. 10.1007/BF02980577.
- [26] A. van de Walle, “A complete representation of structure-property relationships in crystals,” *Nature Materials*, vol. 7, p. 455–458, 2008.
- [27] A. Franceschetti, S. V. Dudiy, S. V. Barabash, A. Zunger, J. Xu, and M. van Schilfgaarde, “First-Principles Combinatorial Design of Transition Temperatures in Multicomponent Systems: The Case of Mn in GaAs,” *Phys. Rev. Lett.*, vol. 97, p. ., 2006.
- [28] H. Y. Geng, M. H. F. Sluiter, and N. X. Chen, “Cluster expansion of electronic excitations: Application to fcc Ni–Al alloys,” *J. Chem. Phys.*, vol. 122, p. doi:10.1063/1.1926276, 2005.

- [29] M. Stöhr, P. R., and M. S., “Ab initio phase diagram of oxygen adsorption on W(110),” *J. Phys.: Condens. Matter*, vol. 21, p. 134017, 2009.
- [30] PhD. thesis of David Reith, University of Vienna. Will be handed in in 2011.
- [31] K. Yuge, “Phase stability of boron carbon nitride in a heterographene structure: A first-principles study,” *Phys. Rev. B*, vol. 79, p. 144109, Apr 2009.
- [32] N. A. Zarkevich and D. D. Johnson, “Reliable First-Principles Alloy Thermodynamics via Truncated Cluster Expansions,” *Phys. Rev. Lett.*, vol. 92, p. 255702, Jun 2004.
- [33] J. H. Holland, *Adaption in Natural and Artificial Systems*. MIT Press, Cambridge, MA, 1975.
- [34] <http://en.wikipedia.org/wiki/Nickel>.
- [35] H. J. Monkhorst and J. D. Pack, “Special points for Brillouin-zone integrations,” *Phys. Rev. B*, vol. 13, pp. 5188–5192, Jun 1976.
- [36] <http://en.wikipedia.org/wiki/Aluminium>.
- [37] A. Lutts and P. Gielen, “The precise determination of the Lattice Parameter of  $\alpha$ -Iron and some of its Alloys,” *J. Appl. Cryst.*, vol. 4, p. 242, 1971.
- [38] C. Paduani and E. Silva, “Electronic structure of gamma-iron,” *Journal of Magnetism and Magnetic Materials*, vol. 134, pp. 161–166, 1994.
- [39] J. Chipman, “Thermodynamics and Phase Diagram of the Fe-C System,” *Metallurgical and Materials Transactions B*, vol. 3, pp. 55–64, 1972.
- [40] J. Zhu, X. W. Wang, and S. G. Louie, “First-principles pseudopotential calculations of magnetic iron,” *Phys. Rev. B*, vol. 45, pp. 8887–8893, Apr 1992.
- [41] <http://en.wikipedia.org/wiki/Iron>.
- [42] W. Huang and Y. Chang, “A thermodynamical analysis of the Ni-Al system,” *Intermetallics* 6, vol. 6, pp. 487–498, 1998.
- [43] P. Oramus, C. Massobrio, M. Kozłowski, R. Kozubski, V. Pierron-Bohnes, M. Cadeville, and W. Pfeiler, “Ordering kinetics in Ni<sub>3</sub>Al by molecular dynamics,” *Computational Materials Science* 27 (2003) 186–190, vol. 27, pp. 186–190, 2003.
- [44] S. L. J. Bitterlich H, Löser W, “Reassessment of Ni-Al and Ni-Fe-Al Solidus Temperatures,” *Phase Equilib*, vol. 23, p. 301, 2002.
- [45] L. Eleno, K. Frisk, and A. Schneider, “Assessment of the Fe-Ni-Al system,” *Intermetallics*, vol. 14, no. 10-11, pp. 1276 – 1290, 2006. EUROMAT 2005.
- [46] R. Darolia, D. Lahrman, and R. Field, “The effect of iron, gallium and molybdenum on the room temperature tensile ductility of NiAl,” *Scripta Metallurgica et Materialia*, vol. 26, no. 7, pp. 1007 – 1012, 1992.

- [47] E. George, C. Liu, J. Horton, C. Sparks, M. Kao, H. Kunsmann, and T. King, “Characterization, processing, and alloy design of NiAl-based shape memory alloys,” *Materials Characterization*, vol. 32, no. 3, pp. 139 – 160, 1994. Memory Metals.
- [48] G. Mondio, “The reflectivity spectra of Al<sub>3</sub>Ni and AlNi<sub>3</sub>,” *Journal of Electron Spectroscopy and Related Phenomena*, vol. 85, pp. 1–7, 1997.
- [49] P. S. Khadkikar and K. Vedula, “An investigation of the Ni<sub>5</sub>Al<sub>3</sub> phase,” *J. Mater. Res. 2 (2)*, Mar/Apr 1987, vol. 2, pp. 163–167, 1987.
- [50] K. Rzyman and Z. Moser, “Calorimetric studies of the enthalpies of formation of Al<sub>3</sub>Ni<sub>2</sub>, AlNi and AlNi<sub>3</sub>,” *Progress in Materials Science*, vol. 49, pp. 581–606, 2004.
- [51] N. P. Singleton MF, Murray JL, *Binary alloy phase diagrams*. ASM International, 1991.
- [52] N. Dupin, I. Ansara, and B. Sundman, “Thermodynamic re-assessment of the ternary system Al-Cr-Ni,” *Calphad*, vol. 25, no. 2, pp. 279 – 298, 2001.
- [53] W. Oelsen and W. Middel, “(title not found),” *Mitt. Kaiser-Wilhelm-Znst. fuer Eisenforschung*, vol. 19, pp. 1–26, 1937.
- [54] O. Kubaschewski, “The Heats of Formation in the System Aluminium - Nickel - Titanium,” *Trans. Faraday Soc.*, vol. 54, pp. 814–820, 1958.
- [55] E. T. Henig and H. L. Lukas, “(title not found),” *Z. Metallkd.*, vol. 66, pp. 98–106, 1975.
- [56] C. McKamey, J. DeVan, P. Tortorelli, and V. Sikka, “A review of recent developments in Fe<sub>3</sub>Al-based alloys,” *J.Mater.Res.*, vol. 6, pp. 1779–1805, 1991.
- [57] M. Palm, “Concepts derived from phase diagram studies for the strengthening of Fe–Al-based alloys,” *Intermetallics*, vol. 13, p. 1286–1295, 2005.
- [58] C. McKamey, P. Maziasz, and J. Jones, “Effect of addition of molybdenum or niobium on creep-rupture properties of Fe<sub>3</sub>Al,” *J. Mater. Res.*, vol. 7, p. 2089–2106, 1992.
- [59] S. Yangshan, Y. Zhengjun, Z. Zhonghua, and H. Haibo, “Mechanical properties of Fe<sub>3</sub>Al-based alloys with cerium addition,” *Scripta Metallurgica et Materialia*, vol. 33, no. 5, pp. 811 – 817, 1995.
- [60] D. G. Morris, M. A. Muñoz-Morris, and C. Baudin, “The high-temperature strength of some Fe<sub>3</sub>Al alloys,” *Acta Materialia*, vol. 52, no. 9, pp. 2827 – 2836, 2004.
- [61] D. G. Morris and S. Gunther, “Strength and ductility of Fe—40Al alloy prepared by mechanical alloying,” *Materials Science and Engineering A*, vol. 208, no. 1, pp. 7 – 19, 1996.
- [62] D. Morris, M. Muñoz-Morris, and L. Requejo, “New iron-aluminium alloy with thermally stable coherent intermetallic nanoprecipitates for enhanced high-temperature creep strength,” *Acta Materialia*, vol. 54, no. 9, pp. 2335 – 2341, 2006.



- [63] S. Risanti, D.D., “Strengthening of iron aluminide alloys by atomic ordering and Laves phase precipitation for high-temperature applications,” *Intermetallics*, vol. 13, p. 1313–1321, 2005.
- [64] T. Massalski, *Binary phase diagrams*. ASM, Metal Parks, 1986.
- [65] R. N. Corby and P. J. Black, “The structure of FeAl<sub>2</sub> by anomalous dispersion methods,” *Acta Crystallographica Section B*, vol. 29, no. 12, pp. 2669–2677, 1973.
- [66] P. J. Black, “The structure of FeAl<sub>3</sub>. II,” *Acta Crystallographica*, vol. 8, pp. 175–182, Mar 1955.
- [67] M. Crimp and K. Vedula, “Effect of boron on the tensile properties of B2 FeAl,” *Materials Science and Engineering*, vol. 78, no. 2, pp. 193 – 200, 1986.
- [68] J. Fedotova, A. Ilyuschenko, T. Talako, A. Belyaev, A. Letsko, A. Zaleski, J. Stanek, and A. Pushkarchuk, “Atomic Arrangement in B2 FeAl Prepared by Self-Propagated High-Temperature Synthesis at Varying Al Content and Annealing,” in *HFI/NQI 2004* (K. Maier and R. Vianden, eds.), pp. 738–744, Springer Berlin Heidelberg, 2005.
- [69] B. Meyer, V. Schott, and M. Fähnle, “Phonon spectrum of B2-FeAl: Ab initio calculation and comparison with data from inelastic neutron scattering,” *Phys. Rev. B*, vol. 58, pp. R14673–R14676, Dec 1998.
- [70] K. Stepien and M. Kupka, “Effect of hydrogen on room-temperature hardness of B2 FeAl alloys,” *Scripta Materialia*, vol. 59, no. 9, pp. 999 – 1001, 2008. Viewpoint set no. 44.
- [71] L. J. Swartzendruber, V. P. Itkin, and C. B. Alcock, “The Fe-Ni (iron-nickel) system,” *J. Phase Equil.*, vol. 12, p. 288, 1991.
- [72] J. Petersen, M. Aydin, and J. Knudsen, “Mössbauer spectroscopy of an ordered phase (superstructure) of FeNi in an iron meteorite,” *Physics Letters A*, vol. 62, no. 3, pp. 192 – 194, 1977.
- [73] P. D. Liu CT, *Ni<sub>3</sub>Al and its alloys in intermetallic compounds, principles and practice*, vol. 2. Wiley and Sons, 1995.
- [74] S. G. Letzig D, Klower J, “Screening of NiAl-Base Ni-Fe-Al Alloys for Structural High Temperature Applications and Development of a New Ni-30Fe-10Al-Cr Alloy,” *Zeitschrift fuer Metallkunde*, vol. 90, p. 712, 1999.
- [75] G. Marcon, R. Pefenx, and H. Lemaire, “Fe-Ni-Al phase diagram in AlNi type permanent magnets related area,” *IEEE transactions on magnetics*, vol. MAG-14,5, pp. 685–688, 1978.
- [76] C. Jiang, L.-Q. Chen, and Z.-K. Liu, “First-principles study of constitutional point defects in B2 NiAl using special quasirandom structures,” *Acta Materialia*, vol. 53, no. 9, pp. 2643 – 2652, 2005.

- [77] A. Bradley, “Microscopical Studies on the Iron-Nickel- Aluminium System. Part II. The Breakdown of Body-Centered Cubic Lattice,” *J. Iron Steel Inst (London)*, vol. 168(3), pp. 233–244, 1951.

# Danksagung

---

Ein steiniger Pfad führte zur Vollendung dieser Diplomarbeit und meines gesamten Studiums. An diesem Punkt möchte ich den Leuten danken die mich in meinem Werdegang unterstützt haben und mir die Durchführung dieser Arbeit überhaupt erst möglich gemacht haben:

In erster Linie möchte ich meinen Eltern danken, ohne deren moralische und finanzielle Unterstützung der Abschluss meines Studiums und die Durchführung dieser Diplomarbeit überhaupt nicht möglich gewesen wäre. Weiters darf man in diesem Zusammenhang natürlich auch meine Geschwister Barbara, Peter und Ilse nicht vergessen, welche mir im Laufe meines Studiums bei der Erlangung von Stipendien, beim Finden von Nebenjobs und bei jedem Problem mit Rat und Tat zur Seite standen.

Als nächstes möchte ich Prof. Raimund Podloucky danken, der mich in seiner Arbeitsgruppe aufgenommen hat und mir dadurch die Möglichkeit gegeben hat die Arbeitsweise in der theoretischen Naturwissenschaft in einer sehr angenehmen (nahezu familiären) Umgebung zu erlernen.

Einige Mitarbeiter der Arbeitsgruppe sind hier speziell zu erwähnen, da ich finde dass sie auch einen grossen Einfluss darauf hatten dass diese Arbeit zustande gekommen ist. Allen voran möchte ich hier David Reith und Markus Stöhr danken, die mich zu Beginn meiner Arbeit in die Welt von VASP und der Cluster Expansion eingeführt haben, und mir bis zum Schluss bei jedem Problem und bei jeder Frage sofort weitergeholfen haben, auch wenn sie oft selbst beschäftigt waren.

Auch meinen Zimmerkollegen Claudia Blaas-Schenner und Marcel Hieckel gebührt grosser Dank, da sie mir beim Erlernen der Arbeit in UNIX und bei jedem weiteren Problem immer mit all ihren Möglichkeiten und Fähigkeiten zur Seite standen. Weiters habe ich die Gespräche und Diskussionen mit ihnen (natürlich auch mit den anderen Mitgliedern der Arbeitsgruppe) sehr genossen, welche immer einen frischen Wind in die manchmal etwas stressigere Erarbeitung dieser Arbeit gebracht haben.

Der Arbeitsgruppe um Stefan Müller möchte ich hier auch für die Bereitstellung des UNCLE codes herzlich danken. Allen voran gebührt hier Tobias Kerscher großer Dank, da er mir bei jeder noch so lächerlichen Frage immer mit seiner Erfahrung und seinem Können zur Seite stand. Weiterer Dank gilt auch Prof. Georg Kresse (und seinen Mitarbeitern) für die Bereitstellung des VASP codes, der die *ab initio* Basis dieser Arbeit ermöglicht hat.

Abschliessend möchte ich hier auch noch dem “Fond zur Förderung der wissenschaftlichen Forschung” (FWF) anführen, welche mir durch die finanzielle Unterstützung dieser Arbeit sehr geholfen hat.



# Curriculum vitae

---

Name: Georg Kastlunger  
Geburtsdatum: 12. November 1985  
Geburstort: Meran (I)  
Staatbürgerschaft: Italienisch

## Ausbildung

09.2004 - 08.2011: Studium der Chemie an der Universität Wien  
09.1999 - 07.2004: Realgymnasium "Albert Einstein", Meran  
07.2004: Matura  
09.1996 - 07.1999: Mittelschule "Josef Wenter", Meran  
09.1991 - 07.1996: Volksschule "Franz Tappeiner", Meran

## Fachspezifische Tätigkeiten

07.2009 - 08.2009: Ferialpraktikum bei "Torggler chimica", Meran